THE DEVELOPMENT OF A NOVEL MRI BASED METHOD FOR MEASURING BLOOD PERFUSION IN NEUROVASCULAR DAMAGE

by

Emma Metcalfe-Smith

A thesis submitted to the University of Birmingham for the degree of DOCTOR OF PHILOSOPHY

Physical Sciences for Health
School of Chemistry
College of Engineering and Physical Sciences
University of Birmingham
October 2019

Abstract

Diffusion-weighted magnetic resonance imaging (DWI) is a key neuroimaging technique. Multi b-value DWI data is composed of an unknown number of exponential components which represent water movement in various compartments, notably tissues and blood vessels. The bi-exponential model, Intravoxel Incoherent Motion (IVIM), is commonly used to fit the perfusion component but does not take account of the multi-component nature of the data.

In this work, a new fitting method, the Auto-Regressive Discrete Acquisition Points Transformation (ADAPT) was developed and evaluated on simulated, phantom, volunteer and clinical DWI data. ADAPT is based on the auto-regressive moving average model, making no prior assumptions about the data.

ADAPT demonstrated that it could correctly identify the number of components within the diffusion signal. The ADAPT coefficients demonstrated a significant correlation with IVIM parameters and a significantly stronger correlation with cerebral blood volume derived from dynamic susceptibility contrast MRI. A reformulation of the ADAPT method allowed the IVIM parameters to be mathematically derived from the diffusion signal and demonstrated lower bias and more accuracy than currently implemented fitting methods, which are inherently biased. ADAPT provides a novel method for non-invasive determination of diffusion and perfusion biomarkers from complex tissues.

To Alex,

For all the love, support and tea you have made.

Declaration

I declare that the work presented within this thesis is entirely my own with the following exceptions:

- Clinical data was acquired by the radiographers at Birmingham Children's Hospital Radiology Department.
- Informed consent was obtained and the East Midlands – Derby Research Ethics Committee (REC 04/MRE04/41) approved the study operating under the rules of Declaration of Helsinki 1975 (and as revised in 1983).
- The post-processing of the Dynamic Susceptibility Contrast data was performed using an in-house tool developed by Dr Stephanie Withey.

Acknowledgements

I want to give a huge thanks to my supervisors Professor Andrew Peet, Dr Niloufar Zarinabad, Dr Jan Novak and Professor Hamid Dehghani, for all of their guidance and support throughout my PhD. Andrew, thank you for the time and energy you have given to this project. Thank you for rescuing me from the numerous ‘Maths Holes’ I found myself stuck in! Niloufar, thank you so much for everything you have taught me and always encouraging me to strive to do the best I can.

I would also like to express my thanks to the rest of the CBTRT, both past and current members. Emma Meeus, thank you for being a fantastic mentor and helping me get to grips with diffusion MRI. Stephen Powell, for being there in the MATLAB meltdowns and always up for a cup of tea. Thank you to the Physical Sciences for Health Centre for Doctoral Training for creating a great community of interdisciplinary scientists. Emma McCarthy, seeing you was always the highlight of my trips to campus. Thank you so much for your friendship over the last four years.

Thank you to the Engineering and Physical Sciences Research Council (EPSRC EP/L016346/1), for funding this project. I also acknowledge support from the National Institute for Health Research (NIHR-RP-R2-12-019), the Cancer Research UK Experimental Cancer Medicine Centre Paediatric Network (C8232/A25261), Health Data Research UK and Free Radio in conjunction with Help Harry Help Others (HHHO). MR imaging was performed in the NIHR 3T MRI Research Centre at Birmingham Children’s Hospital.

Finally, I would like to thank my family. Mum and Dad for always encouraging me and instilling a love of learning from an early age. Those extra advent calendars to learn how to count really paid off. Alex, thank you for coming on this adventure to Birmingham with me. You and Teddy have given me such a wonderful home life and I’m so grateful for your love and support.

Journal Publications

- **E. Metcalfe-Smith**, E. M. Meeus, J. Novak, H. Dehghani, A. C. Peet, N. Zarinabad, “Auto-regressive Discrete Acquisition Points Transformation for Diffusion Weighted MRI Data”, *IEEE Transactions on Biomedical Engineering*, doi: 10.1109/TBME.2019.2893523, January 2019

Conference Presentations

- **E. Metcalfe-Smith**, E.M. Meeus, J. Novak, H. Dehghani, A.C. Peet, N. Zarinabad, "An Investigation into the multicompartment nature of diffusion MRI data". Conference presentation: BCISMRM Post Graduate Symposium, London, UK- Oral Presentation (2017)
- **E. Metcalfe-Smith**, E.M. Meeus, N. Zarinabad, J. Novak, H. Dehghani, A.C. Peet, "Investigating the multi-compartment nature of diffusion MRI data". Conference presentation: University of Birmingham Research Poster Conference, Birmingham UK- Poster Presentation (2017)
- **E. Metcalfe-Smith**, E.M. Meeus, N. Zarinabad, J. Novak, H. Dehghani, A.C. Peet, "An Investigation into the ARMA model for evaluating diffusion MRI". Conference presentation: Transmed Student Conference, University of Birmingham, UK- Oral and Poster Presentation (2017)
- **E. Metcalfe-Smith**, N. Zarinabad, J. Novak, H. Dehghani, A.C. Peet, "Novel fitting methods for Diffusion Weighted MRI data". Conference presentation: Round-Table Forum- Imaging and Brain Science, Southeast University, Nanjing, China- Oral Presentation (2017)
- **E. Metcalfe-Smith**, N. Zarinabad, J. Novak, H. Dehghani, A.C. Peet, "A method for fitting multiexponential diffusion-weighted MRI data". Conference presentation: IEEE International Symposium on Biomedical Imaging Annual Meeting, Washington DC, USA -Poster Presentation (2018: 696)
- **E. Metcalfe-Smith**, N. Zarinabad, J. Novak, H. Dehghani, A.C. Peet, "Multicompartment modelling of diffusion-weighted MRI data with no prior

assumptions”. Conference presentation: ISMRM Annual Scientific Meeting, Paris, France-Poster Presentation (2018-1594)

- **E. Metcalfe-Smith**, N. Zarinabad, J. Novak, H. Dehghani, A.C. Peet, “A novel method for the detection of the number of compartments in diffusion MRI data”. Conference presentation: ISMRM Annual Scientific Meeting, Paris, France-Poster Presentation (2018-1595)
- **E. Metcalfe-Smith**, N. Zarinabad, J. Novak, H. Dehghani, A.C. Peet, “A Method for Accurately Measuring the Pseudo-Diffusion Coefficient in Intravoxel Incoherent Motion (IVIM) Imaging”. Conference presentation: BCISMRM Post Graduate Symposium, Birmingham, UK- Oral Presentation (2019)

Table of Contents

List of Illustrations

List of Tables

List of Abbreviations

ADC = Apparent Diffusion Coefficient

ADAPT=Auto-Regressive Discrete Acquisition Points Transformation

AIC=Akaike Information Criterion

AICc=Corrected Akaike Information Criterion

AIF=Arterial Input Function

ANOVA = Analysis of Variance

AR=Auto-Regressive

ARMA=Auto-Regressive Moving Average Model

ASL=Arterial Spin Labelling

BICc=Corrected Bayesian Information Criterion

CBF = Cerebral Blood Flow

CBV = Cerebral Blood Volume

CSF = Cerebrospinal Fluid

CT=Computed Tomography

CV = Coefficient of Variation

DCE=Dynamic Contrast Enhancing

DKI=Diffusion Kurtosis Imaging

DSC = Dynamic Susceptibility Contrast

DTI=Diffusion Tensor Imaging

DWI = Diffusion-Weighted Imaging

EPI=Echo Planar Imaging

FOV=Field of View

GM = Grey Matter

IC=Inverse Crime

IVIM = Intravoxel Incoherent Motion

LDE=Linear Difference Equation

LER=Log Evidence Ratio

MA=Moving Average

MRI = Magnetic Resonance Imaging

MTT = Mean Transit Time

NEMA=National Electrical Manufacturing Association

NIRS= Near-Infrared Spectroscopy

NSA=Number of Signal Averages

PET=Positron Emission Tomography

PFD=Partial Fraction Decomposition

PGSE=Pulse Gradient Spin Echo

PVE=Partial Volume Effects

QIBs=Quantitative Imaging Biomarkers

rCBV=relative Cerebral Blood Volume

RF=Radio Frequency

ROI = Region of Interest

RSS=Residual Sum Squared

SAR=Specific Absorption Rate

SEM=Stretched Exponential Model

SENSE=Sensitivity Encoding

SNR = Signal to Noise Ratio

WM = White Matter

Chapter 1

Introduction

1. Introduction

1.1 Effects of Neurovascular Damage on the Brain

Neurovascular damage is the disruption of blood vessels that supply the brain and spinal cord. Acute disruption to blood vessels or blood flow can quickly impair the central nervous system and become life-threatening. Chronic damage to blood vessels leads to neurodegeneration and associated neurocognitive and neurological disability (1). Highly sensitive and rapid imaging techniques are crucial in our understanding, diagnosis and management of such cerebral conditions.

Neurovascular injuries can present in a multitude of ways (2), dependent upon the injury/disease and site of vascular disruption. Neurovascular damage can be caused directly from injury, such as blunt force trauma (3) or radiation therapy (4), or from disease, such as stroke (5) or a brain tumour (6), and has been linked to dementia (7). For acute conditions, imaging can provide rapid identification of the neurovascular condition, leading to a quick diagnosis, essential in the treatment of conditions such as strokes (8). For less acute conditions, non-invasive imaging techniques can diagnose and monitor the neurovascular damage, crucial for patient management.

Imaging techniques can be implemented to obtain quantitative perfusion measurements. These measurements can aid in the understanding of different conditions, perhaps most clearly demonstrated in the assessment of brain tumours (9)(10). All current methods for measuring perfusion have significant limitations (11), and in this thesis, novel methods which address some of these limitations are developed and evaluated. These methods are developed with a specific focus on children who have brain tumours. However, the techniques developed should apply to a variety of conditions.

1.2 Measuring Blood Perfusion with MRI

Cerebral perfusion, the passage of fluid through the circulatory system, can be measured with a range of different modalities including Magnetic Resonance Imaging (MRI), Computed Tomography (CT) (12), Positron Emission Tomography (PET) (13) and Near-Infrared Spectroscopy (NIRS) (14).

NIRS can provide continuous perfusion measurements through the assessment of the absorption of the near-infrared electromagnetic spectrum. However, due to its penetration depth, NIRS can only be used to scan cortical tissue (15), and spatial resolution is poor, only localised to the site of the source-detector measurements (16). PET is a long-established modality for measuring cerebral dynamics, in particular, Cerebral Blood Flow (CBF). However, PET uses radioactive tracers, requiring a cyclotron, and limits its repeatability or use in healthy volunteers (17). Additionally, the invasive procedure is at risk of complications and is sensitive to noise (18). Hence this modality is only feasible in very specific settings (11). CT provides reproducible quantitative perfusion measurements (12) and is faster and more readily available than MRI. However, MRI provides a higher spatial resolution with greater sensitivity (19). With MRI, perfusion can be measured with high temporal and spatial resolution (20).

With MRI, the most common method for estimating CBF requires the dynamic tracking of a paramagnetic bolus and is known as Dynamic Susceptibility Contrast (DSC) (21) (other bolus tracking techniques such as Dynamic Contrast Enhanced (DCE) (22) imaging are also commonly used and are further discussed in Section 2.3.4) . Parameters such as Cerebral Blood Volume (CBV) and Mean Transit Time (MTT) can also be measured with DSC; the results can be visualised as parametric colour maps than can be interpreted qualitatively or quantitatively (23). CBV is considered a robust parameter for the evaluation of brain tumours due to the direct relationship to the capillary size and density (24). DSC measurements can aid in the grading of tumours (25), provide useful hemodynamic information not available through standard MR imaging alone- aiding in diagnosis (26) and also in predicting patient outcome (27). However, the interpretation of perfusion measurements can be challenging, quantification of parameters can be difficult to determine (28), and post-processing results can be user-dependent (22). Poor signal to noise ratio measurements requires the implementation of quality control methods (29)(30). In addition, there is no consensus over the protocol to implement (31). For methods requiring a bolus, there are serious concerns over the potential toxicity of the contrast agents used (32). Hence alternative methods of measuring blood perfusion, which are non-invasive, are greatly desired. Arterial Spin Labelling (ASL) is a non-invasive perfusion measurement technique that is gaining considerable attention (33). However, interpretation of ASL measurements can be difficult because of low signal to noise ratio levels (34) and the repeated use during examinations for some populations, such as children, is restricted due to high specific absorption rates (35). Another non-invasive technique for measuring perfusion effects is Diffusion-Weighted Imaging (DWI), which is readily available on current MRI scanners and is routinely used in clinical practice as part of brain MRI.

1.3 Measuring Blood Perfusion with Diffusion-Weighted Imaging: Advantages and Limitations

DWI is a non-invasive MR imaging technique that measures the random movement of water molecules within biological tissue. Intravoxel Incoherent Motion (IVIM) imaging is a DWI technique that requires multiple b-values (a parameter that is changed by varying the diffusion sensitization of the MR sequence) in order to measure diffusion and perfusion-related properties of biological tissue (36) (a comprehensive overview of the IVIM method is provided in the following chapter). IVIM-based perfusion measurements are gaining increasing acceptance, particularly in the field of oncology (37). The perfusion fraction, IVIM-f, has demonstrated clinical value in discriminating between high- and low- grade brain gliomas (38) and is prognostic for survival in brain gliomas (39). The pseudo-diffusion coefficient, IVIM-D*, which macroscopically describes the incoherent motion of blood within the capillary network (40), has additionally shown efficacy in the discrimination of low- and high- grade tumours (41). The IVIM method has demonstrated a moderate correlation to other perfusion methods (42). Furthermore, the IVIM methodology is fundamentally different from other perfusion techniques; hence, the measured perfusion information obtained could be complementary to these other perfusion methods.

The IVIM method is confounded by some limitations. There is no consensus as to the number of data points (b-values) or the distribution that should be used (43). Post-processing techniques, such as the fitting method implemented can also affect the estimated parameter values (44). The impact of these factors is most evident in the IVIM-D* parameter which has the greatest measurement error of the IVIM parameters (45). The IVIM method also assumes that two compartments, water diffusion and perfusion within the capillary bed, exist within the diffusion signal. However, more compartments may be present, either due to signal mixing with other tissues (40) or additional perfusion effects (35). These challenges could potentially confound the use of some of the IVIM parameters as robust biomarkers. There is a need for a robust method which can fit multi b-value DWI without prior knowledge of the number of components and extract relevant information on the perfusion of the tissue.

1.4 Robust Biomarkers

MRI is a popular diagnostic modality with most clinical data assessed by expert qualitative review (46). Qualitative assessment can be rapid but potentially challenging when qualitative features from multiple image types require consistent interpretation (47). In addition, the results from different reviewers of qualitative data can be highly varied. Hence there is a need for more robust measurements with quantitative biomarkers (48).

Perfusion is a complex physiological process that can be measured by a multitude of different parameters, attained through a variety of imaging modalities. Although many different parameters could be complementary in their characterisation of perfusion, it is unfeasible that all will gain clinical use (49). Hence to ensure the implementation of robust biomarkers, a multitude of factors have to be considered.

Imaging biomarkers are a subset of all biomarkers and can be either quantitative or qualitative (50). Quantitative Imaging refers to the extraction and use of numerical and statistical features from a medical image (51). As defined by the Quantitative Imaging Biomarkers Alliance, organised by the Radiological Society of North America (RSNA), a quantitative imaging biomarker is:

> "*An objective characteristic derived from an In-Vivo image measured on a ratio or interval scale as indicators of normal biological processes, pathogenic processes, or a response to a therapeutic intervention.*" (52)

Several different groups associated with the development of quantitative imaging biomarkers (QIBs) (50) have issued consensus statements for guidelines for the acquisition and analysis of some QIBs. Technical validation, clinical validation and cost-effectiveness all have to be established for a potential QIB.

For the technical validation of a QIB, the robustness of the biomarker has to be validated. This is established through determining the QIB's bias (accuracy), precision (variability), and determining its inherent reliability (confidence interval) in parameter measurements. In order to interpret the results from multiple studies, the acquisition protocol needs to be standardised (53). For DWI, this requires a consensus on factors such as magnetic field strength and maximum slice thickness (54).

In the initial stages of biomarker discovery, the precision and bias of a parameter are considered (55) via computer simulations, before being validated in phantoms, preclinical or clinical datasets (52). QIBA recommend that quality control metrics such as parameter mean, standard deviation, coefficient of variation, bias estimate and noise estimation are implemented for technical validation (56).

For imaging biomarkers, clinical validation occurs simultaneously alongside technical validation. Clinical validation of QIBs is conducted by assessing factors such as the sensitivity and specificity (57) of the new biomarker. Subsequent technical validation is then required by assessing multicentre reproducibility (58). At every stage in the development of a new QIB, the cost-effectiveness, i.e. the cost of scan time and assessment, has to be considered (50). Any new QIB should strive to adhere to these image biomarker guidelines.

1.5 Project Aims and Objectives

The overall aim of this work was to develop a new MR method to probe and understand multicomponent diffusion and perfusion within biomedical systems. The project focuses on a novel fitting method for DWI data. The method is validated by investigating if the number of components in the diffusion signal can be correctly determined. The model's coefficients are investigated as potential imaging biomarkers with comparisons to DSC-MRI, the current standard for MR perfusion.

1.5.1 Objectives

1. To develop a new fitting model for multi- b-value DWI data based upon a modified version of the Auto-Regressive Moving Average (ARMA) model. Such a model will have the ability to fit a variable number of components.

2. To investigate the performance of the new method to fit multicomponent data and determine the number of components. Compare the results to multiexponential fitting methods currently implemented. Explore computerised simulations modelling tissues with different water motions, including blood flow.

3. To explore the biophysical origin of the perfusion effects measured with DWI. Compare the perfusion MR parameter cerebral blood volume (estimated using Dynamic Susceptibility Contrast) to perfusion related parameters obtained with DWI.

4. To further develop the mathematical formalism of the new method. Compare the coefficients of the new method to the parameters of multi-exponential fitting methods. Derive the IVIM model parameters from the coefficients of the new method.

1.6 Thesis Structure

In Chapter 2, a background into MR physics and DWI is provided. Common diffusion models, such as the ADC and IVIM model are highlighted. The factors confounding image quality and the effects these have on biomarker reproducibility are considered. Some of the pitfalls of the IVIM model are highlighted, particularly in low perfused tissues such as the brain. The relation of perfusion parameters to the IVIM model and the success of correlation studies is discussed. Multiexponential fitting methods, in general, are explored along with model selection techniques. Finally, the ARMA Model and its potential for modelling multi-exponential data is introduced.

In Chapter 3, the ARMA model is introduced as the ADAPT model, modified for DWI signals. A full mathematical formalism is provided and discussed. The methodology for using ADAPT to determine the number of components in the diffusion signal is presented. A partial volume effects model, combining white matter and cerebrospinal fluid signals is investigated and the results compared to those of multi-exponential fitting methods.

In Chapter 4, the perfusion related measurements from DWI, including the ADAPT parameters, are explored. The correlation between the ADAPT(1,1)-$\alpha1$ and DSC-CBV parameters is investigated and compared to the correlation between IVIM-f and DSC-CBV across a patient cohort. The ADAPT method is used to determine the number of components in the diffusion signal. The impact of the number of components upon the correlation strength is investigated.

In Chapter 5, the IVIM parameters are fully derived from the ADAPT coefficients with a particular focus on IVIM-D*. The ADAPT fitting method is compared to the multi-step, non-linear, least-square fitting algorithm commonly used to estimate the IVIM parameters. Both fitting methods investigate simulated white matter and grey matter brain models, considering the accuracy, precision and bias for a range of Signal to Noise Ratio (SNR) levels. Once optimised, the fitting methods are applied to In-Vivo data and compared.

Chapter 2

Theory

2. Theory

This chapter provides an overview of the fundamentals of MR physics and the phenomenon of diffusion. The methodology for attaining MR images sensitive to diffusion is explained. Modelling of the diffusion signal in order to gain clinically relevant biomarkers, also related to perfusion, is discussed. The challenges that different diffusion models encumber are explored and the desire for a novel fitting method established.

2.1 MR Physics

2.1.1 Magnetic Characteristics of the Nucleus

The magnetic properties of a nucleus are affected by spin, an intrinsic quantum property of the particle's angular momentum, and the electrical charge distribution of the protons and neutrons. Although neutrons have no overall electrical charge, the distribution of charge is inhomogeneous. This inhomogeneity, in addition to the nuclear spin, leads to the neutrons generating a magnetic field that is equal and opposite to that generated by the protons.

The magnetic characteristics of a nucleus can be defined by the nuclear magnetic moment, a vector dictated by the pairings of constituent protons and neutrons. Individual protons and neutrons have an associated magnetic moment and spin ½. The angular momentum of nucleons tends to form pairs acting as single entities with intrinsic angular momentum. If the sum of the number of protons (P) and neutrons (N) are both even, then no magnetic moment is observed. However, if P is even and N is odd, large integer spins are associated with the unpaired nucleons and a magnetic moment is observed (59). If P is odd, a half-integer spin is observed associated with the odd proton.

Several elements present in biological tissue can generate a magnetic moment. Within biological tissues, hydrogen is the best candidate for generating such an MR signal due to its high isotopic abundance, a strong magnetic moment and being heavily concentrated in water and lipids (60). Although other elements, such as ^{23}Na and ^{13}C, have been used to image the body, the proton is primarily used to generate the MR signal.

The spin of the proton can be considered as a spinning gyroscope that is electrically charged; this creates a loop of electrical current about the spinning axis which can interact with external magnetic fields as well as being capable of generating its own. If many unbound hydrogen atoms are considered then, due to their thermal energies, they will assume a random orientation of magnetic moments, resulting in no net magnetic moment being observable. Should an external magnetic field be applied, the magnetic moment vectors will align themselves as parallel or anti-parallel at two discrete energy levels to the field (Figure 2.1).

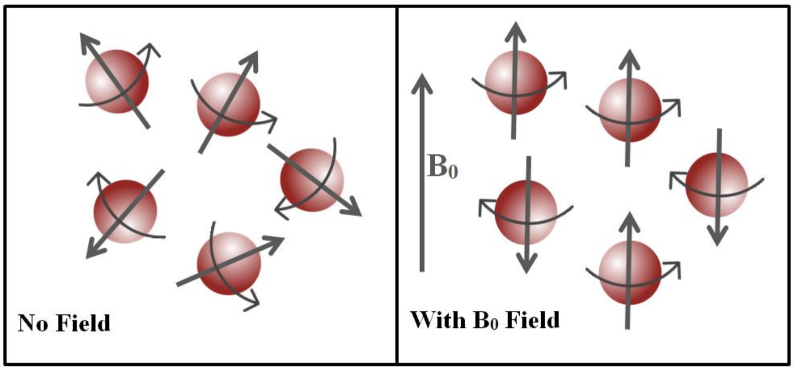

Figure 2.1: A) Nuclei spins are randomly orientated. B) In the presence of a magnetic field, nuclei spins align either spin aligned or spin opposed to the magnetic field.

A small majority of spins exist in the lower energy state; the energy gap between the two states depends upon the strength of the applied magnetic field (Figure 2.2). Increasing the magnetic field increases the number of spin protons in the lower energy state and thus creates an observable magnetic moment, leading to the magnetisation, M_0, of the nuclei that runs parallel to the magnetic field.

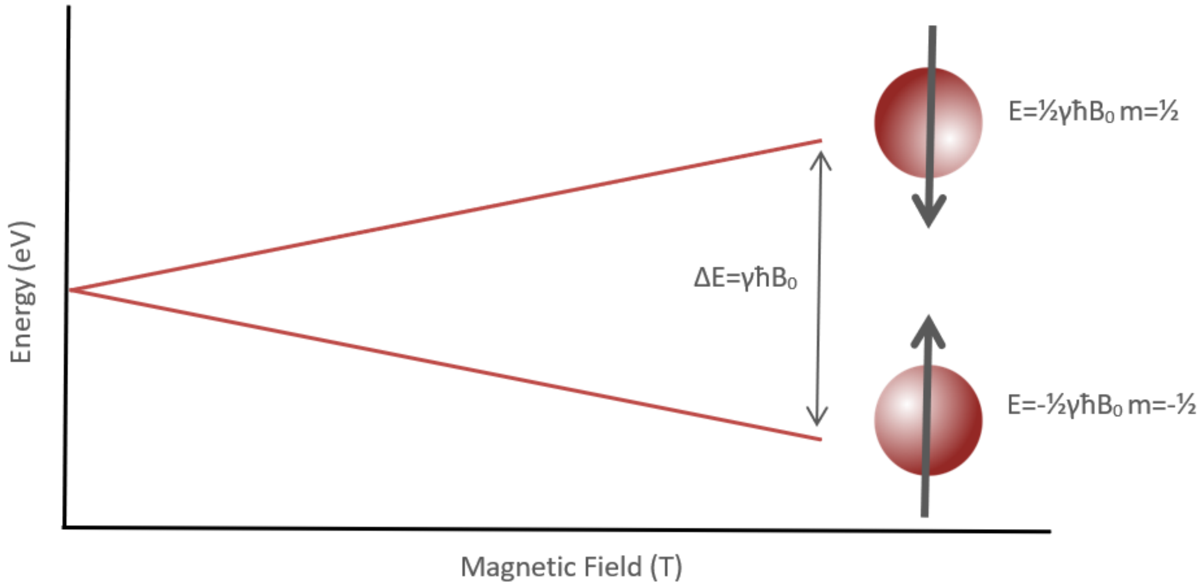

Figure 2.2: Energy of the interactions between a hydrogen nucleus and the applied magnetic field, B_0. Two possible spin states with two different energies are possible with the energy level dependent upon the magnetic field, the reduced Planck constant ħ, the gyromagnetic ratio γ and the spin energy state either ½ or -½.

However, the axis of the nucleus does not perfectly align with the applied magnetic field due to its angular momentum, resulting in the nuclei having a transverse magnetic moment component. This component has no fixed direction and can be at any angle perpendicular to B_0. The angular momentum causes the nucleus to precess about the direction of B_0. The angular frequency of this precession is known as the Larmor frequency, ω_0, dictated by the Larmor equation:

$$\omega_0 = \gamma\beta_0 \tag{2.1}$$

Where γ is the gyromagnetic ratio, a specific constant determined by the element. For a hydrogen nucleus, a proton, γ is approximately 2.68×10^8 rad s^{-1} T^{-1}. Due to the random distribution of proton alignments, there is no net magnetisation across the nuclei in the transverse direction to the magnetic field.

2.1.2 Applying a Radio Frequency Pulse

The nuclei can be distributed from equilibrium by the introduction of a secondary magnetic field, B_1. To excite those nuclei in the lower energy state, they must receive energy equal to the energy difference between the two energy states- hence B_1 must oscillate with a frequency equal to that of ω_0. By applying B_1 perpendicular to B_0, the net magnetisation M_0 is rotated and begins to precess about the sum direction of B_0 and B_1. For imaging purposes, B_1 is required to be rapidly switched on and off; so it has a much smaller magnitude than B_0. The total magnetic field changes with time as B_1 rotates and M_0 precesses about the vector sum of these two fields (Figure 2.3).

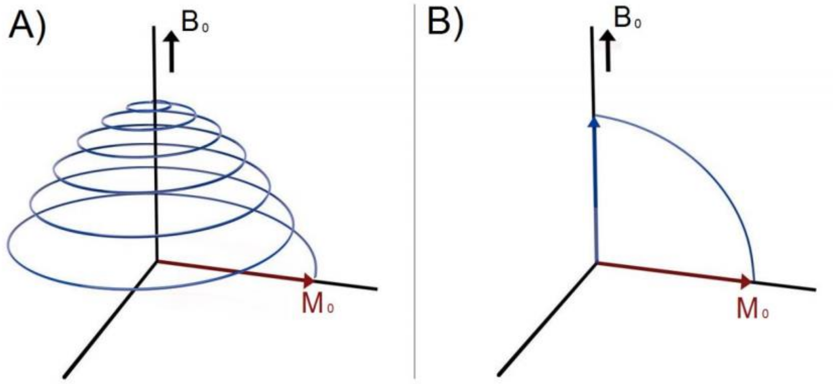

Figure 2.3: Precession of net magnetisation A) Stationary reference frame. B) Rotating reference frame- rotates at the Larmor frequency. M_0 rotates around the B_1 vector and appears stationary about B_0.

B_1 is applied via a low energy radio frequency (RF) pulse. After the pulse, excited nuclei relax back to equilibrium and release detectable energy equal to that of the RF pulse. The number of excited nuclei, and therefore the size of the detectable signal, is dependent upon the magnitude and duration of the RF pulse. By applying B_1 at ω_0, M_0 can be rotated away from B_0. The angle by which M_0 rotates away from B_0 is known as the flip angle. The rotating magnetisation induces an electrical signal in a receiver coil within an MRI scanner; this is the signal that creates the MR Image. This signal oscillates at the same frequency as ω_0, its strength dependent on the angle of M_0 from B_0. The biggest change in signal is observed when M_0 is perpendicular to B_0, creating the largest fluctuation in the magnetic signal. Consequently, the MRI signal is dependent upon the magnitude of magnetisation and its flip angle.

2.1.3 Relaxation

Following the RF pulse, nuclei lose magnetic energy and magnetisation returns back to equilibrium, a process known as relaxation. The phenomenon can be expressed through two components with the longitudinal relaxation being a vector parallel to B_0; this vector relaxes with time T1. In T1 relaxation the longitudinal component of M_0 is recovered as energy is lost to the surrounding lattice; T1 is the time taken for the net magnetisation to recover from zero to (1-1/e) of the maximum value, approximately 63%. T1 relaxation is modelled by the equation:

$$M_z = M_0\left(1 - e^{-t/T1}\right) \tag{2.2}$$

where t is time and M is the net magnetisation.

For T1 relaxation to occur, the energy exchange from the nucleus to the surrounding material is stimulated through the interaction with another magnetic field close to the Larmor frequency. Typically, it is neighbouring protons that induce this relaxation. For molecules with unrestricted motion, such as pure water, a wide range of frequencies are possible. At any given time, only a small fraction of the water molecules will be at the rotational speed needed for the energy exchange. Consequently, water has a long T1. In fat, the water molecules interact with the long carbon chains resulting in a lower resonant frequency. Fat molecules rotate slower than water molecules, resulting in a shorter T1.

The transverse relaxation is the decay of the transverse component of M_0, as energy is transferred between the spins, and has a relaxation time of T2. T2 relaxation occurs at a much quicker rate than T1 and is modelled by:

$$M_{xy} = M_0 e^{-t/T2} \tag{2.3}$$

T2 is the time taken for the transverse magnetisation to decay by (1/e), ~37%. T2 relaxation occurs via dipole-dipole interactions with other ^{1}H nuclei. As the T2 signal is known to exponentially decay, by measuring at time t after relaxation the signal S(t) will be given by:

$$S(t) = S_0 e^{-t/T2} \tag{2.4}$$

Such that S_0 would be the signal measured instantaneously after relaxation. Hence the signal detected is weighted by T2.

Like T1, a tissue's T2 is characterised, in part, by the speed of the molecular rotations. Consequently, moving water molecules have longer T1 and T2 values, whereas water with restricted movement, and lipids, have shorter relaxation times. Subtle differences in relaxation times amongst tissues allows for sensitive imaging. For example, white and grey brain matter can be readily distinguished on conventional MR images with relaxation observed via either the T1 or T2 signal.

2.1.4 Magnetic Field Gradients

To differentiate between all the MR signals generated from different locations, it is necessary to impose a spatially varying magnetic field gradient (Figure 2.4). This gradient varies linearly and results in the total magnetic field being linearly dependent on the location within the scanner. The exact magnetic field strength at location r_i:

$$B_i = B_0 + G_T \cdot \boldsymbol{r_i} \tag{2.5}$$

Where G_T is the gradient amplitude.

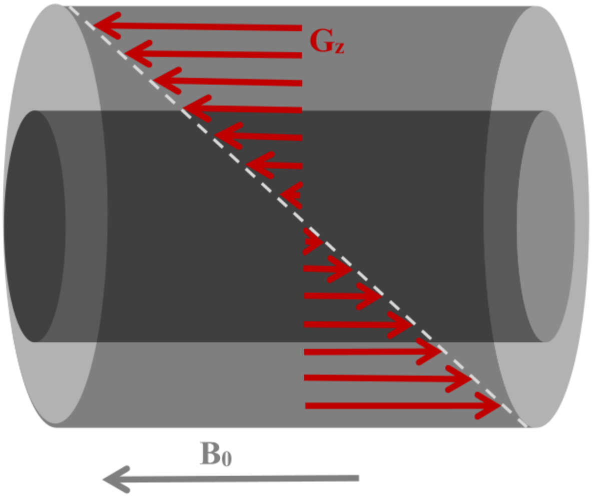

Figure 2.4: Spatially varying gradient field, G_z, within the scanner. The gradient varies linearly and results in the total magnetic field being linearly dependent on its location within the scanner.

This results in an additional term to the Larmor equations:

$$\omega_i = \gamma(\beta_0 + G \cdot \boldsymbol{r_i}) \tag{2.6}$$

Hence the resonant frequency of each proton is unique and varies as a function of location. By only exciting nuclei within a narrow range of frequencies, with an RF pulse that matches their Larmor frequency, selected spins can be isolated across a thin slice. This process is referred to as slice selection (Figure 2.5).

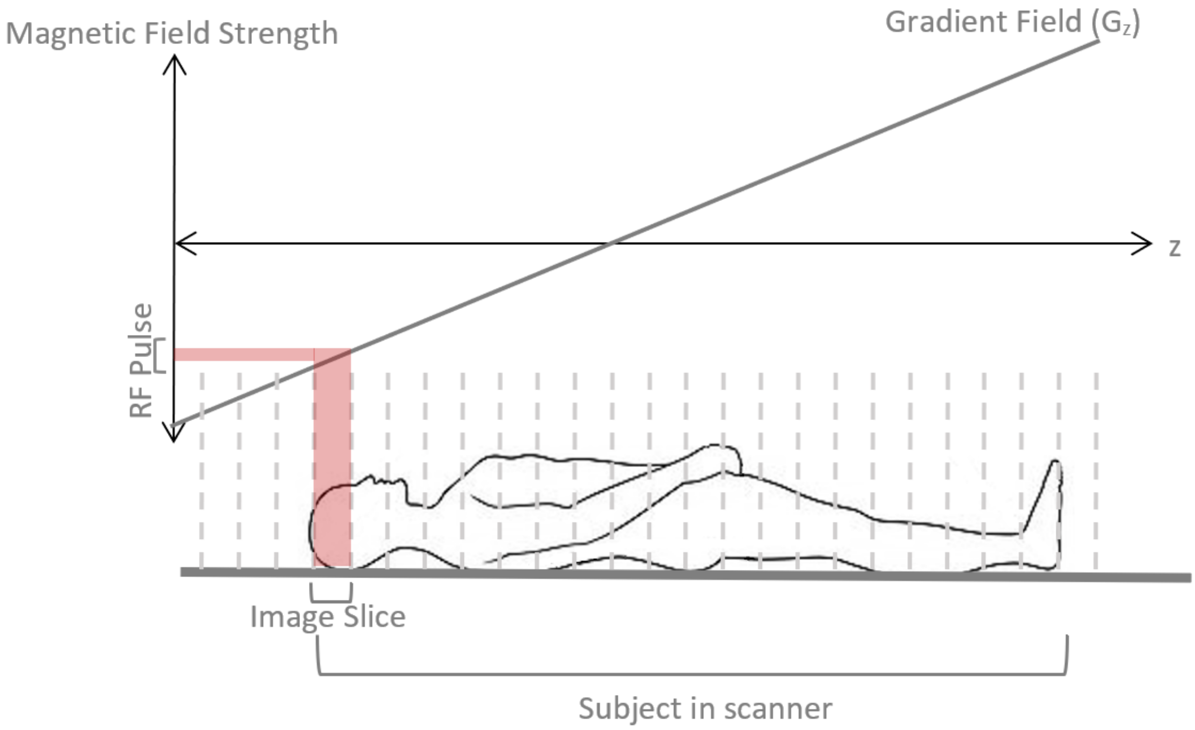

Figure 2.5: Slice selection with selective nuclei excitation.

The thickness of the slice is determined by the magnitude of the slice selective gradient (G_{ss}) and the range of frequencies within the RF pulse. The orientation of the slice is dependent upon the orientation of G_{ss} (i.e. G_z). The slice selection process provides spatial resolution in the direction of G_{ss}; the number of images created will be equivalent to the number of slices. To gain in-plane resolution in x and y- spatial encoding is required. This is done using two gradients: phase encoding and frequency encoding. These supplementary field gradients, whilst applied, temporarily change the resonant frequencies of the protons. Once switched off, the protons return to their original precessing frequencies but the phase induced remains. Phase encoding alters the phase of the voxels in the y-direction. This is done using another gradient and is similar to the process used for slice selection. The induced phase shift is proportional to the duration of the gradient and the position along the y-direction. After phase encoding, frequency encoding is performed where a frequency shift operator is used to change the angular frequency of the spinning protons in the x-direction. The frequency encoding gradient, increases linearly in the x direction, predictably distorting the magnetic field such that the resonant frequency varies as a function of position. This is performed using a similar method to G_{ss} and phase encoding. The bandwidth of these additional RF pulses will determine the resolution of the image. For each voxel in the image, we will have a specific phase and a specific angular frequency associated to the nuclei within that voxel (Figure 2.6).

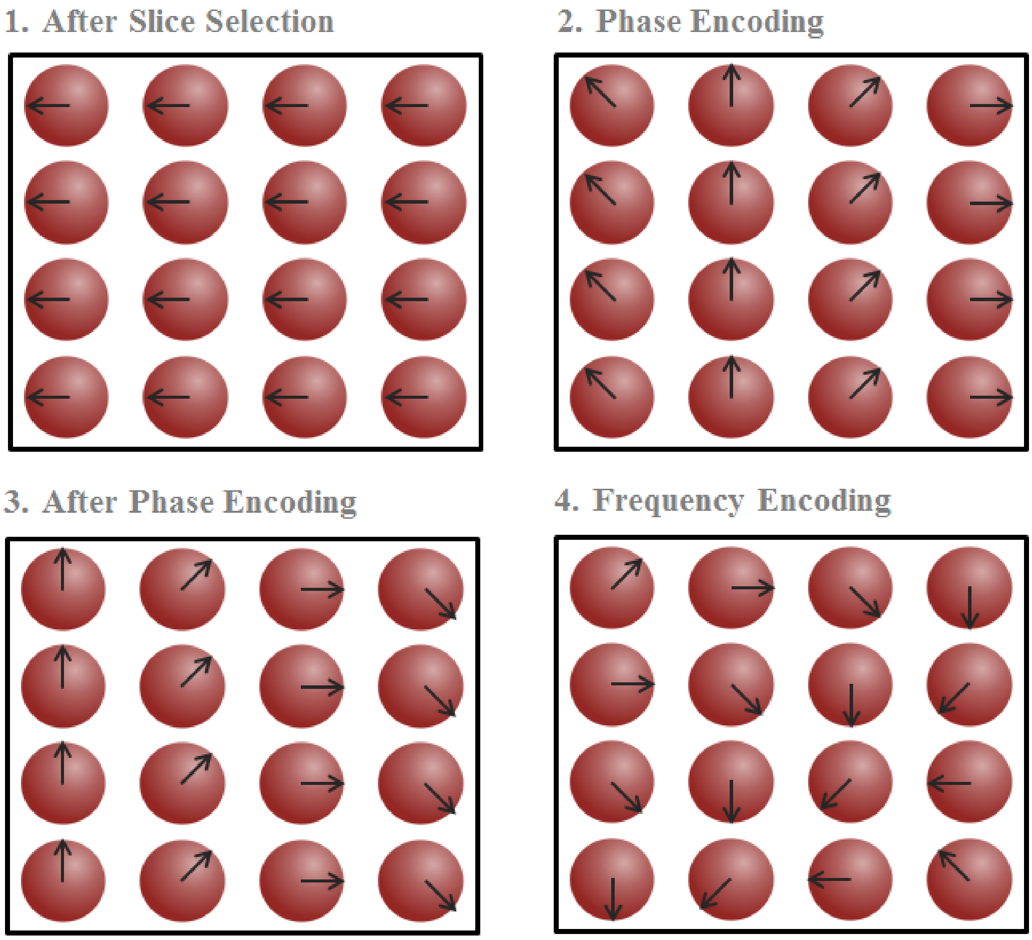

Figure 2.6: Spatial encoding: the effects of phase and frequency encoding on nuclei spins.

2.1.5 Creating an Image from the MR Signal

When the RF pulse is switched off, both T1- and T2- relaxation occur. The transverse relaxation and dephasing caused by small variations in the magnetic field result in the MR signal decaying. To ensure that the signal is detected before it decays considerably, a signal echo is created by temporarily reversing the dephasing. Two possible techniques can create a signal echo: spin-echo and gradient-echo. The spin-echo technique is executed by applying a subsequent 180° RF pulse after the initial 90° RF. As the signal begins to dephase after the 90° RF, the 180° RF pulse inverts the nuclei magnetisation and phase signal such that as the signal continues to propagate it becomes rephased. Spin echo allows more time for the signal to be detected (Figure 2.7).

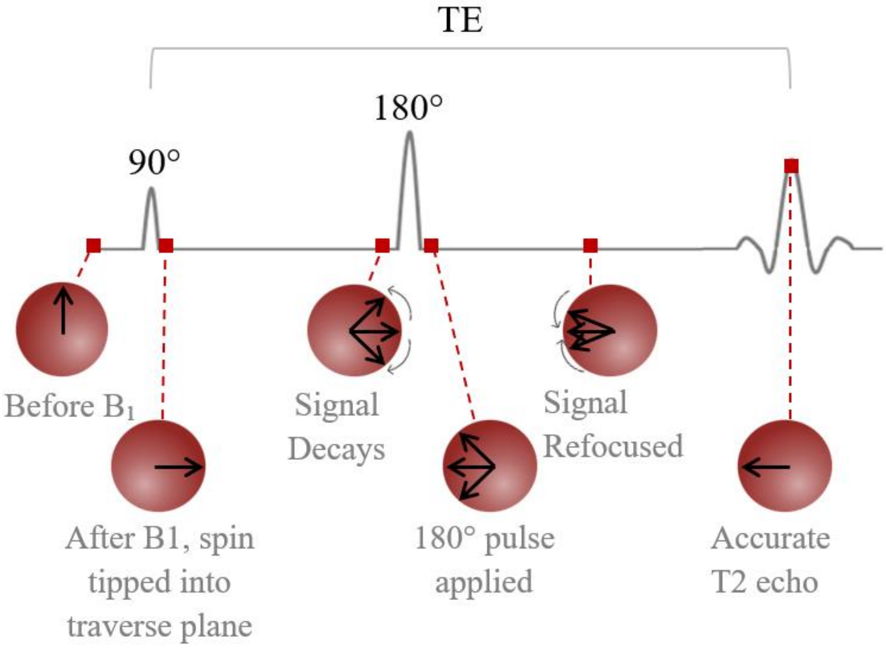

Figure 2.7: Spin Echo: the effects of the pulse sequence on nuclei spin.

The gradient echo technique works by applying a magnetic field gradient upon the nuclei and then rapidly applying another gradient in the opposite direction. The two field gradients cancel out, and the transverse magnetisation is brought back in phase, creating a strong MR signal. The time from the peak of the first RF pulse to the middle of the echo is referred to as echo time- TE. The repetition time, TR, is the time between successive 90° RF pulses. For spin encoded images, the TE and TR are used to determine the image contrast. The detected signal S can be approximated by:

$$S = K \cdot [H] \cdot \left(1 - e^{-TR/T1}\right) \cdot e^{-TE/T2} \tag{2.7}$$

Where K is a scaling factor and [H] is the spin density. When TE is short relative to T2, the echo occurs before any substantial T2 relaxation has occurred. However, when TE is long, the T2 signal decays exponentially, and the contrast between different tissue types, exhibiting different T2 signals will be substantial. A T2-weighted image is acquired with a long TR and TE. If TR is long relative to T1, the signal will have time to fully recover from the RF pulse and will have no dependence on T1.

However, if the repeating TR pulse is so rapid such that the nuclei haven’t fully relaxed-then the longitudinal magnetisation observed will be dependent upon T1. A T1-weighted image is acquired with a short TR and short TE. For the repeated RF pulse technique, the sensitivity of the signal can be controlled for different tissues by changing the interval time between repeated pulses.

The attenuation in the signals leads to a decay in the voltage induced in the receiver. The signal measurements are stored in a large matrix known as k-space- an array of raw data representing spatial frequencies in the MR image. Each element contains information related to the whole image space with the k_x and k_y axes specifying the spatial frequencies in the (x,y) direction. K-space is converted to image space using a Fourier transform.

To reduce the effects caused by patient movement, the slice can be acquired rapidly with a single, or a small number, of excitations. This mode of acquisition is referred to as Echo Planar Imaging (EPI). Different methods exist for acquiring k-space, but by applying the frequency encoding gradient, with an intermittent phase encoding gradient, all of k-space can be acquired with a rectangular zig-zag pattern (Figure 2.8).

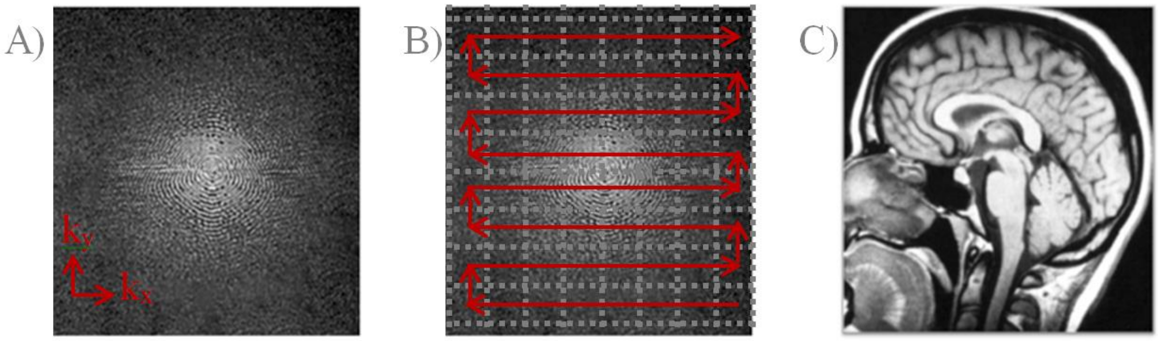

Figure 2.8: A) Image is acquired in k-space B) Using a zig-zag transversal C) Converted to image space using a 2D Fourier Transform. (Edited. Original images Courtesy of Allen D. Elster, MRIquestions.com)

2.1.6 Image Quality

A multitude of factors affect MR image quality. The image resolution is determined by the size of the 3D voxel. The smaller the voxels, the greater the resolution. Image resolution can be increased by reducing the slice thickness and increasing the matrix size (number of voxels) relative to the field of view (FOV):

$$Voxel\ Size = \frac{FOV}{Matrix\ Size} \times Slice\ Thickness \tag{2.8}$$

Increasing the matrix size increases spatial resolution in the xy plane but also increases the scan time due to more voxels needing to be acquired. The smaller voxels also result in a decreased signal due to there being fewer nuclei. Increasing the slice thickness will increase the signal intensity but result in a poorer resolution in the z plane. Thicker slices can also result in partial volume effects, where the signals from different tissue types mix.

A high image resolution is desirable for improved image quality and enables the delineation of tissue structures and small pathologies. However, image resolution is inversely proportional to the signal to noise ratio (SNR) level. An MR image is created from the MR signal, containing useful information, and noise, signals containing no useful information. The noise causes static fluctuations in the image intensity and arises from electrical resistance, within the MR hardware, and electromagnetic noise, from the movement of charged particles within the subject. For the signal coming from the biological tissue to be distinguishable from the background noise, the SNR level needs to be sufficiently high. If the image resolution is too high, the poor SNR level will cause image graining (61) and the scan time will be unacceptably long.

SNR levels can be improved by increasing the number of signal averages (NSA). If the slice acquisition is rapidly repeated, the amount of signal detected can be increased. An image can be calculated from the average of the acquired signals, reducing the effects of artefacts. Doubling the NSA improves the SNR by $\sqrt{2}$. Increasing the NSA greatly increases the scan time; doubling the NSA would double the acquisition time. Hence, for a clinically realisable scan, there still needs to be a trade-off between image resolution and SNR.

The MR hardware also impacts image SNR. Given Faraday’s law of induction (62), the voltage generated in the receiver coil is proportional to the B_0 field strength. In theory, the SNR of the MR Signal is proportional to B_0. Clinical 3T MRI systems are becoming commonplace, with the added value of 3T over 1.5T well documented (63)(64). Hardware developments will continue to improve SNR over the coming decades, with 7T for clinical use recently approved (65).

Localised RF coils are the receivers, and sometimes transmitters, of the B_1 field. The SNR level is greatly improved when the coil is as close to the anatomy of interest as possible. Hence there are a range of dedicated coils for different regions of the body. For MR imaging of the brain, a dedicated head coil is used. The RF coil is comprised of multiple channels, where the output of each channel provides a partial view of the overall image. The more channels there are, the better the image quality and the faster the acquisitions (66). However, to increase the number of channels, multiple small coils are required. The smaller the coil, the shorter the penetration depth (67); thus, many channels are suitable for cortical imaging but not for imaging deep brain structures. Consequently, a compromise is required, and 32-channel head coils are currently in routine use.

A common technique implemented in MR protocols is parallel imaging. By using the known sensitivities and locations of the receiver coils, the spatial location of the MR signals can be informed. This enables the number of phase encoding steps to be reduced- greatly decreasing the scan time. However, such a technique also reduces the SNR. SENsitivity Encoding (SENSE) is a widely used parallel imaging technique which still observes a degradation in SNR but attempts to suppress the artefacts created by the subsampling (68).

The receiver bandwidth is the range of frequencies collected during frequency encoding of RF pulse and is an adjustable parameter. Reducing the bandwidth increases SNR. However, if the receiver bandwidth is set too low, susceptibility artefacts and chemical shift artefacts can occur (69).

Another method for increasing SNR is the addition of slice gaps. The slice profiles generated by the RF pulses are not perfect rectangles. Exciting once slice can cause partial excitation in the neighbouring slice. This interference is known as cross-talk and reduces the SNR (70). By introducing a small gap between neighbouring slices, the effects of cross-talk can be avoided. This is at the expense however, of the information on the slice gaps not being acquired.

MR hardware developments have led to significant SNR improvements over the past decades (48). Future developments in scanner hardware and technology will undoubtedly continue this trend.

TE and TR also affect SNR. A long TR ensures the longitudinal magnetisation to approach its maximum, increasing the signal and thus the SNR. However, the TR cannot be too long if T1-weighting is desired. A long TR would also increase scan time. A short TE, ensuring the transverse decay is rapid, can also increase the SNR. However, a short TE is only an option for T1-weighted images due to the reduction in T2 effects. Hence changes to TE and TR for SNR improvement need to be mindful of the sequence being implemented.

2.1.7 Measuring SNR

It is important to know the SNR of an MR image when clinically relevant biomarkers are being calculated. The SNR can have a profound impact on the variance of a calculated parameter. It is paramount that the robustness of a parameter at relevant SNR levels is investigated before clinical implementation. Hence the SNR of the MR Image should be reliably measured.

Magnitude images are most commonly acquired in MRI; the problems of phase artefacts are avoided by discarding the phase information. The noise in the real and imaginary parts of the MR signal is assumed to have a Gaussian distribution with zero mean (71). The noise is assumed to be uncorrelated between real and imaginary voxels (72). However, the magnitude image is generated through a non-linear transformation, calculating the magnitude from the real and imaginary images. This non-linear mapping means the noise distribution is no longer Gaussian, instead governed by a Rician distribution (73). However, for the SNR attained in MR Images, the Rician noise can be well approximated by a Gaussian distribution (71)(74).

Conventionally, the SNR can be calculated from the quotient of the mean pixel intensity, S, taken from a region of interest (ROI) within the desired tissue, and the standard deviation, σ, from a ROI (or multiple ROIs), drawn in the background of the image.

$$SNR = 0.655 \cdot \frac{S}{\sigma} \tag{2.9}$$

The 0.655 term is due to the Rician distribution; all noise terms are positive, so σ is reduced. This method for measuring SNR assumes that the noise is distributed homogeneously across the image. However, this isn’t true for parallel imaging techniques (75), where:

$$SNR_{parallel} = \frac{SNR}{g\sqrt{R}} \tag{2.10}$$

R is the acceleration factor, which quantifies the reduction in the number of phase encoding steps; g is the geometric/g factor characterising the specific geometry of the RF coil array (76). g is not a constant but a spatially dependent parameter. Hence the SNR is locally dependent.

For SENSE images, SNR can be measured using the National Electrical Manufacturers Association (NEMA) method (77). If a slice is successively imaged twice, with the same protocol, the locally dependent noise can be calculated from the difference between the two images. SNR can be calculated from the quotient of the mean pixel intensity, from a ROI drawn on both images, and the standard deviation of the ROI, drawn in the same location, of the difference image (71):

$$SNR_{diff}(n_1, n_2) = \frac{S_{diff}}{\sigma_{diff}} = \frac{\frac{1}{2} mean\big(S(r, n_1) + S(r, n_2)\big)}{\frac{1}{\sqrt{2}} stddev\big(S(r, n_1) + S(r, n_2)\big)} \qquad (2.11)$$

Where S is the signal intensity, r=(x,y,z) is the position within the ROI, and n is the repetition number. The NEMA method requires multiple acquisitions. For time-sensitive scans, where only one acquisition is obtained, measuring SNR for parallel imaging is problematic. However, if NSA ≥ 2 and presuming the data from each of the acquisitions can be individually accessed, this is not an issue.

If multiple acquisitions are obtained, the noise of a single-pixel can be expressed by the stochastic variations in signal intensity. The SNR of the ROI can be calculated from the pixel-wise standard deviation across multiple acquisitions.

$$SNR_{multi}(r) = \frac{S_{multi}}{\sigma_{multi}} = \frac{mean\big(\sum_{n=1,\ldots,N}^{N} S(r, N)\big)}{stddev\big(\sum_{n=1,\ldots,N}^{N} S(r, N)\big)} \qquad (2.12)$$

For all of these methods, the SNR measured is dependent upon the location of the ROI. SNR is tissue and sequence-dependent. For example, on a T2-weighted image of the brain, grey matter appears brighter than white matter with a greater signal intensity and thus a higher SNR. The size of the ROI should be large enough to ensure that the variations in signal intensity are sufficiently measured. However, this can be restricted by the anatomy of the structure of interest. To ensure that the reported SNR is not biased to the ROI, multiple ROIs (~5) should be considered across the tissue of interest. Additionally, SNR measurements are dependent upon how they are defined and quantified. Hence, the methodology for measuring SNR, the size of the ROI and the number of ROIs considered should be reported with any SNR measurement.

2.2 Diffusion-Weighted Imaging (DWI)

2.2.1 The Physics of Diffusion

Molecules within biological tissue can have active movement, such as bulk flow. Alternatively, the movement of molecules can arise from diffusion- purely random translational motion. Due to the thermal energy of the molecules, they can randomly move around and collide with one another, with no overall net direction of flow. This phenomenon is known as Brownian Motion (78), where the movement of particles is governed by a Gaussian distribution. Diffusion is defined as the net movement of molecules from an area of high concentration to an area of low concentration. The mechanisms of diffusion are described by Fick's first law (79): molar flux due to diffusion is proportional to the concentration gradient. From this law, the parameter D arises, the diffusion coefficient (mm^2/s). D measures the average area a group of particles will move in unit time.

The diffusion of water molecules in biological tissue is an interesting phenomenon to observe. For free water at 37°C, that is no barriers interfere with its motion, Gaussian motion is assumed, the diffusion coefficient is 3×10^{-3} mm^2/s (80). Unconstrained water molecules freely diffuse via Brownian Motion. However, in tissue, the movement of water molecules is restricted by cell membranes and macromolecules resulting in a smaller diffusion coefficient (Figure 2.9). The restriction is characteristic of the environment in which the water molecules reside (81). For tissues with strongly defined membranes and high cellular density, as typical with higher-grade tumour tissue, water molecules are restricted both within and around the cells. In comparison, tissues with a low cellular density and with poorly defined membranes allow for a greater level of diffusion. This enables a particular tissue type to be identified by the degree of diffusion (82). Hence the movement of water can be used as a contrast for biological tissue.

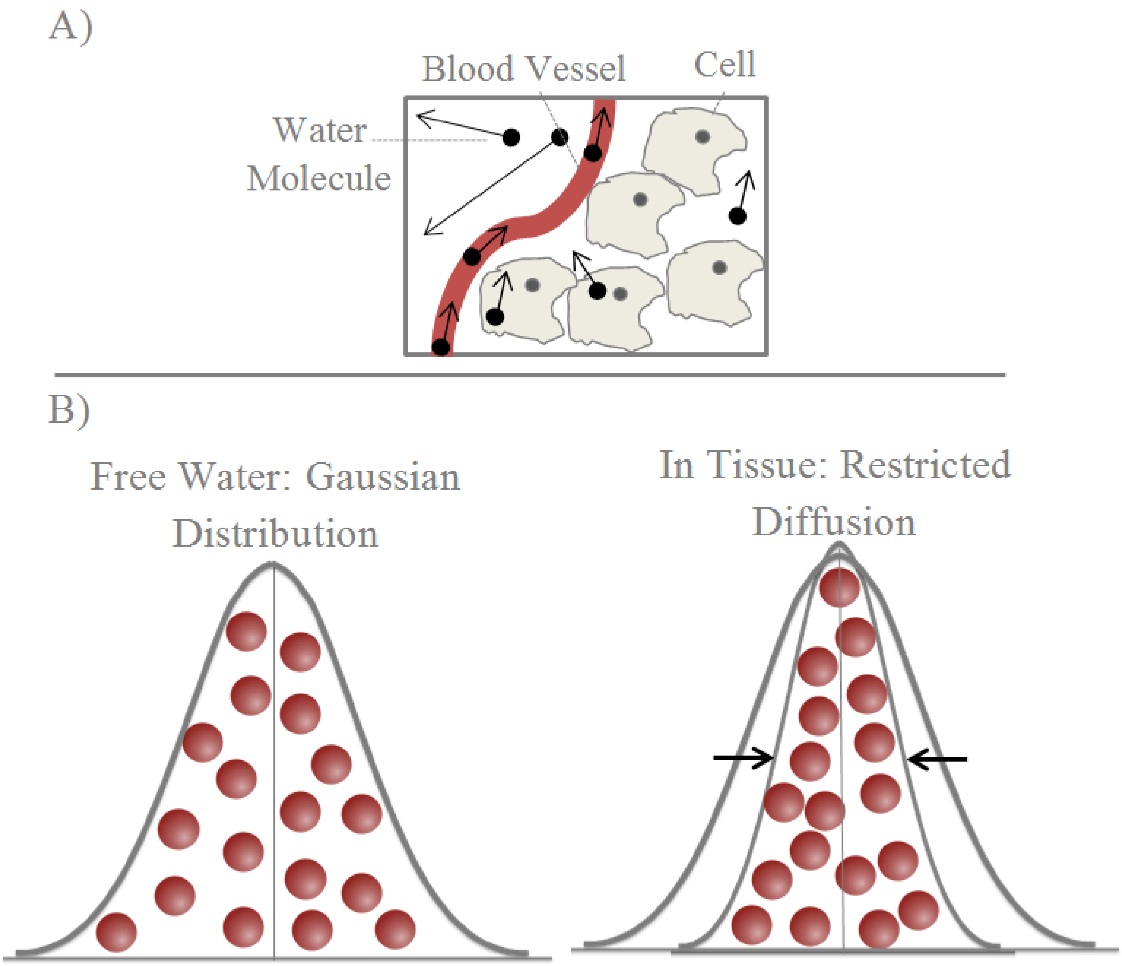

Figure 2.9: A) Movement of water molecules in tissue. B) Distribution of water molecules in unrestricted water follows a Gaussian distribution. The movement of water molecules in tissue is hindered, resulting in a restricted diffusion.

2.2.2 Measuring Diffusion with MR

By measuring the diffusion coefficient with MR, the structural environment of tissue can be probed non-invasively. The sensitivity of MR to diffusion was first documented by Hahn (1950) (83) with the spin-echo sequence (2.1.3). Most diffusion sequences are based upon the pulse gradient spin-echo (PGSE) sequence developed by Stejskal and Tanner (84) (Figure 2.10).

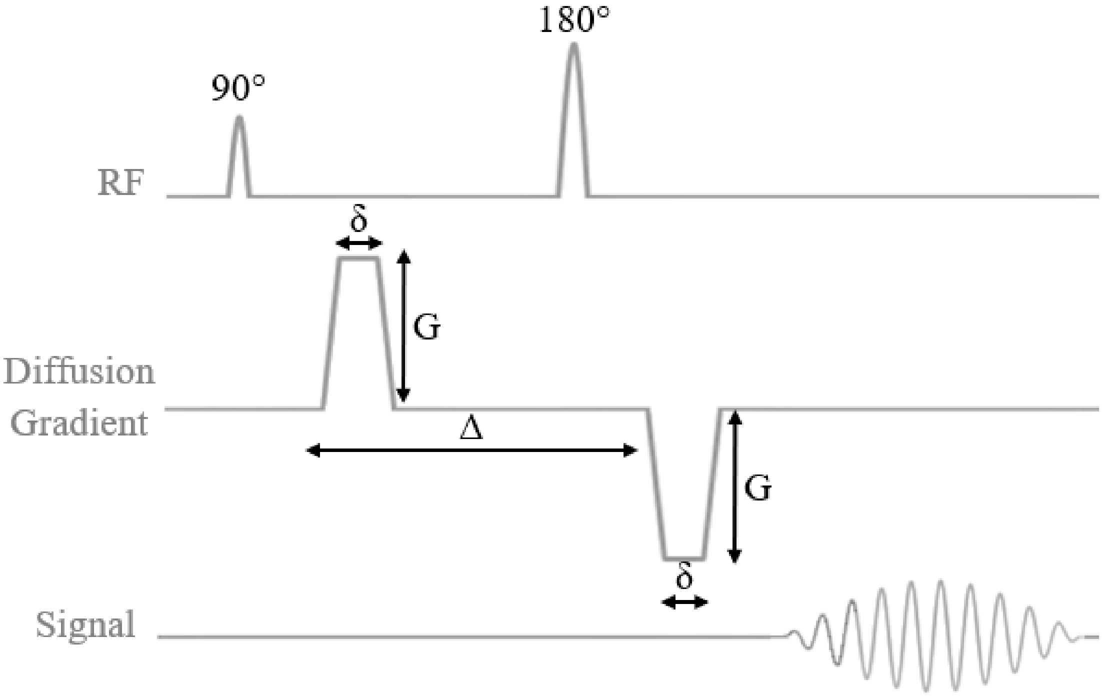

Figure 2.10: Pulsed Gradient Spin Echo (PGSE) sequence

In this sequence, diffusion sensitive gradients are applied either side of the 180° refocusing RF pulse. Stationary spins, those not undergoing diffusion, will be unaffected as any phase shift induced by the first gradient will be reversed by the second. However, any spins that move will not fully rephase, there will be a net phase shift, and the signal will attenuate. It should be noted that the detected movement of spins is not just due to diffusion processes but could be a result of any movement of comparable magnitude.

The diffusion sensitive gradients are known as b-values and are dependent upon the magnitude of the gradient, G, the duration of each gradient pulse, δ, and the time interval between the two gradient pulses, Δ- encapsulated by:

$$b = \gamma^2 G^2 \delta^2 (\Delta - \delta/3) \tag{2.9}$$

The larger G and δ are, the more dephasing happens. The larger Δ is, the more time there is for diffusion. The duration of the pulses needs to be rapid to minimise the diffusion that occurs during the pulses (85). The greater the b-value, the greater the sensitivity to diffusion and the greater the signal attenuation. The detected signal can be related to the diffusion coefficient through:

$$\frac{S(b)}{S(0)} = exp^{-D \cdot b} \tag{2.10}$$

S(0) is the detected signal with b-value= 0 s/mm^2 (no diffusion weighting) and S(b) is the attenuated signal at a particular b-value. S(0) and S(b) are weighted equally by M_0, T1 recovery and T2 decay (86). By dividing S(b) by S(0), relaxation effects are removed, and the signal is only influenced by diffusion effects. To ensure that the signal *is diffusion-weighted,* the effects of T1 are reduced by making TR long. TE is kept as short as possible, but this is limited in order to fit the diffusion gradients into the sequence. Consequently, there are some T2 effects in the diffusion image. This results in some areas on the diffusion image being bright solely due to T2 effects- a result known as T2 shine through (87).

2.3 Modelling of DWI

For the diffusion signal to be correctly interpreted, an accurate biophysical model is required such that the model's diffusion parameters can relate to the structural features and phenomena on a cellular level (88). This section will focus on isotropic, multi b-value, diffusion models. Some of these models are biophysically motivated, relating multicomponent behaviour to the tissue structure. Others are data-driven and employ statistically motivated models that ensure an optimised fit and the error in the fitting parameters minimised.

2.3.1 Apparent Diffusion Coefficient (ADC)

The Apparent Diffusion Coefficient model is the simplest of the diffusion models, assuming monoexponential behaviour. To obtain the diffusion coefficient, two b-values are required. These are typically b-value=0s/mm^2 and b-value=1000s/mm^2 (89). The large difference in b-values enables a large signal attenuation. The apparent diffusion coefficient (90) is calculated by modelling the diffusion signal with the equation:

$$\frac{S(b)}{S(0)} = exp^{-b \cdot ADC} \tag{2.11}$$

Where ADC is the apparent diffusion coefficient. It is 'apparent' in order to emphasise that the results differ from Gaussian diffusion observed in free water. For each voxel in an image, the ADC can be established from the two diffusion images. (Figure 2.11). By plotting the attenuated signal on a logarithm scale and calculating the gradient, the ADC for that voxel is attained (91).

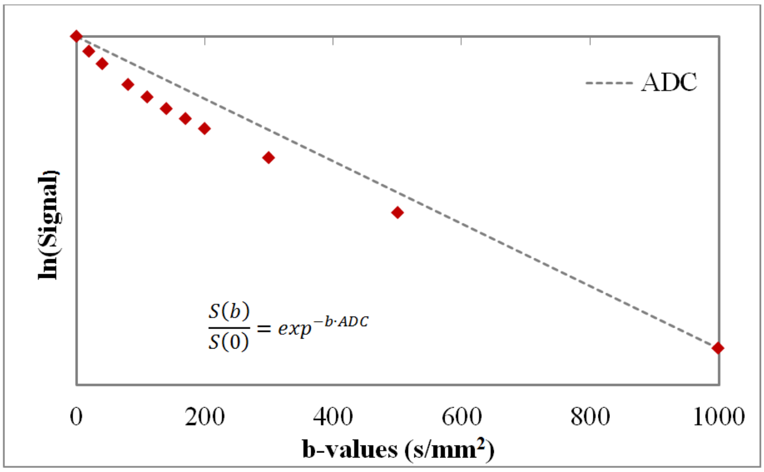

Figure 2.11: Modelling the diffusion signal with the Apparent Diffusion Coefficient model with b-values=0 and 1000s/mm^2.

Both theoretical and experimental studies have suggested that the water diffusion in tissue is characterised by multi-component behaviour (92)(93). Despite being a simplified monoexponential diffusion model, ADC is still the most commonly used model for DWI analysis (94). Requiring only two b-values, it is quick and relatively easy to interpret with most vendors providing software that automatically generates an ADC map from the raw data (95). Acquiring an ADC map is routine in most MR protocols. Despite the oversimplification of the model, the ADC provides a robust biomarker (96), and its clinical value is evident, particularly in differentiating some human brain tumours (97).

The ADC parametric maps can be assessed qualitatively by simply comparing the signal intensities of different regions for tissue characterisation (98). The ADC maps do however provide quantitative information. This can be assessed on a pixel-wise basis, but typically a mean value is taken from an ROI drawn on the ADC map (99). These quantitative values can be used to grade tumours, where higher grade tumours typically have a greater cellular density and consequently, a lower ADC value (100). In the healthy brain, the cerebral spinal fluid (CSF) has an ADC comparable to that of free water ~ 3 × 10^{-3} mm^2/s. Cortical Grey Matter has a typical ADC of 0.78 - 1.09 × 10^{-3} mm^2/s and White Matter 0.62 - 0.79 × 10^{-3} mm^2/s (101).

2.3.2 Intravoxel Incoherent Motion (IVIM) Model

Only two b-values are required to calculate the ADC. However, when multi b-value DWI is performed, that is more than two b-values are acquired, it can be seen that plotting a straight line through the signal intensities no longer explains the behaviour observed, particularly at the low b-values (> $200s/mm^2$) (102). The signal attenuation is more than expected (Figure 2.12).

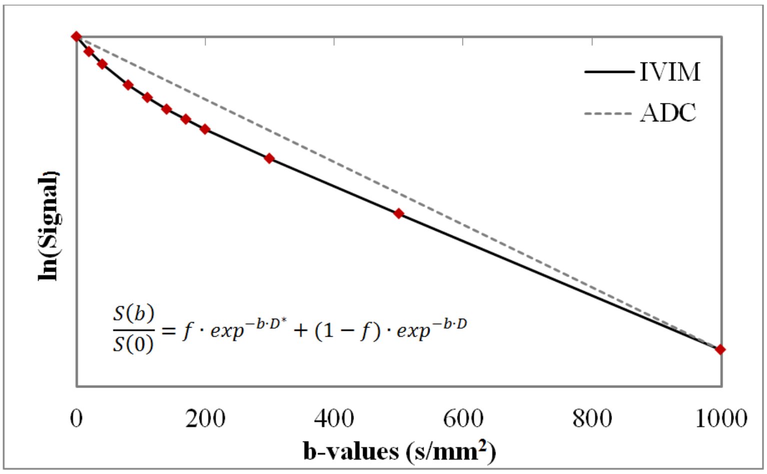

Figure 2.12: Modelling the diffusion signal with the Intravoxel Incoherent Motion Model.

This effect is theorised to be due to the bulk movement of water molecules within intravascular compartments, in particular, the movement of blood in the micro-capillaries; a phenomenon known as perfusion. A method which takes this perfusion into consideration was proposed by Le Bihan et al. (90) in 1986, known as the Intravoxel Incoherent Motion (IVIM) Method. Mathematically, the IVIM model is a bi-exponential equation which gives the relationship as:

$$\frac{S(b)}{S(0)} = f \cdot exp^{-b \cdot D^*} + (1-f) \cdot exp^{-b \cdot D} \tag{2.12}$$

where D is the diffusion coefficient, D* is the pseudo diffusion coefficient (the diffusion affected by perfusion) and f the flowing vascular volume fraction (the component of the signal attributed to perfusion) (90). The water flowing in the microcapillaries exhibits a random walk such that there is no coherent flow in any given direction (Figure 2.13).

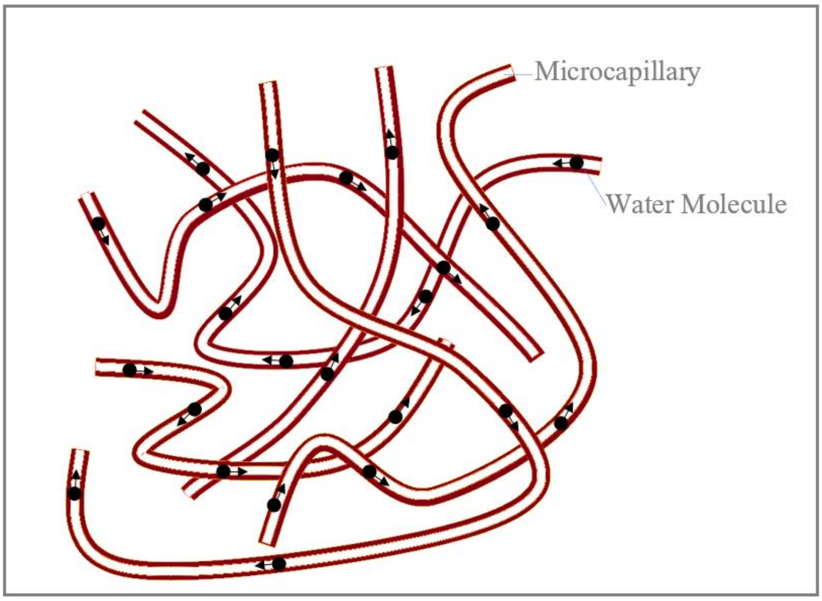

Figure 2.13: Water flowing in the capillaries mimics a random walk (Pseudo-diffusion)

The IVIM parameters have demonstrated their clinical value in the management of acute strokes (103), and in the detection, diagnosing, staging and monitoring across a range of cancers (104)(105). IVIM-f has been shown to provide added value, distinguishing between high and low-grade gliomas (38) and also differentiating different grades of pancreatic cancer (106). In some cases, the IVIM parameters have demonstrated a greater sensitivity to pathology than the ADC model. IVIM-D* was shown to significantly decrease for mild and severe cases of renal dysfunction in the kidneys- the ADC only decreased significantly in severe renal dysfunction (107). For the characterisation of liver lesions, IVIM-D and IVIM-f provided more discriminatory power than ADC (108).

The IVIM parameter values for different organs differ significantly depending on the perfusion of the tissue (Table 2.1).

Table 2.1: Typical IVIM parameters for Volunteers

Study	Organ	IVIM-D ($\times 10^{-3}$ mm^2/s)	IVIM-f	IVIM-D* ($\times 10^{-3}$ mm^2/s)	Number of Volunteers	b-value sequence (s/mm^2)
A. Luciani et al. (109)	Liver	1.10 ± 0.5	0.30 ± 0.05	80 ± 20	25	**10** [0, 10, 20, 30, 40, 50, 100, 200, 400, 800]
Y. Deng et al.(110)	Kidney	1.85 ± 0.13	0.24 ± 0.04	14.53 ± 6.50	12	**9** [0, 50, 100, 150, 200, 300, 400, 600, 800]
W. C. Wu et al.(111)	Brain: White Matter	0.77 ± 0.04	0.07 ± 0.01	7.9 ± 0.9	18	**12** [0, 15, 30, 45, 60, 100, 250, 400, 550. 700, 850, 1000]
	Brain: Grey Matter	0.84 ± 0.05	0.14 ± 0.02	8.2 ± 0.9		

In high perfused tissues, such as the liver and kidneys, the volume fraction is high ~30%. The IVIM-D* parameter is considerably large, with the IVIM-D*/IVIM-D ratio reported as 70 in the liver (45). In low perfused tissue, such as the brain, the perfusion effects are more subtle with the IVIM-D*/IVIM-D ratio of 10 (45) and the volume fraction less than 10% (112).

2.3.3 Challenges of IVIM

2.3.3.1 Selection of b-values

For the effects of perfusion to be measured from the diffusion signal, additional b-values are required, with a particular emphasis on sampling the signal between 0s/mm^2 and 200s/mm^2. There is, however, no consensus on the number of b-values that should be used in the diffusion sequence, nor their distribution. Studies have reported the use of between 5 and 16 b-values for IVIM measurements in the abdomen (109,113,114). Typically, between 6 and 8 b-values are used in the abdomen, with at least four b-values between 0s/mm^2 and 100s/mm^2 (102).

Studies have attempted to optimise the b-value sequence for different tissues (104), i.e. liver (115,116), kidney (45,117), prostate (118), breast (119). The optimisation is relative to the fitting of the ADC and is focused on attaining the optimal statistical fit for the IVIM method. This optimisation relies heavily on the assumption that the behaviour of biological tissue is best explained by the IVIM model.

In low perfused tissues such as the brain, the perfusion compartment is subtle and more b-values are required, with even more sampling the signal at b-value<200s/mm^2 (Table 2.2).

Table 2.2: b-value sequences used for IVIM measurements in the brain

Study	b-value sequence (s/mm^2)
C.Federau et al.(120)	**16**[0, 10, 20, 40, 80, 110, 140, 170, 200, 300, 400, 500, 600, 700, 800, 900]
E. Meeus et al.(121)	**11**[0, 20, 40, 80, 110, 140, 170, 200, 300, 500, 1000]
W. C. Wu et al.(111)	**12** [0, 15, 30, 45. 60, 100, 250, 400, 550, 700, 850, 1000]
S. Zhang et al.(122)	**13**[0, 10, 20, 30, 50, 80, 100, 150, 200, 300, 400, 600, 800]
Y. Yao et al.(123)	**15**[0, 20, 40, 80, 110, 140, 170, 200, 300, 400, 500, 600, 700, 800, 900, 1000]
S. Bidas et al.(124)	**14**[0, 5, 10, 20, 30, 40, 60, 80, 90, 100, 200, 700, 1000, 1300]

There is no consensus for the number of b-values required for measuring IVIM effects in the brain, typically more than ten b-values are implemented. Most studies assume that the perfusion effects are limited to the low b-values, but these may extend to 600s/mm^2 in the brain with the limit predicted to be tissue and pathologically dependent (104). Different b-value sequences sensitise the signal to different compartment behaviours and can greatly impact the measured IVIM parameters (119). It is paramount that the b-value sequence implemented is optimised. The relationship between the b-value sequence and the effect on the diffusion signal should be fully understood.

2.3.3.2 Fitting Method

The fitting method implemented will impact the estimated parameters (125). The IVIM method can be fitted on a pixel-wise basis with an unconstrained non-linear least-squares fitting algorithm- i.e. the Levenberg-Marquardt algorithm. This unconstrained fitting method is known to be sensitive to noise and can lead to incorrect perfusion measurements (37). Alternatively, the diffusion signal can be fitted using a two-step process. The perfusion effects are assumed to only dominate the low b-value regime. A log-transformation is applied to the diffusion signal and IVIM-D calculated using a linear fitting method with b-values >200 s/mm^2. The Levenberg-Marquardt algorithm is then fitted across the whole diffusion signal to calculate IVIM-f and IVIM-D* (121). Another method implemented for fitting the IVIM equation takes the log transform of the data with b-values >200 s/mm^2 and simultaneously fits IVIM-D and IVIM-f from the gradient and y-intercept, respectively. IVIM-D* is then calculated using the Levenberg-Marquardt algorithm across the whole diffusion signal. This fitting method has been reported to provide more accurate and reproducible IVIM parameters in the brain (121).

The non-linear least-squares fitting algorithms, employed in each of these different fitting methods, requires initial starting values for the IVIM parameters. If the Trust Region Reflective algorithm is implemented, upper and lower boundaries must be specified for parameter fitting (126). These initial starting values can bias the parameters with the estimate reaching a local minimum (127). Hence, it is essential for accurate parameter estimation that appropriate initial starting values are selected- these will be tissue-dependent. This is problematic if the tissue type is unknown- such as in cases diagnosing pathology.

2.3.3.3 Number of Compartments

The IVIM model assumes two compartments. In regions that are cystic or ischemic with no perfusion, IVIM-D* will not be defined. In such cases, IVIM-D* can be incorrectly assigned the same value as IVIM-D (120) and IVIM-f estimated by any value between 0 and 1, evidently increasing parameter variability. However, additional physical processes such as multiple diffusion rates within one physical component, bulk flow in tubules or glandular secretion (128) may also affect the detected signal (102), which would lead to more than two exponential components. If more than two-compartments are present, such as partial volume effects between brain tissue and CSF, the high diffusion coefficient of CSF can be misinterpreted and be incorrectly measured in the IVIM-D* parameter.

2.3.4 Relationship of DWI models to Perfusion Measurements

Perfusion MRI uses techniques sensitive to cerebral haemodynamics to create quantitative parametric maps relating to cerebral blood volume (CBV), cerebral blood flow (CBF), and mean transit time (MTT) (129). The three most commonly implemented techniques for perfusion MRI are Dynamic Susceptibility Contrast (DSC), Dynamic Contrast-Enhancing (DCE) imaging, and Arterial Spin Labelling (ASL) (22).

In DSC, a Gadolinium contrast agent is injected intravenously, and a gradient-echo T2-weighted sequence is rapidly repeated. As the bolus passes through the vascular space, it produces a magnetic field distortion, which depending on the concentration of Gadolinium, leads to a significant decrease in signal intensity (130). The signal intensity for each voxel can be plotted as a function of time.

The Gadolinium concentration is proportional to the changes observed in the rate of relaxation in T2. This, in turn, is proportional to the negative logarithm of the relative signal intensity. Hence, using a logarithm transformation, the signal intensity curve can be transformed to measure the gadolinium concentration as a function of time.

Ideally, the bolus would be rapidly delivered to the tissue of interest. Unfortunately, the bolus is delayed and dispersed as it passes through the circulatory system. The contrast agent input to the tissue of interest is described by the Arterial Input Function (AIF) (131). The AIF can be measured from a major artery or automatically selected with software (132).

The perfusion parameter Cerebral Blood Volume (CBV) can be estimated from the area below the concentration-time curve. CBV can be made a quantitative value by dividing the area below the concentration-time curve with the area under the AIF. The Cerebral Blood Flow (CBF) can be estimated with the mathematical process of deconvolving the concentration-time curve with the AIF. The parameter Mean Transit Time (MTT) can be estimated by the division of CBV with the CBF parameter.

The DSC perfusion parameters estimated are based on several assumptions. Firstly, that blood flow and volume remain constant during the measurement. Secondly, the system has a linear response to inputs, and the output follows the principles of superpositions. Finally, the parameter estimations rely on the assumption that all bolus exits the system. This is an oversimplification as bolus can accumulate in tumours where there is a breakdown of the blood-brain barrier. Several strategies have been proposed to address the issue of contrast leakage, such as preload dosing of the contrast agent and baseline subtraction techniques to account for T1 and T2 effects (133), but there is currently no universally accepted method (134).

In the brain, DSC is the most prevalent of the perfusion measurements with demonstrable clinical value in the characterisation of brain tumour haemodynamics (130). DSC image acquisitions are short, typically 2 minutes. DCE is a similar technique, requiring a Gadolinium contrast agent, but instead investigates the T1 shortening effects of the bolus. DCE scans are typically 5-10 minutes in duration.

There is some concern regarding the Gadolinium bolus (135). Recent studies have found gadolinium deposits accumulating in the brain and other organs after multiple injections of the contrast agent (136). Hence a contrast free method for measuring perfusion is desirable. ASL doesn't require an injectable contrast, instead relying on labelling of the arterial blood as it flows through the neck and into the brain (137). RF pulses are used to label protons in the adjacent slice with a high magnetisation such that they can be identified when they flow into the slice of interest, providing contrast against the stationary tissue. The use of ASL can be confounded by the poor signal to noise ratio of the signal acquired (34). The RF sequence leads to a high Specific Absorption Rate (SAR), which can cause tissue heating, restricting repeated use in some populations, such as children (35). Therefore, other contrast free methods for measuring perfusion are under consideration with diffusion models such as IVIM of particular interest.

The theorised relationships between the perfusion parameters and IVIM parameters are presented in Table 2.3:

Table 2.3: Theoretical Relationship between IVIM parameters and Perfusion parameters

IVIM Parameters	Perfusion Parameters	Theoretical Relationship
$IVIM\ f$	CBV	$IVIM\ f = \lambda_{H_2O}^{-1} \cdot CBV$
$IVIM\ D^*$	MTT	$IVIM\ D^* = \frac{L\langle l \rangle}{6} \cdot MTT^{-1}$
$IVIM\ f \cdot IVIM{-}D^*$	CBF	$IVIM\ f \cdot IVIM\ D^* = \frac{L\langle l \rangle}{6\lambda_{H_2O}} \cdot CBF$

CBV- Cerebral Blood Volume; MTT- Mean Transit Time; CBF- Cerebral Blood Flow; λ_{H2O}- fraction of MRI visible water; L-Length of the microvascular network; l-mean microvessel length

The perfusion parameters are related through the equation:

$$CBF = \frac{CBV}{MTT} \tag{2.13}$$

The parameters from the perfusion MRI techniques have been correlated with the perfusion related IVIM parameters with mixed success (42). H. Kim et al. found a significant positive correlation (0.67) between IVIM-f and CBV in the differentiation of glioblastomas (138). C. Federau et al. found a strong correlation (r=0.75) between DSC-CBV and IVIM-f for ROIs across a range of lesions (120). A correlation was also established between IVIM-f×IVIM-D* and DSC-CBF (r=0.65) but a weak relationship between IVIM-D* and DSC-MTT (r=-0.27) was attained. Other studies have also struggled to validate the theorised relationship between IVIM-D* and mean transit time (MTT) (139). S. Bisdas et al. found no clear link between the perfusion related IVIM parameters and the DSC- and DCE- derived metrics in gliomas (140). This poor relationship could be due to the different theoretical background and modelling of the tumour vasculature in the IVIM theory (140), or due to the fitting method implemented for estimating IVIM-f and IVIM-D* (141). The correlation between the perfusion parameters and the diffusion signal require further investigation to determine the feasibility of DWI parameters being used as a surrogate for perfusion measurements.

2.3.5 Multicompartment Modelling

One of the setbacks of the IVIM model is the assumption of two compartments. This has led to investigations into three-compartment models and the fitting of tri-exponential equations:

$$\frac{S(b)}{S(0)} = Ae^{-b\alpha} + Be^{-b\beta} + Ce^{-c\gamma} \tag{2.14}$$

Studies have shown that at high b-values, diffusion can be differentiated into fast (free diffusion) and slow (restricted diffusion) compartments (142,143). Triexponential studies have been performed in liver cirrhosis (144), prostate cancer (145), the characterisation of brain tissue (146)(147), and glioma grading (148). In each case, a triexponential fit was found to be the optimum statistical fit in comparison to the bi-exponential or mono-exponential fit. This suggests that more detailed tissue diffusion can be attained with the additional parameters.

Similar challenges that confound IVIM are further exacerbated by the tri-exponential fitting method. Different b-value sequences and fitting methods are implemented in each of these studies. The simultaneous fitting of additional coefficients may result in parameter overfitting (149). At high b-values, the assumption of molecular diffusion following a Gaussian distribution breaks down. For b-values > 1000s/mm^2, deviation from Gaussian behaviour is quantified by kurtosis, a dimensionless statistical metric (150). None of the tri-exponential models mentioned considering fast and slow diffusion account for kurtosis, despite sampling high b-values. The biophysical basis for the two diffusion compartments has been linked to extra- and intracellular compartments (147). This is contested by several studies where bi-exponential behaviour was observed to govern diffusion within a single cellular compartment (151)(152). The physiological basis for two diffusion compartments is not yet fully understood.

Tri-exponential diffusion signals with two perfusion and one diffusion compartment have also been considered with success in differentiating kidney lesions (153) and monitoring kidney function (154) and characterising liver tissue (155)(156). Two-compartment perfusion models have largely focused on high perfused tissues, where the rationale for fast and slow perfusion comes from two different flow regimes (154) from capillaries and medium-sized vessels. However, the fast perfusion compartment decays rapidly and can be difficult to measure (35), requiring a very short TR.

2.3.6 Other Diffusion Models

Other equations have been suggested for modelling the diffusion signal. Within one voxel there are a multitude of cells and different components, each with different spin packets, and different diffusivities, contributing to the overall detected signal. The stretched exponential model (SEM) (157) argues that the number of contributing components cannot be known and should instead be represented by a distribution function. The SEM equation:

$$\frac{S(b)}{S(0)} = exp^{-(b \cdot DDC)^{\alpha}} \tag{2.15}$$

Where DDC is the distributed diffusion coefficient, the mean diffusivity for the voxel, and α is the heterogeneity index, a dimensionless parameter ranging from 0 to 1. If only one compartment contributes to the signal, α would be 1, and the SEM model would be mathematically equivalent to the ADC model. The lower the value of α, the greater the heterogeneity. However, the physiological basis for α is uncertain, and therefore α is not yet considered a true biomarker (102). The SEM also doesn't take perfusion effects into consideration.

The Diffusion Kurtosis Model (DKI) (158) accounts for non-Gaussian behaviour at high b-values, a challenge for tri-exponential models previously discussed, and is presented as:

$$\frac{S(b)}{S(0)} = exp^{-b \cdot D + b^2 D^2 K/6} \tag{2.16}$$

Where D is the apparent diffusion coefficient, and K is the apparent diffusional kurtosis. The DKI model doesn't take perfusion effects into consideration; however, DKI has been incorporated into a hybrid DKI-IVIM model (159)(160). DKI is sensitive to noise due to the strong diffusion weightings at high b-values and modelling of the signal with low SNR can be challenging (161). In this project, only b-values ≤1000s/mm^2 were measured, and the DKI model was not considered any further.

2.4 Multi-exponential fitting methods

Fitting of multi-exponential equations to experimental data is a notable problem for many different scientific fields. The number of exponential terms within a signal, the decay coefficients of each term along with the fractional value of each term, indicating each component's contribution to the overall signal, all have to be determined (162). The accuracy of such models is of particular importance in the biomedical field, where multi-exponential decay is common and robust biomarkers are required. The complex fitting problem is further exacerbated by the poor signal to noise ratios (SNRs) and a limited number of data points (163).

Diffusion studies considering a range of multi-exponential models will typically use iterative, non-linear least-squares fitting techniques such as the Levenberg-Marquardt or the Trust-Region Reflective algorithm (127) to fit each of the models considered. The optimum model will then be decided by which equation provided the best statistical fit. However, a whole range of different methods exist for determining the number of exponential components present in a signal. Most of these have been developed to describe time series data and we use that language in this section.

2.4.1 Graphical Methods

Graphical methods attempt to determine the number of exponential components through visual inspection. A logarithm is performed and a straight line drawn through the data. The cut-off point at which the data begins to deviate from the straight line determines the location of the second compartment. Data contributing to the first compartment is removed and the process repeated until all compartments are identified. This problem was initially solved by hand (164), but advances in software eventually lead to the development of computational tools (165). Although simple to execute, graphical methods are subjective and prone to high errors (166). The results are not very accurate, depending on the user-defined cut-off values and the method fails when more than two components are present (167).

2.4.2 Iterative Methods

Iterative methods start with a user-defined initial guess. The algorithm then iterates, improving the approximate solution at each step. The algorithm stops once a user-defined level of convergence or the maximum number of iterations is attained. Iterative methods require good initial starting guesses to ensure that convergence reaches a global minimum- this does require some prior knowledge about the system. If a good initial starting value is not provided, the algorithm has to go through many iterations making the method computationally expensive. Noisy data can exacerbate the time taken for the algorithm to convergence and can result in convergence at a local minimum.

2.4.3 Algebraic Methods

Exponential models can be fitted to data using algebraic methods, where simultaneous linear equations are solved. A popular method for solving exponential summations is the Prony method (168). The signal is regarded as a solution of a homogeneous linear difference equation (LDE) with constant coefficients (169). The solution to the LDE will be a summation of complex exponentials. Therefore, by solving the LDE, the coefficients of the exponential summation can be attained. The Prony method is restricted to data equally spaced in time (163). Also, the Prony algorithms have been demonstrated to be highly susceptible to noise and perform poorly when trying to determine the number of exponential terms in signals with a large number of components (162,163). Many modifications to the Prony method have been developed (169)(170)(171), but the algorithm still struggles with poor SNR and sparse data.

2.4.4 Transform Methods

Transform methods have also been developed (162), in which the data is Fourier transformed to create a spectral plot with spikes representing exponential components (163). A popular technique, known as the Gardner method, uses a Laplace transformation- a continuous integral. However, this approach exacerbates high-frequency noise in the deconvolution process (172), causing ripples and broadening of the spectral peaks, making interpretations of the results difficult.

2.4.5 Model Selection

Selecting the optimum number of exponential terms to model a data series is a challenging task. Complex models can minimise the error but result in overfitting the data. To avoid the risk of overfitting, the Akaike Information Criterion (AIC) (173), is commonly implemented as a means of model selection. The AIC estimates the relative quality of each of the multiparametric fitting methods, rewarding for goodness of fit and penalising for the complexing (Equations 2.15)

$$AIC = n \cdot \ln\left(\frac{RSS}{n}\right) + 2k \tag{2.17}$$

Where RSS is the residual sum of squares, n is the number of data points in the sequel, and k is the number of parameters in the model. The model with the lowest AIC value is considered to be the optimum fit.

2.5 The Auto-Regressive Moving Average Model

2.5.1 The ARMA model

The Auto-Regressive Moving Average (ARMA) model has been evaluated for the fitting of multi-exponential data (174). ARMA models were considered due to their ability to fit a broad range of data types without making any previous assumptions about the data. The ARMA model is established through a series of equations which can be classified into two subsets- the Auto-Regressive (AR) part and the Moving Average (MA) part. The AR model is a time series in which the current value of a system is dependent upon a linear function of previous values. AR(P), an AR model of order P is described by:

$$y(t) = \sum_{j=1}^{P} \alpha_j y(t-j) \tag{2.18}$$

Where the order P specifies how many lagged terms there are, y(t) is the signal at time point t, y(t-j) are the lagged signal values at point t-j with lag j, and α_j are the multiplication coefficients.

The MA model in a time series has terms dependent upon past errors, or input values. MA (Q), a MA model of order Q and dependent upon Q lagged terms, is specified by:

$$y(t) = \sum_{i=0}^{Q} \beta_i x(t-i) \tag{2.19}$$

where $x(t-i)$ are the lagged input values at time $(t-i)$ with lag i, and β_i are the multiplication coefficients. Hence an ARMA model is a linear combination of these two models, with ARMA (P, Q) giving:

$$y(t) = \underbrace{\sum_{i=0}^{Q} \beta_i x(t-i)}_{Moving\ Average} + \underbrace{\sum_{j=1}^{P} \alpha_j y(t-j)}_{Auto-Regressive} \tag{2.20}$$

The α_j and β_i coefficients are determined such that the error between the data and the model are minimised. Upon selecting the order of the ARMA model, the coefficients are determined via establishing the following matrices (175):

$$Y = \begin{bmatrix} x_{(0)} & 0 & \cdots & 0 & 0 & 0 & \cdots & 0 \\ x_{(1)} & x_{(0)} & \cdots & \vdots & y_{(0)} & 0 & \cdots & \vdots \\ \vdots & \vdots & \cdots & \vdots & y_{(1)} & y_{(0)} & \cdots & \vdots \\ \vdots & \vdots & \cdots & \vdots & \vdots & \vdots & \cdots & \vdots \\ x_{(t)} & x_{(t-1)} & \cdots & x_{(t-Q)} & y_{(t-1)} & y_{(t-2)} & \cdots & y_{(t-P)} \end{bmatrix}; A = \begin{bmatrix} \beta_0 \\ \vdots \\ \beta_Q \\ \alpha_1 \\ \vdots \\ \alpha_P \end{bmatrix}; \ Y_{Pred} = \begin{bmatrix} y_{(0)} \\ y_{(1)} \\ \vdots \\ y_{(t)} \end{bmatrix} \ \#(2.21)$$

Y is a matrix engineered from the previous input and output terms. A is the matrix of ARMA coefficients, and Y_{pred} is the final model of the predicted signal. By solving the normal equation such that:

$$Y \cdot A = Y_{Pred} \tag{2.22}$$

the ARMA coefficients are minimised and the model Y_{pred} established.

2.5.2 Interpretation of the ARMA model

The ARMA model is a popular forecasting tool used to study economics and financial time series (176)(177). In these applications, the crucial focus is to implement the ARMA model to enable the prediction of future time points- the interpretation behind the optimum ARMA order or corresponding coefficients is not of interest

In general, the ARMA models are considered atheoretical (178). However, it is theorised that more complex data will require modelling with a higher-order ARMA model (179). For exponential fitting, it is postulated that the optimum ARMA order will be dependent on the number of exponential components present in the signal. A MA(1) process can be modelled as an infinite AR process, AR(∞) (180).To ensure each component is fully independent of one another, only ARMA(P,Q) orders with $P \geq Q$ will be considered. To avoid overfitting, the maximum order considered is limited to ARMA(3,3) with up to 99% of datasets modelled by no more than a third-order lag term (181).

The interpretation of the minimisation coefficients is challenging. For AR(1) models, the lower the value of α_1, the quicker the rate of convergence. AR(1) structure imposes an exponential decay rate (182) and α_1 inversely correlates with the decay rate. For MA(1) models, the convergence to the mean is linear (183). Higher-order ARMA models can model increasingly complex behaviour. For the application of ARMA to exponential decays, the signal is not stochastic and will follow trends similar to that of AR(1). The α and β ARMA minimisation coefficients will, therefore, relate to the magnitude of decay. The modelling of the diffusion signal with the ARMA model will be explored in the next chapter.

2.5.3 Applications of the ARMA model to MR

The ARMA model has been implemented for time series analysis across a range of MR data. ARMA models have been used to model the error caused in the reconstruction of MR images after a Fast Fourier Transform (184). ARMA models have been implemented for the calculations of T2 and chemical shift in cases with a limited number of sparsely sampled echoes (185)(186). ARMA models have also effectively fitted contrast perfusion signals in cardiac MRI (187)(188)(189).

In each of these studies, ARMA was applied to MR time series data and used as an atheoretical model. In the subsequent chapters, the ARMA model is modified for the interpretation of the diffusion signal. The optimum ARMA order and the corresponding α and β coefficients are investigated and related to multi-component behaviour, as well as tissue diffusion and perfusion behaviour.

Chapter 3

The ADAPT Method for Model Selection

3. The ADAPT Method for Model Selection

In this chapter, the ARMA model is introduced as the ADAPT model, modified for DWI signals. A full mathematical formalism is provided and discussed. The methodology for using ADAPT to determine the number of components in the diffusion signal is presented. A partial volume effects model, combining white matter and cerebrospinal fluid signals is investigated and the results compared to those of multi-exponential fitting methods. Once optimised, ADAPT is fitted to In-Vivo data.

3.1 Introduction

Multi-exponential fitting is a challenging task for diffusion-weighted magnetic resonance imaging (DW-MRI) data, where there are a limited number of data points, and the number of components within the diffusion signal is unknown. Theoretical and experimental studies have suggested that water diffusion in biological tissue is characterised by multi-exponential behaviour (35,145,147). Diffusion-weighted imaging (DWI) has been demonstrated to have clinical relevance for identifying areas of cerebral ischemia and oncological diagnosis (190). As the reported diffusion coefficient is dependent upon the fitting method implemented, it is crucial that the optimum method is realised.

In order to attain the diffusion coefficient for each voxel in the MR image, the scan is repeated at different b-values (84). The b-value is related to the duration, strength and time-spacing of these two gradient pulses. As the b-values increase, so does the sensitivity to particle motion, and the detected signal attenuates exponentially. By plotting the signal on a logarithmic scale and calculating the gradient, the diffusion coefficient for that voxel is attained (91) — the greater the signal attenuation, the greater the rate of diffusion.

Multi-component models have been applied to DWI data previously, and the most common is the Intravoxel Incoherent Motion (IVIM) method (90). The IVIM method assumes that the signal is composed of two exponentials, accounting for tissue water diffusion and bulk flow in small blood vessels. When plotted on a logarithmic scale, the gradient of each component provides the diffusion related coefficients for each exponential term. If IVIM is fitted using the Levenberg-Marquardt algorithm, initial starting values for the parameters are required, and the fitting stability is often improved by using a multistep fitting approach (191). However, the assumption that only two components exist might not be appropriate in some cases. Additional physical processes (192) and cases where a voxel contains partial volumes (i.e. a mixture of brain tissue and fluid) may lead to more than two exponential components. Hence, a method that can optimise the number of components could provide new insight into the physical properties of water motion in tissue.

Several variables have to be defined for multi-exponential fitting. The number of exponential terms, the magnitude and the fractional contributions to the signal all have to be determined (162). Common exponential fitting methods such as graphical methods are simple to execute but are subjective and prone to high errors (166). Parametric techniques, such as the Prony method which provide a solution as a series of damped sinusoids (168), are also commonly implemented but are highly sensitive to noise. Transform methods have also been developed (162), in which the data is Fourier transformed to create a spectral plot with spikes representing exponential components (163). However, this approach exacerbates high-frequency noise in the deconvolution process (172), and interpretations of the results can be difficult. Overall, there is a need to develop improved analysis methods for multi-exponential data.

Auto-Regressive Moving Average (ARMA) models (174) are generalised versions of multi-exponential models and can predict the behaviour of a data series from previous values alone.

ARMA has the flexibility to represent a wide range of data series, with the order (number of lag terms) of the optimum ARMA model relating to the complexity of the data. However, such a method is restricted to the time domain. Therefore, this chapter aimed to develop a new generalised fitting method for multi-exponential data where the number of components is unknown a priori and evaluate it on simulated and real multi b-value DWI data.

3.2 Materials and Methods

3.2.1 The Auto-regressive Discrete Acquisition Points Transformation (ADAPT) Method

To adapt the ARMA equation for the modelling of DWI data, the method was modified henceforth referred to as the Auto-regressive Discrete Acquisition Points Transformation (ADAPT) method. ADAPT models the diffusion signal by the equation:

$$\ln(S_n) = \sum_{i=0}^{Q} \beta_i b_{n-i} + \sum_{j=1}^{P} \alpha_j \ln\left(S_{n-j}\right) \tag{3.1}$$

Where S_n-Signal at acquisition point n; b_n- b-value at acquisition time point n. αj, βi-minimisation coefficients. Here the acquisition point of the b-values is used such that b value=0 s/mm^2 at acquisition point 0, b(0)=0. b-value=20 s/mm^2 at acquisition point 1, b(1)=20 and so forth. The previously acquired b-values are therefore used as previous input terms. Upon selecting the order of the ADAPT(P,Q) model, the α and β minimisation coefficients are determined such that the error between the data and the model is minimised. The coefficients are determined via establishing the matrices in (Equation 3.2):

$$S = \begin{bmatrix} b_{(0)} & 0 & \cdots & 0 & 0 & 0 & \cdots & 0 \\ b_{(1)} & b_{(0)} & \cdots & \vdots & \ln\left(\frac{S_{(0)}}{S_{(0)}}\right) & 0 & \cdots & \vdots \\ \vdots & \vdots & \cdots & \vdots & \ln\left(\frac{S_{(1)}}{S_{(0)}}\right) & \ln\left(\frac{S_{(0)}}{S_{(0)}}\right) & \cdots & \vdots \\ \vdots & \vdots & \cdots & \vdots & \vdots & \vdots & \cdots & \vdots \\ b_{(N)} & b_{(N-1)} & \cdots & b_{(N-Q)} & \ln\left(\frac{S_{(N-1)}}{S_{(0)}}\right) & \ln\left(\frac{S_{(N-2)}}{S_{(0)}}\right) & \cdots & \ln\left(\frac{S_{(N-P)}}{S_{(0)}}\right) \end{bmatrix};$$

$$A = \begin{bmatrix} \beta_0 \\ \vdots \\ \beta_Q \\ \alpha_1 \\ \vdots \\ \alpha_P \end{bmatrix}; \qquad S_{pred} = \begin{bmatrix} \ln\left(\frac{S_{(0)}}{S_{(0)}}\right) \\ \ln\left(\frac{S_{(1)}}{S_{(0)}}\right) \\ \vdots \\ \ln\left(\frac{S_{(N)}}{S_{(0)}}\right) \end{bmatrix} \tag{3.2}$$

S is a matrix engineered from the input b-values and the detected signal with acquisition point n=0, …, N. A is the matrix of ADAPT coefficients. S_{pred} is the final model of the predicted signal normalised by S(0)- the initial signal value at b=0 and n=0. By solving the normal equation such that:

$$\mathrm{S} \cdot \mathrm{A} = \mathrm{S}_{\mathrm{pred}} \tag{3.3}$$

the ADAPT coefficients are minimised and the model S_{pred} is established.

3.2.1.1 Determining the Number of Components

Upon selection of the optimum ADAPT order, the transfer function can be expressed as:

$$\mathrm{H(n)} = \frac{\ln(\mathrm{S_n})}{\mathrm{b_n}} = \frac{\beta_0 + \beta_1\hat{\mathrm{L}} + \cdots + \beta_{\mathrm{P}}\hat{\mathrm{L}}^{\mathrm{P}}}{1 - \alpha_1\hat{\mathrm{L}} - \cdots - \alpha_{\mathrm{Q}}\hat{\mathrm{L}}^{\mathrm{Q}}} \tag{3.4}$$

Where $\hat{\mathrm{L}}$ is the lag operator (181) such that $\ln(\mathrm{S_n})\,\hat{\mathrm{L}} = \ln(\mathrm{S_{n-1}})$. By mapping the transfer function of the optimum order to the Z-domain, the following is obtained:

$$\mathrm{H(z)} = \frac{\beta_0 + \beta_1 z^{-1} + \cdots + \beta_P z^{-P}}{1 - \alpha_1 z^{-1} - \cdots - \alpha_Q z^{-Q}} \tag{3.5}$$

Equation 3.5 can be rearranged using partial fraction decomposition. An inverse Z-transform was then performed, and the number of components established.

3.2.1.2 ADAPT(1,1)

For example, ADAPT(1,1) gives:

$$\ln(S_n) = \beta_0 b_n + \beta_1 b_{n-1} + \alpha_1 \ln(S_{n-1}) \tag{3.6}$$

Taking the transfer function of ADAPT(1,1):

$$H(n) = \frac{\ln(S_n)}{b_n} = \frac{\beta_0 + \beta_1 \hat{L}}{1 - \alpha_1 \hat{L}} \tag{3.7}$$

Converting to the Z-domain:

$$H(z) = \frac{\beta_0 + \beta_1 z^{-1}}{1 - \alpha_1 z^{-1}} \tag{3.8}$$

Performing partial fraction decomposition (PFD):

$$H(z) = \frac{\beta_1}{\alpha_1 - z} + \frac{\beta_0 \alpha_1}{\alpha_1 - z} - \beta_0 \tag{3.9}$$

And finally, performing the inverse Z transform:

$$\mathrm{H(n)} = \beta_1 {\alpha_1}^{n-1} + \beta_0 {\alpha_1}^{n} \tag{3.10}$$

Here ADAPT(1,1) is evaluated to be a two-component decay model.

3.2.1.3 ADAPT(1,0)

ADAPT(1,0) gives:

$$\ln(S_n) = \beta_0 b_n + \alpha_1 \ln(S_{n-1}) \tag{3.11}$$

And the transfer function of ADAPT(1,0) in the Z-domain:

$$H(z) = \frac{\beta_0 z}{z - \alpha_1} \tag{3.12}$$

Performing partial fraction decomposition (PFD) and an inverse Z transform:

$$H(n) = \beta_0 {\alpha_1}^n \tag{3.13}$$

Hence ADAPT(1,0) was also evaluated to be a one-component decay model.

3.2.1.4 ADAPT(2,0)

ADAPT(2,0) gives:

$$\ln(S_n) = \beta_0 b_n + \alpha_1 \ln(S_{n-1}) + \alpha_2 \ln(S_{n-2}) \tag{3.14}$$

And the transfer function of ADAPT(2,0) in the Z-domain:

$$H(z) = \frac{\beta_0 z^2}{z^2 - \alpha_1 - \alpha_2} = \frac{\beta_0 z^2}{(z - r_1)(z - r_2)} \tag{3.15}$$

Where the denominator is factorised such that r_1 and r_2 are roots of the quadratic expression. Performing PFD and an inverse Z transform:

$$H(n) = A{r_1}^{n-1} + B{r_2}^{n-1} \tag{3.16}$$

Where A and B represent the numerators that would be attained through the PFD. Hence ADAPT(2,0) was also evaluated to be a two-component decay model.

3.2.1.5 ADAPT(2,1)

ADAPT(2,1) gives:

$$\ln(S_n) = \beta_0 b_n + \beta_1 b_{n-1} + \alpha_1 \ln(S_{n-1}) + \alpha_2 \ln(S_{n-2}) \tag{3.17}$$

And the transfer function of ADAPT(2,1) in the Z-domain:

$$H(z) = \frac{\beta_0 z^2 + \beta_1 z}{z^2 - \alpha_1 - \alpha_2} \tag{3.18}$$

Performing PFD and an inverse Z transform:

$$H(n) = C{r_1}^{n-1} + D{r_2}^{n-1} \tag{3.19}$$

Where r_1 and r_2 are roots of the quadratic expression in the denominator of the transfer function and C and D, represent the numerators that would be attained through the PFD. Hence ADAPT(2,1) was also evaluated to be a two-component decay model.

3.2.1.6 ADAPT(3,1)

ADAPT(3,1) gives:

$$Ln(S_n) = \beta_0 b_n + \beta_1 b_{n-1} + \alpha_1 \ln(S_{n-1}) + \alpha_2 \ln(S_{n-2}) + \alpha_3 \ln(S_{n-3}) \tag{3.20}$$

And the transfer function of ADAPT(3,1) in the Z-domain:

$$H(z) = \frac{\beta_0 z^2 + \beta_1 z}{z^3 - \alpha_1 z^2 - \alpha_2 z - \alpha_3} = \frac{\beta_0 z^2 + \beta_1 z}{(z - r_1)(z - r_2)(z - r_3)} \tag{3.21}$$

Where the denominator is factorised such that r_1, r_2 and r_3 are roots of the cubic expression. Performing PFD and an inverse Z transform:

$$H(n) = F{r_1}^{n-1} + G{r_2}^{n-1} + H{r_3}^{n-1} \tag{3.22}$$

Where F, G and H represent the numerators that would be attained through the PFD. Hence ADAPT(3,1) was evaluated to be a three-component decay model.

3.2.2 Data Simulations

All simulated and acquired In-Vivo data was created or obtained using a range of 11 exponentially spaced b-values between 0 and 1000 [0, 20, 40, 80, 110, 140, 170, 200, 300, 500, 1000] s/mm^2. All simulations and data analysis were conducted using MATLAB (MathWorks, Natick, MA, USA, v.2016b).

3.2.2.1 Simulation of a Bi-exponential Signal

A range of bi-exponential diffusion signals were created by simulating data using the equation for the IVIM method:

$$\frac{S(b)}{S(0)} = f \cdot \exp^{-bD^{*}} + (1 - f) \cdot \exp^{-bD} \qquad (3.23)$$

Where S(b)/S(0) is the signal intensity for a particular b-value, b, normalized by the signal intensity when b=0 s/mm^2; D is the tissue diffusion coefficient; D* is the pseudo-diffusion coefficient (related to the perfusion of blood in the capillary network); and f is the volume fraction of incoherently flowing blood in the tissue describing the fraction of the signal arising from the vascular network (91).

Bi-exponential signals were created with a range of f values (0.1, 0.3 and 0.5) and three different D*/D ratios corresponding to those observed in the brain, kidney and liver (10, 20 and 70 respectively) (45). The D parameter was fixed at 0.0007 mm^2/s and the D* parameters considered were 0.007 mm^2/s, 0.014 mm^2/s and 0.049 mm^2/s. Random white Gaussian noise was added to the simulated signals to mimic SNR levels of 50, typical of those measured In-Vivo data. The ADAPT method was applied to the bi-exponential signals, and a range of orders from ADAPT(0,0) to ADAPT(3,3) were considered.

3.2.2.2 Simulation of a Multi-Component Partial Volume Effects Model

A partial volume effects (PVE) model was simulated, in which compartments from both cerebral white matter (WM), assumed to be a two-compartment model, and cerebrospinal fluid (CSF), assumed to be one compartment, are simultaneously detected, thus creating a tri-exponential model.

$$\frac{S(b)}{S(0)} = Ae^{-b\alpha} + Be^{-b\beta} + Ce^{-b\gamma} \tag{3.24}$$

Such a tissue model is of particular interest to DWI, as the use of the IVIM method in the brain requires cautious interpretation in regions of tissue edges due to PVE. The high value of the diffusion coefficient in CSF and the much lower diffusion coefficient in WM results in the incorrect detection of a large perfusion value within the cerebral cortex, when a voxel contains information from both these regions (42). CSF was assumed to exhibit mono-exponential behaviour with a diffusion coefficient assumed to be that of free water at $37°C$ ($D_{CSF} = 3 \times 10^{-3} mm^2/s$) (80). WM was assumed to be represented by the bi-exponential IVIM method. The WM model parameters were taken from averaged IVIM values previously reported in a volunteer study ($f_{WM} = 0.07; D_{WM} = 0.77 \times 10^{-3} mm^2/s$; $D^*{}_{WM} = 7.9 \times 10^{-3} mm^2/s$)(111). A partial volume effect (PVE) model was created as a summation of the CSF and WM model such that Equation(3.24) was parameterised with physically meaningful coefficients:

$$\frac{S(b)}{S(0)} = f_{CSF}e^{-bD_{CSF}} + (1 - f_{CSF})\left(f_{WM}e^{-bD^*{}_{WM}} + (1 - f_{WM})e^{-bD_{WM}}\right) \tag{3.25}$$

Where f_{CSF} indicated the fraction of the signal that was contributed by the CSF compartment. A range of PVE models were created with varying CSF:WM ratios (100:0, 75:25, 50:50, 25:75 and 0:100). White Gaussian noise was added to PVE models to mimic SNR levels ≈ 50.

3.2.2.3 Robustness Analysis

Poor signal quality can result in a change of parameter values or in the detection of an additional component. Hence the effects of poor SNR on the robustness of the fitting methods were investigated. Random white Gaussian noise was added to the simulated signals to mimic SNR levels between 20 and 100. Although the noise present in MRI data is governed by a Rician noise distribution, the distribution is approximately Gaussian for the SNR levels considered in this study (121). Noise was added using the MATLAB Communications System Toolbox ‘Add White Gaussian Noise’ (awgn) function. The data simulations were performed using 1000 random data iterations for each model and SNR level.

3.2.3 Physical Phantom

A physical phantom with multiple compartments containing varying Deuterium Oxide (D_2O)/ H_2O mixtures was designed and scanned to further consider the effects of partial volumes. The phantom was created with two hydrogel compartments: the bottom layer, Agarose gel formed with 10% D_2O/90% H_2O; the top layer, Agarose gel formed with 100% H_2O and N-Acetylaspartic acid (NAA). A balloon filled with water was suspended between the two hydrogels. The phantom was scanned with the same diffusion protocol used for In-Vivo data acquisitions (3.2.4).

3.2.4 In-Vivo Data Acquisition

A volunteer brain scan (age 25 years), SNR≈50 in WM at b-value = 0 s/mm^2, was acquired on a Philips Achieva 3T TX (Philips Healthcare, Best, the Netherlands) MRI scanner at Birmingham Children’s Hospital using a 32-multichannel receiver head coil. A patient (age 3.2 years) with a brain tumour, suprasellar pilomyxoid astrocytoma, was also scanned. The patient case was considered as the ventricles were enlarged due to hydrocephalus, allowing for an easier investigation of the one compartment CSF. It should be noted that no tumour was present on the slice considered. Informed parental consent was obtained for all subjects and the East Midlands – Derby Research Ethics Committee (REC 04/MRE04/41) approved the study operating under the rules of Declaration of Helsinki 1975 (and as revised in 1983). The diffusion-weighted MRI sequence used a sensitivity-encoded (SENSE) approach with the following parameters: b-value data acquired in three orthogonal directions, FOV 230mm x 230mm, TR/TE 3,214/84ms, matrix size 256x256, 5mm slice thickness and in-plane resolution 0.9mm x 0.9mm. The spectral presaturation with inversion recovery (SPIR) was used for fat suppression and the scan duration was 2.21 minutes.

3.2.5 Data Analysis

3.2.5.1 Measuring SNR

In-Vivo SNR levels were calculated using the standard NEMA method based on the difference image from two acquisitions; this is the recommended method for determining SNR when parallel imaging techniques are used (77). The quality of parameter estimation depends strongly on the SNR, with the SNR for the low IVIM perfusion regime recommended to be above a critical value of 40 (45,121). An SNR≈50 was recorded in the White Matter (b-value =0), in agreement with previous studies using this acquisition protocol (191).

3.2.5.2 Model Selection

The Akaike information criterion (AIC) (173) was used as a means of model selection for determining the optimum ADAPT order. The AIC estimates the relative likelihood of a model being the optimum fit by measuring the trade-off between goodness of fit and model complexity. Such a selection process aims to reduce the risk of over-fitting. As the b-value sequence used within the diffusion-weighted imaging (DWI) protocol typically has less than 30 b-values (11 in the cases considered), they can be considered to be a finite data set (35). Thus the corrected AIC (AICc) (193), with a harsher penalty for overfitting, was implemented. The AICc formula (11):

$$\mathrm{AIC_c} = \mathrm{n} \cdot \log\left(\frac{\mathrm{RSS}}{\mathrm{n}}\right) + \frac{2 \cdot \mathrm{k} \cdot (\mathrm{k}+1)}{\mathrm{n}-\mathrm{k}-1} \qquad (3.26)$$

Where n is the number of b-values used to fit the signal; k is the number of parameters; and RSS is the residual sum squared. The fit with the lowest AICc value is considered to be the optimum fit. The number of parameters, k, includes the diffusion signal S_0 (194) and an additional parameter is counted due to the Gaussian noise hypothesis for the signal residuals (35).There is a debate in the literature that the AIC is only suitable for analysing nested models and is consequently inherently biased. Although the models in this study are nested, other studies have shown the AIC as a suitable criterion for a wide range of model types, both nested and non-nested (195). However, to ensure that such a selection criterion is not ad-hoc, an additional selection criterion is also considered- the Bayesian Information Criterion corrected for small samples (BICc) (196).

It is advocated that an approach of using two criteria together can increase the confidence in identifying the optimum order (197). Hence the BICc was also calculated:

$$\mathrm{BICc} = \frac{\mathrm{k \cdot n \cdot \log(n)}}{n-k-1} + \mathrm{n} \cdot \log\left(\frac{\mathrm{RSS}}{\mathrm{n}}\right) \tag{3.27}$$

The relative significance of the optimum information criterion fit was justified with the use of Bayes Factors (198) where w_i is the Weight, indicating the probability of model i being the optimum model and the associated statistic the log evidence ratio (LER) indicates evidence for the parsimoniousness of the optimum model against a competing model. The Akaike weight, w_i:

$$\mathrm{w_i} = \frac{\exp\left(-\frac{1}{2}\Delta_\mathrm{i}\mathrm{AICc}\right)}{\sum_{\mathrm{m=1}}^{\mathrm{M}} \exp\left(-\frac{1}{2}\Delta_\mathrm{m}\mathrm{AICc}\right)} \tag{3.28}$$

Where M is the number of compared models and:

$$\Delta_\mathrm{i}\mathrm{AICc} = \mathrm{AICc(i)} - \mathrm{AICc_{min}} \tag{3.29}$$

Where $\mathrm{AICc_{min}}$ is the minimum AICc value of all the models considered. The Akaike weight of all the models summed together should equal one. The Evidence Ratio ER:

$$\mathrm{ER_i} = \frac{\mathrm{w_{max}}}{\mathrm{w_i}} \tag{3.30}$$

Where $\mathrm{w_{max}}$ is the Akaike weight of the optimum model. The LER is provided by taking the log of the ER such that.

$$\mathrm{LER_i} = \log_{10}(\mathrm{ER_i}) \tag{3.31}$$

LER values greater than 0, 0.5, 1 or 2 indicate respectively that the evidence is 'minimal', 'substantial', 'strong' or 'decisive'.

3.2.5.3 Statistical Analysis

For the data simulations, correlation analysis (Pearson correlation coefficient, r) was performed to determine how the ADAPT(1,1) coefficients were related to the IVIM parameters. ADAPT(1,1) was considered as it was found to be the optimum fit for bi-exponential equations. The IVIM parameters were calculated using the multi-exponential fitting methods as described in the section below (Section 3.2.5.4). The statistical significance of the relationship was assessed using the p-value (P <0.05). The robustness of the ADAPT and multi-exponential coefficients, when fitted to the PVE models, was assessed by calculating the coefficient of variation (CV) over the 1000 iterations measured.

For the In-Vivo data, correlation analysis (Spearman's rank correlation coefficient, s) was performed to compare the ADAPT(1,1) coefficients to the IVIM parameters. ρ values between 0.60 - 0.79, and 0.80 - 1.0 were considered to represent a 'strong' and 'very strong' correlation respectively. Five regions of interest (ROIs), each 4x4 pixels, were selected from within both the one compartment CSF and the two-compartment WM. The ROIs were drawn upon the DWI scans with no additional filtering. The optimum ADAPT and multi-exponential fitting methods were fitted to each of the ROIs. To investigate the robustness of the fitting parameters, the average parameter value and CV was calculated.

3.2.5.4 Multi-exponential Fitting Methods

The bi-exponential fitting method for the IVIM equation was assessed using non-linear least-squares minimisation, with the Levenberg-Marquardt algorithm and a constrained 2-parameter fitting method (121). The tri-exponential fitting method used the same minimisation technique and a constrained 4-parameter fitting method. The mono-exponential fitting method was also considered for the PVE models and In-Vivo data. By plotting the signal on a logarithmic scale and calculating the gradient, the Apparent Diffusion Coefficient (ADC) is attained.

3.2.5.5 Performance of Fitting Methods

All calculations were performed on OS: Windows 10 Pro 64-bit (10.0 Build 16299), CPU: AMD Ryzen 5 1600, 3.2 GHz, Memory: 8192 MB DDR4 RAM. To compare the performance of the ADAPT and IVIM fitting methods, the CPU run time of each method was recorded and averaged over 10 iterations.

3.3 Results

3.3.1 ADAPT Method Applied to Simulated Bi-exponential Signal

3.3.1.1 Selection of Optimum Fit

A range of ADAPT orders were fitted to the simulated bi-exponential signal (SNR ≈ 50) with varying IVIM parameters (Figure 3.1).

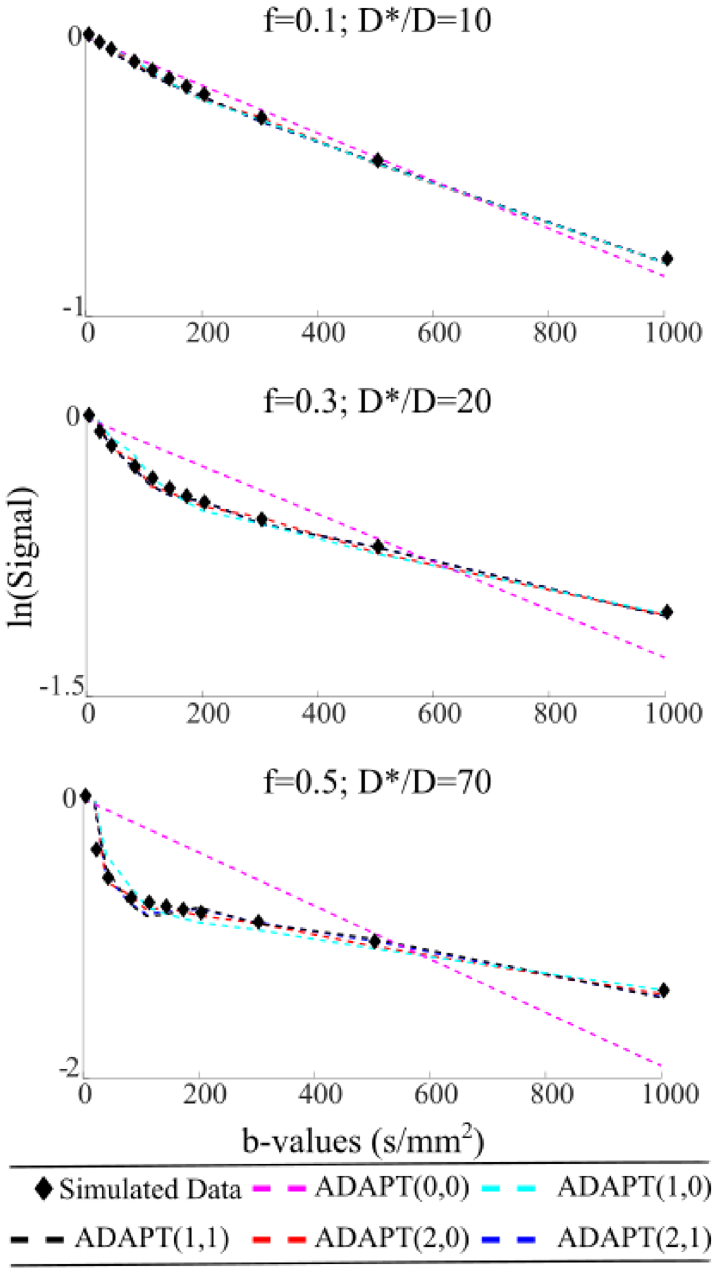

Figure 3.1: The ADAPT orders fitted to a range of simulated bi-exponential signal

For each of the 9 scenarios considered ADAPT(1,1) was found to be the optimum order, having the lowest AICc for every case (Table 3.1).

Table 3.1: ADAPT Orders Fitted to Bi-exponential Diffusion Signals-AICc

			ADAPT Orders				
D*/D	**f**		**(0,0)**	**(1,0)**	**(1,1)**	**(2,0)**	**(2,1)**
10	0.1	AICc	-73	-97	**-120**	-97	-115
		LER_{AIC_c}	10.06	4.85	**0**	4.94	0.92
	0.3	AICc	-49	-79	**-101**	-80	**-98**
		LER_{AIC_c}	11.22	4.74	**0**	4.39	**0.49**
	0.5	AICc	-36	-68	**-91**	-69	**-89**
		LER_{AIC_c}	11.87	5.03	**0**	4.75	**0.42**
20	0.1	AICc	-65	-88	**-106**	-93	-103
		LER_{AIC_c}	8.93	3.88	**0**	2.98	0.67
	0.3	AICc	-39	-68	**-82**	-73	-79
		LER_{AIC_c}	9.35	3.12	**0**	2.02	0.70
	0.5	AICc	-25	-56	**-71**	-61	-68
		LER_{AIC_c}	9.90	3.21	**0**	2.07	0.70
70	0.1	AICc	-59	-78	**-84**	-80	-80
		LER_{AIC_c}	5.39	1.24	**0**	0.75	0.70
	0.3	AICc	-32	**-56**	**-58**	**-57**	-55
		LER_{AIC_c}	5.58	**0.48**	**0**	**0.23**	0.66
	0.5	AICc	-18	**-43**	**-45**	**-44**	-42
		LER_{AIC_c}	5.84	**0.39**	**0**	**0.09**	0.62

A range of two compartment bi-exponential diffusion signals (SNR≈50) were investigated with a range of IVIM-D*/D ratios and IVIM-f values. The ADAPT method was applied to the bi-exponential signals and the optimum fit (highlighted) was selected by choosing the method with the lowest AICc. Those ADAPT orders lightly shaded have an AICc-LER<0.5 indicating competing models.

For the bi-exponential signals where D*/D=10, the competing order ADAPT(2,1) was found to have an AICc-LER just below 0.5 in two instances. For the bi-exponential signals with D*/D=70 and f=0.3 or 0.5, the AICc-LER ratio indicates that ADAPT(1,0) and ADAPT(2,0) are competing orders that should also be taken into consideration. ADAPT orders (2,2), (3,0), (3,1), (3,2) and (3,3) were also considered for each case but possessed comparatively higher

Table 3.2: ADAPT Orders Fitted to Bi-exponential Diffusion Signals-BICc

			ADAPT Orders				
D*/D	**f**		**(0,0)**	**(1,0)**	**(1,1)**	**(2,0)**	**(2,1)**
10	0.1	BICc	-68	-89	**-109**	-86	-101
		LER_{BIC_c}	8.79	4.19	**0**	4.94	1.67
	0.3	BICc	-46	-74	**-93**	-72	-87
		LER_{BIC_c}	10.04	4.13	**0**	4.39	1.15
	0.5	BICc	-34	-63	**-83**	-61	-78
		LER_{BIC_c}	10.70	4.42	**0**	4.75	1.08
20	0.1	BICc	-63	-83	**-99**	-85	-92
		LER_{BIC_c}	7.76	3.28	**0**	2.98	1.33
	0.3	BICc	-37	-63	**-74**	-65	-68
		LER_{BIC_c}	8.18	2.51	**0**	2.02	1.36
	0.5	BICc	-23	-51	**-63**	-53	-57
		LER_{BIC_c}	8.72	2.61	**0**	2.07	1.36
70	0.1	BICc	-56	-73	**-76**	-72	-69
		LER_{BIC_c}	5.39	1.24	**0**	0.75	0.70
	0.3	BICc	-30	**-50**	**-50**	**-49**	-44
		LER_{BIC_c}	4.53	**0**	**0.12**	**0.35**	1.44
	0.5	BICc	-15	**-38**	**-37**	**-36**	-42
		LER_{BIC_c}	4.88	**0**	**0.21**	**0.30**	0.62

The optimum ADAPT order for the simulated bi-exponential diffusion signals was selected using the lowest BICc. Those ADAPT orders lightly shaded have a BICc-LER<0.5 indicating competing models.

AICc values and thus very high AICc-LERs. The BICc confirmed that the optimum order was ADAPT(1,1) (Table 3.2). No competing orders were detected when D*/D=10. For the signals with D*/D=70 and f=0.3 or 0.5, the BICc indicated that ADAPT(1,0) was the optimum order. However, the BICc-LER for ADAPT(1,1) was low and the BICc values almost equivalent.

3.3.1.2 Number of Components

The Transfer function, Z-transform, PFD and subsequent inverse Z-transform were performed on ADAPT(0,0), ADAPT(1,0), ADAPT(1,1), ADAPT(2,0) and ADAPT(2,1). ADAPT(0,0) is equivalent to the mono-exponential model and thus, a one-component decay model. As previously stated, ADAPT(1,1) was evaluated to be a two-component decay model. In all bi-exponential simulations considered, a two-component model was found to be the optimum fit, based upon the AICc. ADAPT(2,0) and ADAPT(2,1), which were found to be competing orders are also two-component decay models. ADAPT(1,0), a one-component decay model, was found to be a competing order for some cases. However, for the D*/D ratio of 70 and f value of 0.3, the AICc-LER of ADAPT(1,0) is 0.48 is close to the cutoff and the wi probability (ADAPT(1,0) wi=0.14) is more than half that of the optimum order (ADAPT(1,1) wi=0.43).). Using the BICc, ADAPT(1,0) was identified as the optimum order (wi=0.44). However, the BICc-LER for ADAPT(1,1) was very low, 0.12 and wi= 0.33. For the D*/D ratio of 70 and f-value of 0.5, the w_i probability of ADAPT(1,0) (ADAPT(1,0) w_i=0.15) is more than half that of the optimum order (ADAPT(1,1) w_i=0.37). ADAPT(1,0) had the lowest BICc and was selected as the optimum order (wi=0.46); however, the BICc-LER for ADAPT(1,1) was low, 0.21 and wi= 0.28, indicating a competing model with a comparable probability.

3.3.2 Tri-exponential Partial Volume Effect Models

3.3.2.1 Selection of Optimum Order

Mono-, bi- and tri- exponential fitting methods (Figure 3.2) were applied to the PVE models (SNR ≈ 50) with varying CSF:WM ratios and the optimum fit selected using the AICc (Table 3.3) and the BICc (Table 3.4).

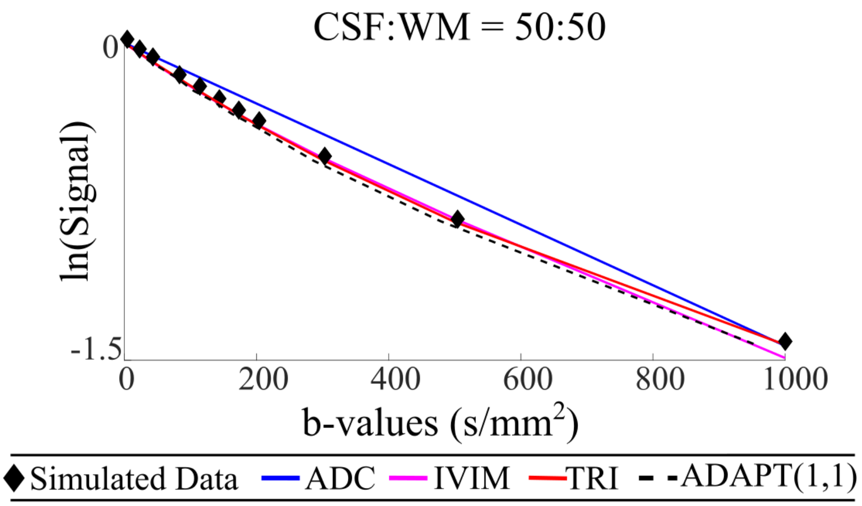

Figure 3.2: The optimum ADAPT order and the multi-exponential models are shown fitted to the PVE model CSF:WM 50:50. The ADAPT model can be used to accurately fit and identify the tri-exponential signal.

Table 3.3: Partial Volume Effects Model fitted with ADAPT orders and Multi-exponential fitting methods-AICc.

			Exponential Model			**ADAPT Orders**					
CSF:WM	Number of compartments		**ADC**	**IVIM**	**TRI**	**(0,0)**	**(1,0)**	**(1,1)**	**(2,0)**	**(3,0)**	**(3,1)**
100:0	1	AICc	-154	**-155**	-154	-154	-160	**-161**	-159	-161	-158
		LER_{AIC_c}	0.32	**0**	0.33	1.45	0.17	**0**	0.32	0.02	0.55
75:25	3	AICc	-67	-110	**-154**	-59	-79	-97	-78	-77	**-108**
		LER_{AIC_c}	18.85	9.40	**0**	10.65	6.13	2.32	6.48	6.75	**0**
50:50	3	AICc	-64	-108	**-152**	-60	-83	-101	-82	-80	**-110**
		LER_{AIC_c}	18.97	9.42	**0**	11.01	5.83	2.02	6.08	6.59	**0**
25:75	3	AICc	-68	-116	**-150**	-67	-92	-111	-91	-88	**-116**
		LER_{AIC_c}	17.77	7.47	**0**	10.75	5.29	1.13	5.40	6.08	**0**
0:100	2	AICc	-80	-140	**-151**	-81	-103	**-128**	-104	-102	-123
		LER_{AIC_c}	15.50	2.44	**0**	10.30	5.35	**0**	5.17	5.71	1.09

A range of PVE models, with varying CSF:WM ratios, were investigated. Multi-exponential fitting methods and the ADAPT method were fitted. The optimum fit was selected by choosing the method with the lowest AICc.

Table 3.4: Partial Volume Effects Model fitted with ADAPT orders and Multi-exponential fitting methods-BICc.

		Exponential Model			**ADAPT Orders**					
CSF:WM		**ADC**	**IVIM**	**TRI**	**(0,0)**	**(1,0)**	**(1,1)**	**(2,0)**	**(3,0)**	**(3,1)**
100:0	BICc	**-149**	-144	-139	**-152**	**-155**	-150	-151	-153	-144
	LER_{BIC_c}	**0**	0.94	2.02	**0.72**	**0**	1.09	0.75	0.45	2.40
75:25	BICc	-62	-100	**-139**	-56	-74	-89	-70	-66	**-93**
	LER_{BIC_c}	16.84	8.64	**0**	8.07	4.12	0.91	5.07	6.00	**0**
50:50	BICc	-59	-97	**-137**	-57	-78	-93	-74	-69	**-96**
	LER_{BIC_c}	16.95	8.66	**0**	8.43	3.81	0.61	4.66	5.84	**0**
25:75	BICc	-63	-105	**-136**	-64	-87	**-103**	-83	-77	**-102**
	LER_{BIC_c}	15.75	6.72	**0**	8.44	3.55	**0**	4.27	5.61	**0.28**
0:100	BICc	-75	-129	**-137**	-78	-98	**-120**	-96	-91	-109
	LER_{BIC_c}	13.48	1.69	**0**	9.13	4.75	**0**	5.17	6.37	2.50

The optimum fitting method for the PVE models (SNR≈ 50) was selected by choosing the method with the lowest BICc.

Based on the AICc, the number of detected components did not correspond to the number of exponential terms presented in the signal. In particular, a tri-exponential fit was found to best represent both two and three-component models. The one-compartment model was best represented by a bi-exponential fit. However, the LER-AICc values indicated that all other multi-exponential fits were competing. Based on the BICc, the one compartment and three-compartment models were correctly identified, but a two-compartment model was overfitted and found to be best represented by a tri-exponential fit. No other multi-exponential fits were found to compete. According to the AICc and BICc, the two-compartment model is wrongly fitted by a tri-exponential equation for even very high SNR≈100 (Figure 3.3).

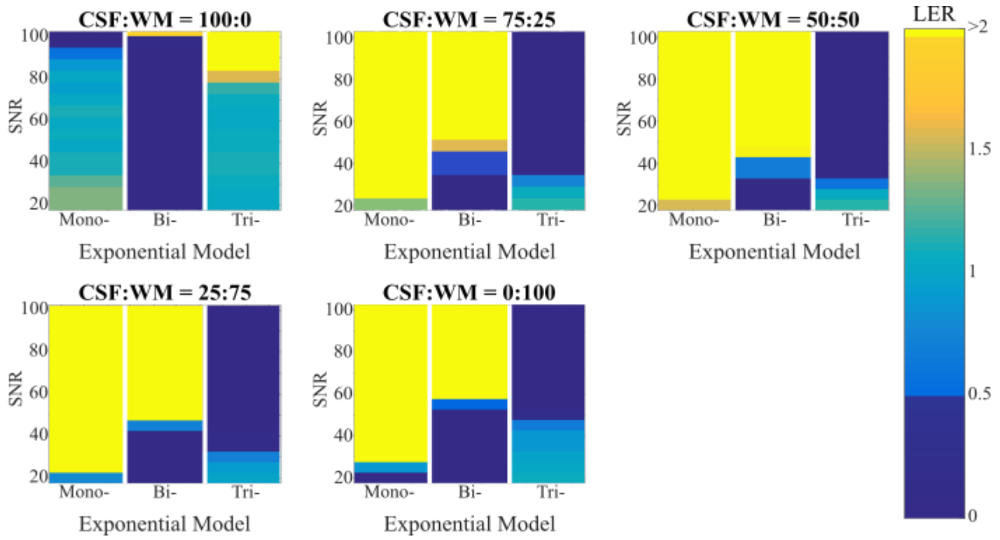

Figure 3.3: Using the AICc-LERs, the number of compartments, identified by the multi-exponential fitting methods was investigated as a function of varying SNR in the PVE models. An AICc-LER<0.5 indicated a competing model that needed to be considered. An AICc-LER>2 indicated a competing model that 'definitely' did not need to be considered.

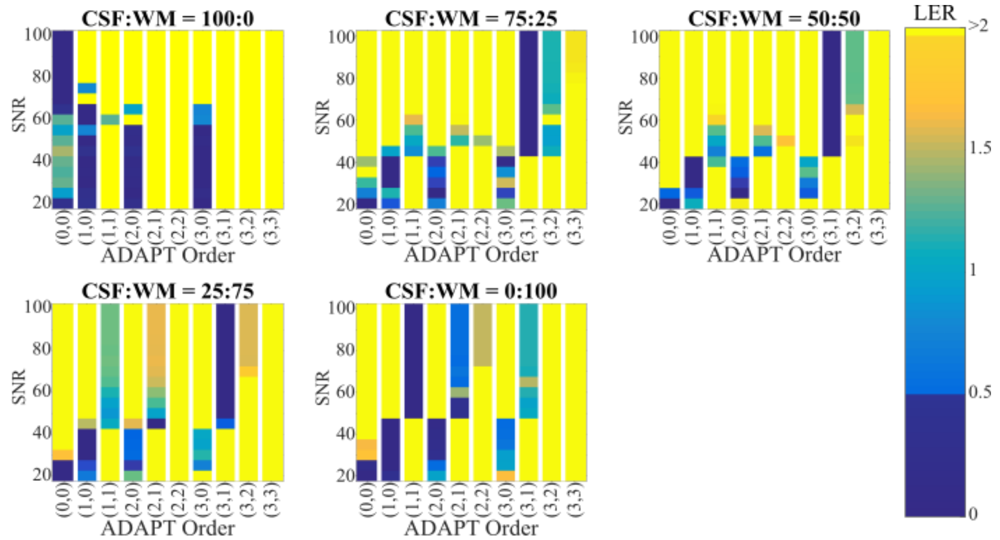

Figure 3.4: Using the AICc-LERs, the number of compartments, identified by the ADAPT method was investigated as a function of varying SNR in the PVE models.

The range of ADAPT orders from (0,0) to (3,3) were also applied to the PVE models (Table 3.4).With the AICc, a distinct number of terms were found to be able to distinguish between two and three-compartment models. The two and three-compartment models were found to be best fitted by ADAPT orders (1,1) and (3,1) with no other competing order found to be significant. All other AICc-LERs were found to be >0.5, indicating that no other fit was statistically significant. The BICc results were found to be similar (Table 3.4), although ADAPT(1,1) was found to be a competing order (BICc-LER= 0.28) for the three-compartment CSF:WM=25:75 signal. The one-compartment CSF model was best fitted by ADAPT(1,1) according to the AICc and ADAPT(1,0) with the BICc. Both list a range of different orders as the optimum fit, indicating that noise can easily corrupt a one compartment signal. The one-compartment signal was investigated at SNR≈100 and decisively found to be represented by ADAPT(0,0) (Figure 3.4), mathematically equivalent to the mono-exponential equation.

Comparing the AICc values of the exponential and ADAPT fitting methods, for the one component signal, the AICc was lowest with ADAPT, indicating a better fit. However, the optimum AICc values are very similar and the RSS values are of the same order of magnitude (RSS for ADC = 1.2×10^{-5}, ADAPT(0,0) = 1.5×10^{-5}, ADAPT(1,1) = 4.0×10^{-6}). For the three component signals, the tri-exponential fits have much lower AICc values than ADAPT(3,1). The RSS values are also two orders of magnitude smaller (i.e RSS for CSF:WM-50:50, TRI = 4.3×10^{-5}, ADAPT(3,1) =1.0×10^{-4}). For the two-component data, the wrongly identified tri-exponential fit has a very low RSS value (RSS for TRI = 4.5×10^{-6}, suggesting that the signal is being overfitted. Although the AICc for IVIM is still lower than ADAPT(1,1) (RSS for IVIM = 1.8×10^{-5}, ADAPT(1,1) = 7.2×10^{-5}), the RSS values are of the same order of magnitude, indicating a similar accuracy of fit.

3.3.2.2 Number of ADAPT Components

The transfer function, Z-transform, PFD and subsequent inverse Z-transform were performed on ADAPT(3,1) which was evaluated to be a three-component decay model(refer to section 3.2.1.6 ADAPT(3,1)).

3.3.3 SNR and Robustness of Data Simulations

3.3.3.1 Influence of Noise upon the Tri-exponential Partial Volume Effects Model

Using the AICc-LERs, the number of compartments identified by the multi-exponential fitting methods (Figure 3.3) and the ADAPT method (Figure 3.4) was investigated as a function of varying SNR. The multi-exponential fitting methods correctly identified the mono-exponential behaviour in the PVE signal CSF:WM 100:0. However, the LER demonstrates that the optimum fit quickly becomes bi-exponential below the high SNR of 85. The three-compartment PVE signals are best represented by the tri-exponential fit down to an SNR of 35 for the CSF:WM of 75:25 and 50:50, and SNR 40 for 25:75. The PVE signal CSF:WM 0:100 is incorrectly represented by a tri-exponential fit. This, however, becomes a bi-exponential fit below SNR 50. CSF:WM 100:0 is best represented by the one component ADAPT(0,0) above an SNR of 75. Below SNR 75 the one component ADAPT(1,0), is the optimum order. However, ADAPT(2,0) and ADAPT(3,0) have AICc-LERs<0.5, indicating significant competing fitting methods. All three-compartment PVE models are best represented by the three-component ADAPT(3,1) down to an SNR of 45. For CSF:WM 0:100, the optimum order is the two-component model ADAPT(1,1) down to an SNR of 45. Below this value the one component models and ADAPT (2,0), another two-component model, begin to show statistical significance.

3.3.4 ADAPT Components Applied to Physical Phantom Acquisition

The ADAPT method was applied to a DWI axial slice of the hydrogel phantom (Figure 3.5).

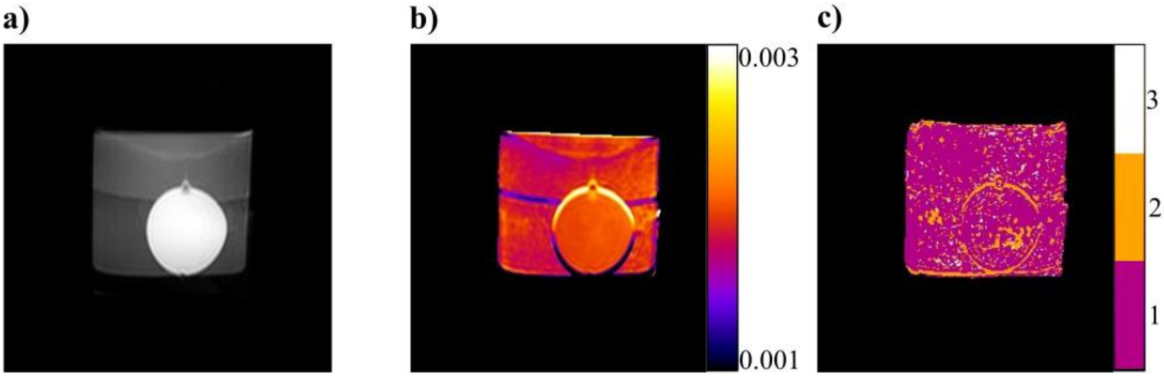

Figure 3.5: Example case of the ADAPT method applied DWI axial slice of hydrogel phantom. a) DWI slice of phantom where b value=0 s/mm^2. b) Apparent Diffusion Coefficient (ADC) parameter map of the phantom (mm^2/s). c) ADAPT applied to the diffusion signal and the corresponding number of detected components are displayed.

As indicated by the ADC (Figure 3.5b), the diffusivity of the hydrogels and water balloon are of the same order of magnitude. The ADAPT method detects one compartment in the hydrogels and water balloon (Figure 3.5c). However, at the interface between the water balloon and the gels, two-compartment behaviour was exhibited.

3.3.5 ADAPT Components Applied to In-Vivo Data Acquisition

The ADAPT method was applied to a DWI axial slice of both a volunteer and a patient case (Figure 3.6). Three ADAPT components were observed as a white line along the boundary of the ventricles for the volunteer case (Figure 3.6c). Such clusters of high order behaviour are consistent with partial volume effects. Few voxels exhibit one-component behaviour in the ventricles of the volunteer. This could be due to the limited size of the ventricles. A patient case was considered in which the ventricles were enlarged. Large clusters of one component behaviour were observed within the ventricles with some three-component behaviour also seen in the region (Figure 3.6d).

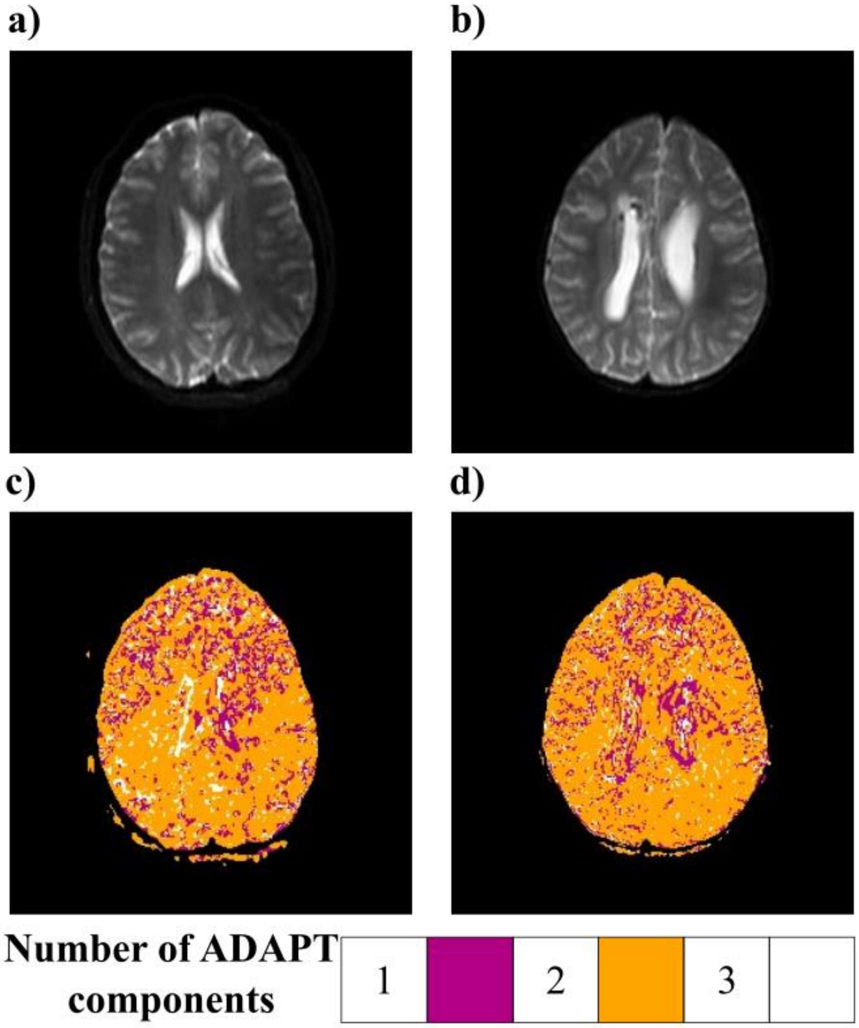

Figure 3.6: Example case of the ADAPT method applied to In-Vivo DWI axial slices. a) DWI slice of a volunteer where b value=0 s/mm^2. b) DWI slice of patient with enlarged ventricles where b value=0 s/mm^2 c) ADAPT applied to volunteer slice and the corresponding number of detected components are displayed. f) ADAPT applied to patient slice.

3.3.6 ADAPT(1,1) Coefficient Study with Data Simulations

The relationship between the ADAPT α and β coefficients, created as a result of minimising (Equation 3.2), and the IVIM f, D and D* parameters were investigated (Figure 3.7).

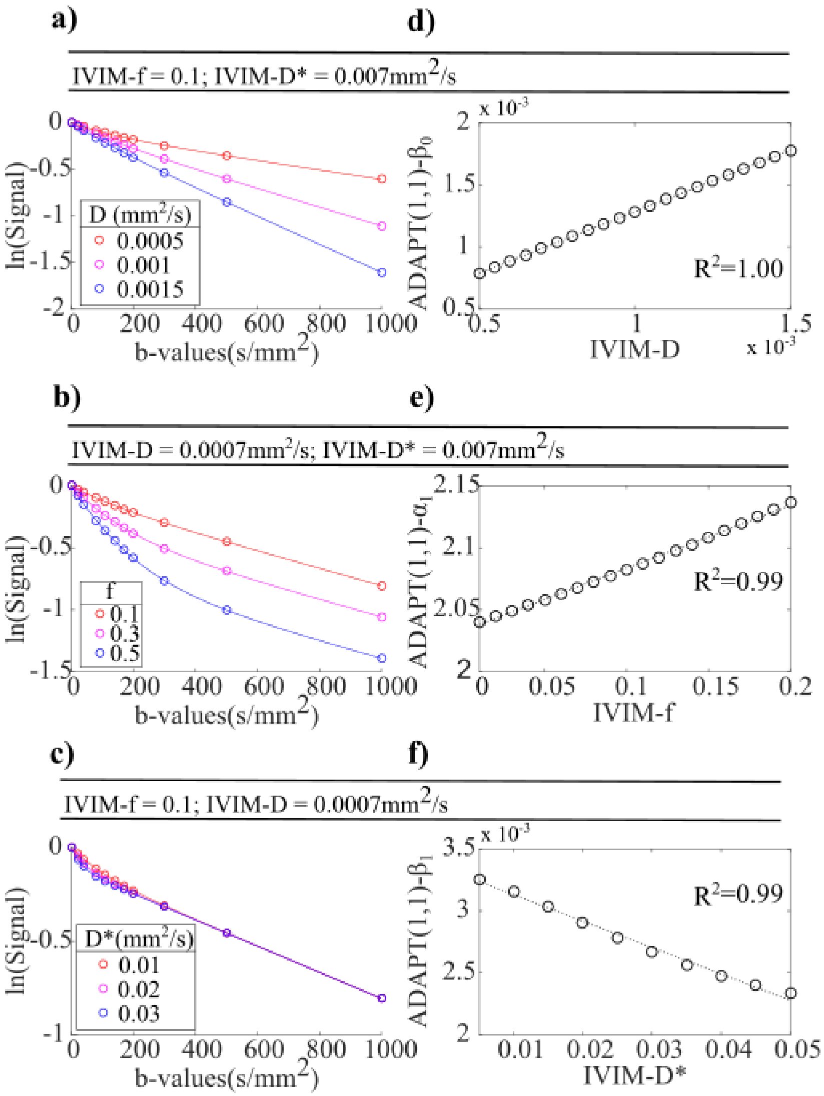

Figure 3.7: The relationship between the ADAPT(1,1) coefficients and the IVIM parameters was investigated. a) Effects on the diffusion signal when only IVIM-D was varied and the other two IVIM parameters were fixed. b) Only IVIM-f varied. c) Only IVIM-D* varied. d) Linear relationship between IVIM-D and ADAPT(1,1)-β_0. e) Between IVIM-f and ADAPT(1,1)-α_1. f) Between IVIM-D* and ADAPT(1,1)-β_1.

If IVIM-f and IVIM-D* are fixed, and only IVIM-D is varied for simulated data, the gradient of the detected diffusion signal can be observed to increase with an increasing IVIM-D value (Figure 3.7a). An increase in the gradient of the signal would also increase the value of the ADAPT-β coefficients and result in a directly linear relationship between the IVIM-D and ADAPT(1,1)-β_0 with R^2=1(Figure 3.7d). When IVIM-f and IVIM-D are fixed, increases in IVIM-D* result in a subtle increase in the gradient at the low b-values (Figure 3.7c). Such behaviour results in a linear correlation between IVIM-D* and the higher-order ADAPT(1,1)-β_1 coefficient with R^2=0.99 (Figure 3.7f). When IVIM-D and IVIM-D* are fixed, and only IVIM-f is varied, an increase in IVIM-f results in an increase in the curvature of the bi-exponential signal and the prevalence of the second component (Figure 3.7b). Consequently a linear relationship is found between IVIM-f and ADAPT(1,1)-α_1 with R^2=0.99 (Figure 3.7e).

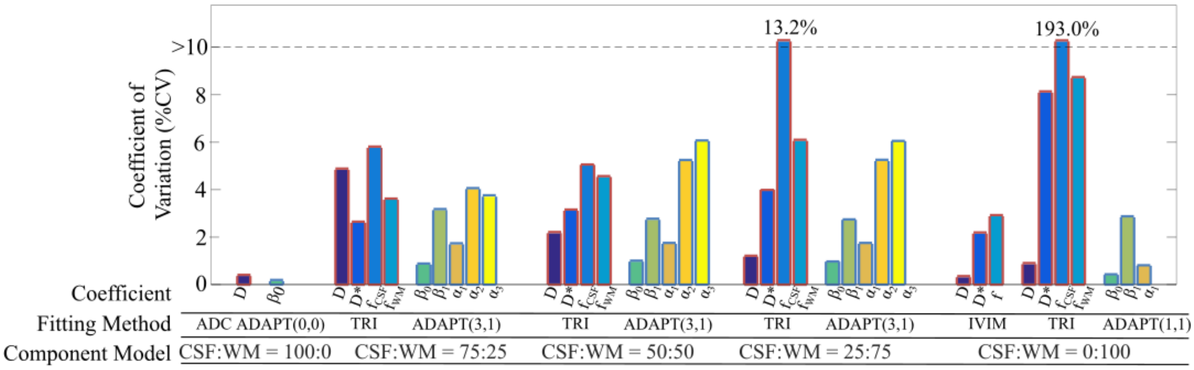

Figure 3.8: Coefficient of Variation calculated for the coefficients of the optimum ADAPT and multi-exponential fitting methods for each of the PVE models (SNR ≈ 50) considered. For the one-component model, CSF:WM=100:0, the ADC and ADAPT(0,0) fitting methods were implemented. For the two-component models, CSF:WM=75:25,50:50 and 25:75, the tri-exponential and ADAPT(3,1) fitting methods were implemented. For the three-component models, CSF:WM=0:100, the tri-exponential and ADAPT(1,1) fitting methods were implemented. The IVIM method was also considered. For each of the fitting methods implemented, the respective coefficients were investigated.

The coefficients of ADAPT and the multi-exponential fitting methods were investigated for the PVE models (SNR≈50) (Figure 3.8). For the one-compartment model, the optimum mono-exponential fitting method and ADAPT(1,0) were considered. ADAPT(0,0) was also considered due to being mathematically equivalent to the mono-exponential equation. The CV was found to be 0.4% for the mono-exponential ADC and 0.2% for ADAPT(0,0)-β_0. Both have a CV <1% indicating that both fitting methods were robust for fitting one compartment data. For ADAPT(1,0), β_0 had a CV of 0.6% and α_1 2735.7%. The β_0 coefficients from ADAPT(0,0) and ADAPT(1,0) had a percentage variation of 0.0002%. Given the similarity in β_0 coefficients and the high CV for ADAPT(1,0)-α_1, it can be theorised that the additional parameter in the one component ADAPT(1,0) is a consequence of the noise added to the signal. For the three-compartment models, the optimum fitting methods, ADAPT(3,1), and the tri-exponential fit were compared. In general, the ADAPT(3,1) coefficients have a lower CV than the tri-exponential parameters. α_2 and α_3 have a higher CV than the TRI-f_{CSF} and f_{WM} parameters for the CSF:WM=50:50 case, but the CV is still less than 6.1%. For the CSF:WM=25:75 case, the TRI-f_{CSF} had a CV of 13.2% significantly higher than any of the other parameters associated with three compartments. For the two-compartment model, ADAPT(1,1) was compared against both the bi- and tri- exponential fitting methods. Although selected as the optimum multi-exponential fit, it is evident that the tri-exponential is the incorrect fit as the CV of TRI-f_{CSF} is 193.0%. Comparing the ADAPT(1,1) coefficients to the IVIM parameters, β_0, β_1, and α_1 had CVs of 0.4%, 2.8% and 0.8% respectively. IVIM-D, IVIM-D* and IVIM-F were 0.3%, 2.2% and 2.9%. Both methods possessed low CVs for their parameters indicating that ADAPT(1,1) and IVIM are both robust fitting methods for two-compartment signals.

3.3.7 ADAPT(1,1) Coefficient Study with In-Vivo Data

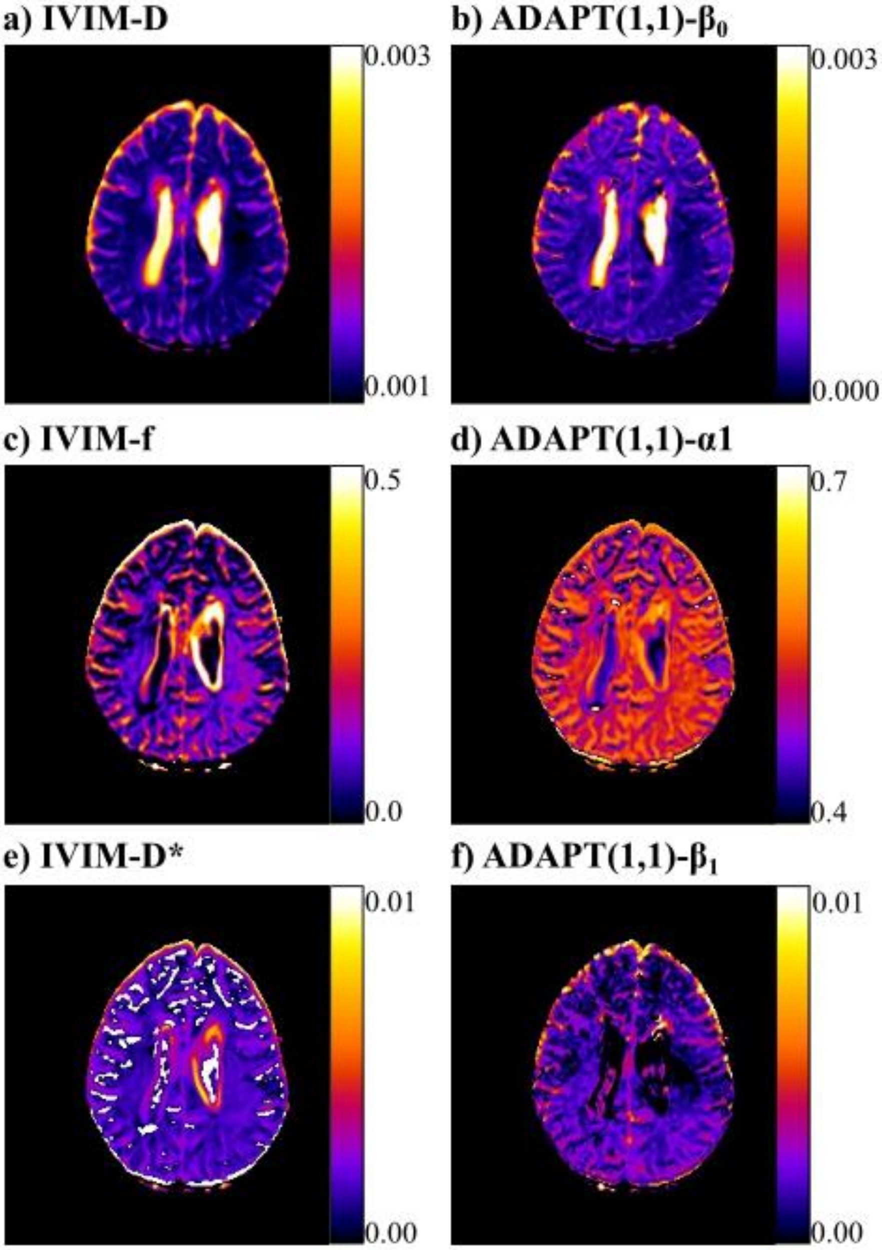

Figure 3.9: Parametric maps of Axial brain slice of patient with enlarged ventricles a) IVIM-D (mm^2/s); c)IVIM-f; e)IVIM-D* (mm^2/s); b) ADAPT(1,1)-β_0; d)ADAPT(1,1)-α_1; f)ADAPT(1,1)-β_1.

The ADAPT(1,1)-β_0 (Figure 3.9b), α1 (Figure 3.9d) and β_1 (Figure 3.9f) coefficients for an In-Vivo axial slice of a patient brain scan were correlated on a pixel-wise basis with the IVIM-D (Figure 3.9a), IVIM-f (Figure 3.9c) and IVIM-D* (Figure 3.9e) parameters respectively. Upon visual inspection, the IVIM-D and ADAPT(1,1)-β_0 parametric maps appear similar with the calibration bars also showing comparable scales. Furthermore, when the voxels with ADAPT(1,1) identified as the optimum order were selected (n=6002), s=0.708 (P <0.001) was obtained, indicating a strong relationship between IVIM-D and ADAPT(1,1)-β_0. However, the edges of the ventricles appear to be affected by partial volume effects more in the IVIM maps than the ADAPT maps. IVIM-D* and ADAPT(1,1)-β_1 were found to have an s= 0.741 (*P*<0.001), also indicating a strong relationship. The CPU run time of the IVIM fit for one slice was averaged over 10 iterations and found to be 575.0 ± 3.1 seconds. Comparatively the CPU run time of ADAPT method was just 23.2 ± 0.1 seconds.

The CV was calculated from the average coefficient values calculated from ROIs within the CSF and WM (Table 3.5). For the one compartment CSF, ADAPT(0,0)-β_0 was almost identical to the ADC value and the CV <1.5%. For the two-compartment WM, ADAPT(1,1)-β_0 was found to be the same order of magnitude as IVIM-D although the CV of IVIM-D was found to be just 4.6% compared to 10.7% for β_0. However, ADAPT(1,1)-α_1 has a lower CV than IVIM-f 16.7% compared to 18.2%. ADAPT(1,1)-β_1 has a significantly lower CV than IVIM-D*, 25.0% compared to 78.7%.

Table 3.5: Optimum Fitting Methods applied to In-Vivo ROIs- Parameter coefficient of variation (CV)

Number of compartments	**Parameter**	**Average**	**Standard Deviation.**	**CV (%)**
1	ADC	2.89E-03	4.04E-05	1.40
	(0,0)-b0	2.90E-03	3.73E-05	1.30
2	IVIM-D	8.66E-04	4.01E-05	4.64
	(1,1)-b0	6.24E-04	6.71E-05	10.77
	IVIM-D*	4.66E-02	3.67E-02	78.65
	(1,1)-b1	1.01E-03	2.53E-04	24.98
	IVIM-f	0.074	0.013	18.16
	(1,1)-a1	0.601	0.100	16.65

ROIs were drawn within the WM and CSF on the patient axial slice (Fig. 5b). The parameter values for the optimum methods were calculated.

3.4 Discussion

It has been demonstrated that the number of components in diffusion-weighted MRI data is determined unreliably by simply applying multi-exponential fitting methods and then selecting the optimum fit. For the simulations considered, the ADAPT method is superior at identifying multiple components.

In the physical phantom, the ADAPT method was able to correctly identify bi-exponential behaviour at the interface between the two mono-exponential components. However, to recreate a partial volume effect exhibiting tri-exponential behaviour, a considerably more complex phantom, with flow effects, would be required. Consequently, the development of a physical phantom is beyond the scope of this thesis.

In simulations, the ADAPT method also demonstrated that it could correctly identify the number of components in the bi-exponential signal across a large range of IVIM parameter values. The SNR analysis demonstrated that ADAPT was more robust at detecting both one and two-compartment signals.

In simulations, ADAPT was superior at identifying three-component behaviour, even when the third component is more subtle, i.e. PVE model with CSF:WM 75:25. However, the BICc did detect competing orders, indicating that the third compartment could be difficult to detect for cases where the fraction of CSF is more subtle. Although the tri-exponential fitting methods had lower RSSs than ADAPT(3,1) for the three-compartment PVE models, the low RSSs are more likely due to the study being culpable of the inverse crime (refer to section 3.5 Study Limitations) and the tri-exponential fitting method being inherently biased towards the simulated tri-exponential data. Furthermore, the RSS values for the optimum ADAPT orders were still low, and the model selection was more robust. It is recommended that if the number of compartments in a signal is unknown, the ADAPT method should be used instead of multi-exponential fitting for model selection.

ADAPT is a generalisation of exponential models and makes no prior assumptions about the number of components within the data. Thus ADAPT lends itself as a potential novel method for the detection of the number of components in DWI data. The data simulations indicated that there is a relationship between the IVIM parameters and ADAPT coefficients. A strong relationship between these two methods is also evident in the In-Vivo patient example. Although the relationship between the IVIM parameters and ADAPT coefficients is complex and non-linear, ADAPT presents the opportunity for complex diffusion biomarkers to be obtained by making no prior assumptions about the nature of the data nor does it require any multistep fitting processes.

Consequently, in this study, ADAPT is a much faster fitting method. The In-Vivo ROIs showed that ADAPT(1,1) and IVIM had comparable parameter CVs. However, IVIM-D* was considerably higher. Although this may be due to tissue heterogeneity within the white matter, the average IVIM-D* value is higher than expected (111), indicating that ADAPT may be more robust than IVIM at fitting in WM.

Both the ADAPT and multi-exponential fitting methods struggled to correctly identify the number of signal components at poor SNRs (< 45). The addition of noise to the tri-exponential PVE models resulted in the methods under-fitting the signal. This was most likely due to noise modulating the true signal and causing individual components to be mistakenly classified together. The addition of noise to the mono-exponential fitting method resulted in overfitting the signal. Although ADAPT was still able to detect a one-component model at poor SNR, the optimum order, using the AICc, switched from ADAPT(0,0) to ADAPT(1,0) resulting in an additional parameter. Although more robust than the multi-exponential fitting methods, the ADAPT method requires further development to optimise how it handles low SNR data, and the inclusion of an additional component or parameter to account for noise should be considered.

3.5 Study Limitations

In general, the AICc and BICc selected the same optimum order, increasing the confidence that the most appropriate order had been selected. However, a more formal protocol is required for when the information criterion methods disagree.

One should note that only one range of clinically relevant b-values was considered for the data simulated or acquired In-Vivo in this study. The number of data points and their magnitude could have a significant influence on the performance of the ADAPT method and the generality of the findings. However, there is no clear consensus on what optimal b-value sequence should be used for DWI (199). As the ADAPT method requires a discrete approximation of the diffusion signal, there will inevitably be a truncation in the approximation, which is inherent to the method. Another limitation of the simulations in this study was the assumption that diffusion in the CSF exhibits mono-exponential behaviour, consequently the effects of CSF circulation or pulsatile flow (200) were not considered. However, such effects are assumed to have a minimal contribution to the observed signal. Given the limited spatial resolution, it is also difficult to ensure that choroid plexus does not contribute to voxels in close proximity.

As far as the authors are aware, no other diffusion models with a perfusion fraction exist for simulating data other than the multi-exponential equations explored. Therefore it was not possible to avoid committing the ‘inverse crime’ (IC) where multi-exponential equations were used to simulate as well as fit the data. To mitigate the IC, Gaussian noise was added to the simulated data (201), and a range of different multi-exponential models were explored. In addition, the ADAPT method is a different mathematical model, and therefore the IC wasn’t committed with this class of models. Hence the IC would more likely favour multi-exponential fitting methods such as IVIM.

The study only considered DWI data, which averages over all the directions in which a gradient is applied. Consequently, this method is only able to measure isotropic diffusion compartments. If anisotropic effects, such as fanning or crossing of axon bundles, were to be investigated, many diffusion-weighted images, with diffusion-weighted gradients in different directions, would be required resulting in Diffusion Tensor Imaging (DTI). Although multi b-value models are not yet routine in clinical settings, it would be interesting to consider an application of ADAPT to this technique, in particular investigating anisotropic effects with further simulations and In-Vivo studies.

Further investigations are required to understand how the number of optimum ADAPT components relates to the number of exponential terms within the signal. This is considered in Chapter 5 with further rearrangement of the transfer function.

3.6 Conclusion

The ADAPT method has shown that it can distinguish between multi-exponential diffusion data containing different numbers of components, which cannot be achieved by applying multi-exponential fitting methods and selecting the optimum fit. This novel method allows for the identification of different components within a diffusion signal. The relationship between the ADAPT and IVIM parameters suggest that diffusion biomarkers can be obtained without making prior assumptions about the nature of the data. Whilst ADAPT has been applied to DWI data; it should find application in other multi-exponential data sets which can be manipulated to be represented as a function of acquisition points.

Chapter 4

Correlation of Perfusion Effects in DWI with Perfusion MRI

4. Correlation of Perfusion Effects in DWI with Perfusion MRI

In this chapter, the coefficients of the ADAPT method and their relationship to perfusion information are further investigated. The correlation between the Dynamic Susceptibility Contrast (DSC), relative Cerebral Blood Volume (rCBV) and the ADAPT coefficients are investigated and compared to the correlation between rCBV and IVIM-f.

4.1 Introduction

Perfusion MRI uses techniques sensitive to cerebral haemodynamics in order to attain quantitative parametric maps. The most prevalent perfusion MRI technique used in clinical investigations is Dynamic Susceptibility Contrast (DSC) MRI (202). The DSC parameter Cerebral Blood Volume (CBV), has demonstrable clinical value in the grading of gliomas (203), predicting tumour progression (204) and assessing treatment response (205).

However, the routine use of DSC is confounded by the lack of consensus for an optimised DSC-MRI protocol (31) or for the gadolinium contrast agent injected (27). Furthermore, absolute quantification of parameters can be difficult to determine (28), and post-processing results can be user-dependent (22). There is some concern regarding the Gadolinium bolus (135). The use of some gadolinium contrast agents is restricted in some populations, such as young children (206). Recent studies have also found gadolinium deposits accumulating in patient’s brains and other organs after multiple injections of the contrast agent (136). Hence a contrast free method for measuring perfusion is desirable.

Arterial Spin Labelling (ASL) is another perfusion MRI technique that is gaining considerable attention. ASL doesn’t require an injectable contrast, instead relying on the labelling of arterial blood as it flows through the brain. However, DSC has a higher signal to noise ratio (SNR) (33) and better temporal and spatial resolution (207). In addition, the image acquisition time of ASL protocols is significantly longer than that of DSC (22).

Contrast free perfusion measurements may also be possible with Diffusion-Weighted Imaging (DWI). The Intravoxel Incoherent Motion (IVIM) model (90) is a bi-exponential equation with two components related to diffusion and perfusion-related measurements, respectively. The perfusion-related parameters, IVIM-D*; the pseudo-diffusion coefficient and IVIM-f; the volume fraction of flowing blood in the tissue, have been shown to be correlated with perfusion MRI parameters (42). Assuming the microvascular network is randomly orientated and isotropic, the relationship between IVIM-f and CBV is linear (208).

Several studies have investigated the correlations between CBV and IVIM-f (38,111,120,138,140,209–212), with most reporting a moderate correlation (Federau et al. determined a Pearson's r=0.59 in Gliomas (38), Kim et al. determined r=0.67 (P<0.001) in Glioblastomas (138)). Moderate correlations have also been reported in healthy tissue (Wirestam et al. r=0.56 (P<0.001) (212), Wu et al. r=0.29-0.48 in Grey Matter (111)). In contrast Bisdas et al. reported a negative correlative with Spearman's rank, s=-0.57(P=0.09) in healthy tissue and s=-0.43(P=0.10) in Gliomas (140), although results were not significant. A poor correlation has been observed in regions of white matter (Wu et al. r=-0.02-0.05 (111)).

Across the correlation studies considered, variables that could impact the correlations are highly varied. The IVIM model is implemented with a range of different fitting methods (unconstrained and constrained with a multi-step approach) and different b-value distributions. The effects of different IVIM fitting methods upon the correlation between

IVIM-f and CBV have previously been reported (212).The selection and size of the region of interest (ROI) is highly varied. The parameters, CBV and IVIM-f, are either fitted for the ROIs on a voxel-wise basis (140,209) or just for the signal average (120,212). The correlations are performed either voxel-wise for individual cases (111) or across the whole cohort taking the average (38), maximum (211) or 90th percentile (138) parameter values for each ROI.

The choice of fitting method used to determine the IVIM parameters significantly affects the estimation of the IVIM-f parameter (121) and therefore, the correlation with CBV. The assumption of two-components by the IVIM model could also affect the correlation with some diffusion models predicting multiple perfusion components within the diffusion signal (35). An alternative model for fitting multi-component diffusion signals is the Auto-Regressive Discrete Acquisition Points Transformation (ADAPT) method. The ADAPT method is based on the Auto-Regressive Moving Average model (174), a generalised multi-exponential model. ADAPT has the ability to represent a wide range of data sets and is not constrained to assume bi-exponential behaviour. The fitting method does not require any initial starting values or any multi-step fitting processes for robust parameters. ADAPT presents the opportunity for novel biomarkers to be obtained with no prior assumption about the nature of the data. In the previous chapter (Chapter 3), ADAPT(1,1) was shown to be the optimum ADAPT model for fitting bi-exponential behaviour (213). In addition, the parameter ADAPT(1,1)-$\alpha 1$ was shown to correlate strongly with IVIM-f.

In this chapter, the correlation between rCBV (relative CBV, which has been normalised to white matter) and IVIM-f is investigated for a cohort of children with brain tumours (n=15). The correlation between rCBV and ADAPT(1,1)-$\alpha 1$ is also investigated and compared to the correlation with IVIM-f. The impact of the number of components in the diffusion signal upon the perfusion-related measurements is also considered.

4.2 Materials and Methods

4.2.1 Study Population

Fifteen Paediatric brain tumour cases (5 Females, 10 Males, Age Range 1.6 – 10.3 years, Median 6.2 years) were considered for the evaluation of the correlation between rCBV and the DWI parameters (Table 4.1). Informed consent was obtained and the East Midlands – Derby Research Ethics Committee (REC 04/MRE04/41) approved the study operating under the rules of Declaration of Helsinki 1975 (and as revised in 1983).

Table 4.1: Patient cohort demographic for the correlation study

Case	Age (Years)	Sex (M/F)	Diagnosis
1	9.1	M	Glioneuronal tumour
2	5.8	F	Optic pathway glioma
3	6.5	M	Optic pathway glioma
4	4.1	M	Optic pathway glioma
5	6.5	F	Ganglioglioma
6	6.9	F	Optic pathway glioma
7	10.3	F	Pilocytic Astrocytoma
8	1.7	M	Thalamic optic pathway glioma
9	1.6	M	Optic pathway glioma
10	2.6	M	Supratentorial low-grade glioma
11	8.6	M	Suprasellar pilomyxoid astrocytoma
12	6.2	M	Multisystem Langerhans Cell Histiocytosis
13	3.3	M	Optic pathway glioma
14	6.2	F	Optic pathway glioma
15	5.0	M	Ganglioglioma

4.2.2 MRI Data Acquisition

All patients were scanned on a Philips Achieva 3T TX (Philips Healthcare, Best, the Netherlands) MRI scanner at Birmingham Children's Hospital using a 32-multichannel receiver head coil. A T2-weighted TSE scan was performed using the following parameters: FOV 240mm x 240mm, TR/TE 4000/100ms, matrix size 288×288, 30 slices with 3.5mm slice thickness and in-plane resolution 0.9mm × 0.9mm.

The Diffusion-weighted MRI sequence, acquired with the same coverage as the T2 scan, used a sensitivity-encoded (SENSE) approach with single-shot, spin-echo (EPI) sequence and the following parameters: FOV 240mm x 240mm, TR/TE 4000/91ms, matrix size 96×96, 30 slices with 3.5mm slice thickness and in-plane resolution 2.5mm × 2.5mm. A b-value sequence of 11 exponentially spaced b-values between 0 and 1000 s/mm^2, [0, 20, 40, 80, 110, 140, 170, 200, 300, 500, 1000] s/mm^2, was acquired in three orthogonal directions. The scan duration of the diffusion protocol was 2.12 minutes.

The DSC protocol was performed following the DWI protocol and was acquired with the same coverage as the T2 and the DWI scan. The FOV and image resolution of the DSC protocol was identical to that of the DWI protocol. The DSC scan was an axial FE-EPI scan with the parameters: TR/TE 1865/40ms, flip angle 20° and temporal resolution 1.86s, which was repeated 60 times. The gadolinium contrast agent (Dotarem, Guerbet, Frace) was administered via a power injector through a cannula inserted in an antecubital vein. The dose was administered in two stages; the first dose was administered before the DSC acquisition as a pre-bolus to minimise T1 effects (214). The second dose was administered at the start of time point 5 in the DSC data acquisition. The total dose of contrast agent given was 0.1 mmol/kg with an injection rate of 3 mL/s. Each dose was subsequently followed by a saline injection at the same rate, up to 10mL dependent on the patient’s weight.

4.2.3 Data Analysis

The IVIM equation is given as (Equation 4.1):

$$\frac{S_{(b)}}{S_{(0)}} = f \cdot \exp\left(-bD^{*}\right) + (1 - f) \cdot \exp\left(-bD\right) \tag{4.1}$$

Where S(b)/S(0) is the signal intensity of the normalised signal for a particular b-value; IVIM- D is the diffusion coefficient; IVIM-D* is the pseudo-diffusion coefficient; and IVIM-f is the volume fraction of incoherently flowing blood in the tissue describing the fraction of the signal arising from the vascular network (36). The IVIM model was fitted to the diffusion scans using a non-linear least-square fitting, and a constrained one-parameter fitting method (121). This model assumes that the effects of perfusion are negligible in measurements at high b-values. For b-values > 200 s/mm^2, a monoexponential fitting method is implemented. By plotting the signal on a logarithmic scale and calculating the gradient and y-intercept, IVIM-D and IVIM-f can be calculated respectively. The fitting method was applied on a voxel by voxel basis.

The ADAPT equation is given as (Equation 4.2):

$$\ln(S_n) = \sum_{i=0}^{Q} \beta_i b_{n-i} + \sum_{j=1}^{P} \alpha_j ln\left(S_{n-j}\right) \tag{4.2}$$

Where S_n is the signal at acquisition point n, b_n is the b-value at acquisition point n, and α_j, β_i are the minimisation coefficients. At each acquisition point, the signal value can be modelled as a linear combination of the previous b-values and corresponding signal values. The parameters P and Q indicate the number of previous terms that the input signal depends upon. The ADAPT order ADAPT(1,1) was considered (Equation 4.3):

$$\ln(S_n) = \beta_0 b_n + \beta_1 b_{n-1} + \alpha_1 ln(S_{n-1}) \tag{4.3}$$

The ADAPT parameters β0, β1 and α1 were established using the matrices (Equation 4.4):

$$S = \begin{bmatrix} b_{(0)} & 0 & 0 \\ b_{(1)} & b_{(0)} & ln\left(\frac{S_{(0)}}{S_{(0)}}\right) \\ \vdots & \vdots & ln\left(\frac{S_{(1)}}{S_{(0)}}\right) \\ \vdots & \vdots & \vdots \\ b_{(N)} & b_{(N-1)} & ln\left(\frac{S_{(N-1)}}{S_{(0)}}\right) \end{bmatrix}; \quad A = \begin{bmatrix} \beta_0 \\ \beta_1 \\ -\alpha_1 \end{bmatrix}; \quad S_{pred} = \begin{bmatrix} \ln\left(\frac{S_{(0)}}{S_{(0)}}\right) \\ \ln\left(\frac{S_{(1)}}{S_{(0)}}\right) \\ \vdots \\ \ln\left(\frac{S_{(N)}}{S_{(0)}}\right) \end{bmatrix} \qquad (4.4)$$

Where S is a matrix constructed from the b-values and the detected signal with acquisition point n=0, …, N. A is the matrix of ADAPT coefficients. S_{pred} is the final model of the normalised predicted signal. By finding the least-squares error of Equation 4.4, A is minimised, and the model S_{pred} is established:

$$S \cdot A = S_{pred} \qquad (4.5)$$

The ADAPT method was used to determine the number of components. A range of ADAPT orders from ADAPT(0,0) to ADAPT(3,3) were fitted to each diffusion signal. The optimum fit was selected using the corrected Akaike Information Criterion (AICc) (173).ADAPT orders between ADAPT(0,0) and ADAPT(1,0) identified signals with one component, between ADAPT(1,1) and ADAPT(2,2) identified two component signals and between ADAPT(3,0) and ADAPT(3,3) identified three component signals (213).

The rCBV parametric map was derived from the DSC scan. The tracer tissue concentration-time course data was obtained from the signal-time course data by considering the relationship between the tracer tissue concentration and the T2* signal intensity. By considering the area below the tracer tissue concentration-time course, the rCBV value was attained with arbitrary units mL/100 mL. Leakage corrections were applied using preload-dosing and baseline subtraction techniques, further details of the method can be found in J. Novak and S. Withey et al. (215).

Tumour regions of interest (ROI) were drawn manually on the T2-weighted images (Average Tumour ROI=461 ± 243 voxels). Areas of cyst were excluded from the ROIs. Grey Matter (GM) and White Matter (WM) masks were created using the Brain Extraction Tool (BET) (216) and the FMRIB's Automated Segmentation Tool (FAST) (217) from the FMRIB Software Library v6.0 (Analysis Group, Oxford, UK) using the T2-weighted images. A probability map was generated predicting whether a voxel was WM, GM or cerebrospinal fluid (CSF). WM and GM masks were created, using only voxels with a 100% probability of being that tissue type. To further mitigate the effects of partial volumes, an image erosion of 1 voxel was applied to each mask. The Tumour ROI, areas of cyst and CSF were masked out with an additional exclusion of 2 voxels around these areas- (Average GM ROI=4999 ± 1654 voxels, Average WM ROI=5719 ± 2149 voxels) (Figure 4.1).

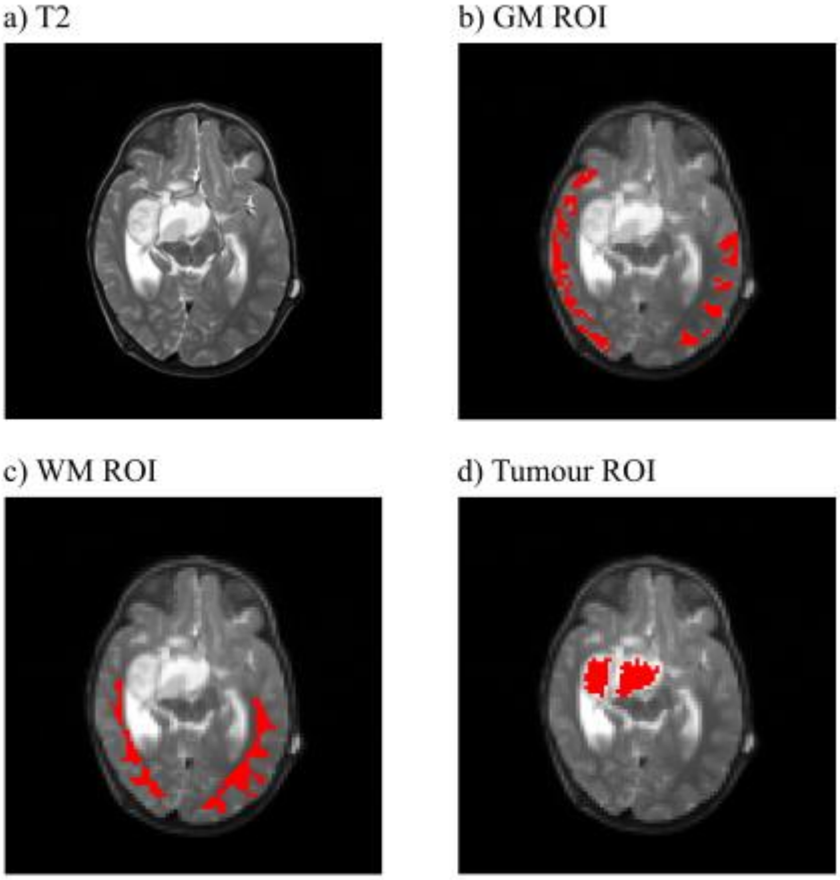

Figure 4.1: Example of Region of Interests (ROIs) drawn for each tissue type considered in the correlation study. a) T2 axial slice of the whole brain. b) grey matter selected, c) white matter selected, d) tumour selected.

4.2.4 Statistical Analysis

For each of the cases in the study population, the correlation analysis between rCBV and IVIM-f was assessed using Spearman's rank correlation coefficient. The correlation between rCBV and ADAPT(1,1)-α1 was also considered. The two correlations were directly compared across the whole brain and GM, WM and Tumour ROIs. A summary statistic for the cohort was established by considering the correlation across all cases. The average correlation for each ROI was determined by implementing the Fischer-Z transformation (35) to normally distribute the correlation coefficients. As the correlations to compare are dependent and overlapping, Zou's 95% confidence intervals were calculated with lower and upper bounds to assess if one correlation was statistically stronger than the other (36). The mean, median and standard deviation were also calculated for each parameter across all voxels in each of the tissue types considered.

4.3 Results

4.3.1 rCBV, IVIM-f and ADAPT(1,1)-α1 Parameter Comparison

Parametric maps of rCBV, IVIM-f and ADAPT(1,1)-α1 were calculated on axial slices from the cohort (Figure 4.2).

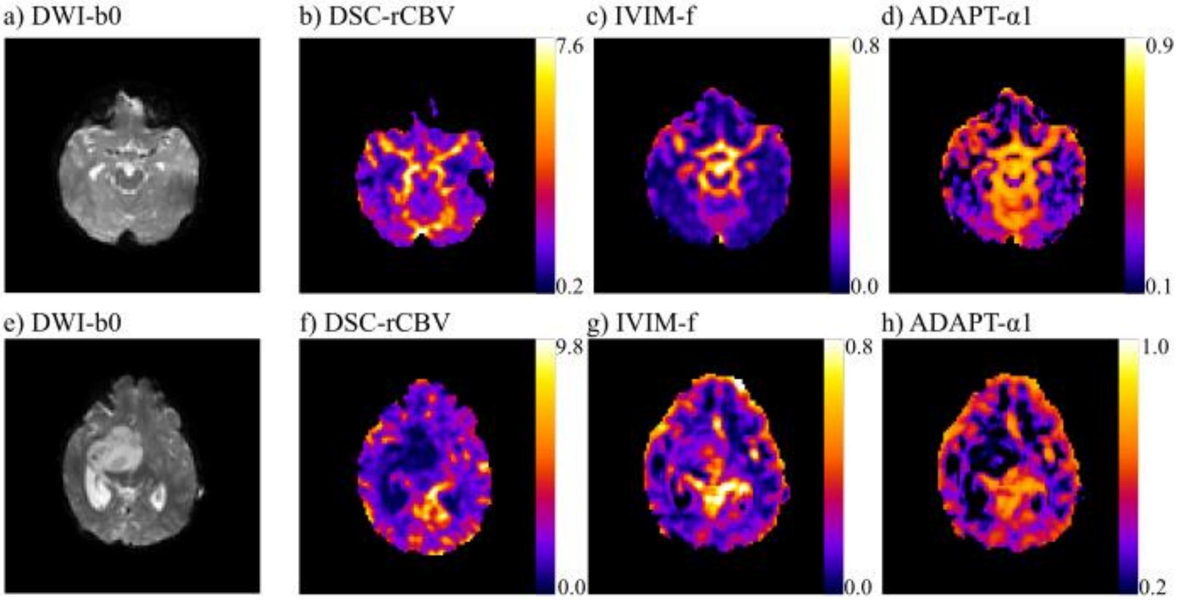

Figure 4.2: Example parameter maps for the perfusion measurements: a) axial b0 image of Optic pathway Glioma case and corresponding parameter maps b)DSC-rCBV, c) IVIM-f, d)ADAPT(1,1)-α1, e)axial b0 image of Suprasellar pilomyxoid astrocytoma and corresponding parameter maps f)DSC-rCBV, g) IVIM-f, h)ADAPT(1,1)-α1

Upon visual inspection, the parametric maps appear similar with the calibration bars for the diffusion measurements showing comparable scales.

Spearman's rank was calculated on a voxel-wise basis for each of the cases across the whole brain and GM, WM and Tumour ROIs. The Spearman's rank correlation is reported for each of the cases in Table 4.2:

Table 4.2: Spearman’s Rank correlations between DWI measurements and rCBV for each case in the cohort considering the whole brain. P < 0.001 for all measurements.

Whole Brain								
Spearman's Rank				Zou's 95% CI				
Case	rCBV IVIM-f	rCBV ADAPT(1,1)-α1	IVIM-f ADAPT(1,1)-α1	n	Fisher Z	Lower Bound	Upper Bound	Strongest Correlation
1	0.471	0.574	0.830	33823	-38.24	-0.11	-0.10	ADAPT(1,1)-α1
2	0.440	0.456	0.917	32749	-7.77	-0.02	-0.01	ADAPT(1,1)-α1
3	0.413	0.456	0.922	36647	-23.13	-0.05	-0.04	ADAPT(1,1)-α1
4	0.262	0.485	0.731	38503	-64.95	-0.23	-0.22	ADAPT(1,1)-α1
5	0.447	0.422	0.698	37560	7.10	0.02	0.03	IVIM-f
6	0.584	0.576	0.968	34649	6.92	0.01	0.01	IVIM-f
7	0.404	0.336	0.936	26655	33.16	0.06	0.07	IVIM-f
8	0.451	0.589	0.892	35982	-64.34	-0.14	-0.13	ADAPT(1,1)-α1
9	0.403	0.471	0.868	39494	-29.18	-0.07	-0.06	ADAPT(1,1)-α1
10	0.463	0.503	0.868	44628	-18.73	-0.04	-0.03	ADAPT(1,1)-α1
11	0.398	0.610	0.833	36024	-78.31	-0.22	-0.21	ADAPT(1,1)-α1
12	0.704	0.672	0.965	27078	27.66	0.03	0.04	IVIM-f
13	0.502	0.597	0.910	31745	-46.65	-0.10	-0.09	ADAPT(1,1)-α1
14	0.529	0.576	0.949	35955	-33.34	-0.05	-0.04	ADAPT(1,1)-α1
15	0.277	0.387	0.857	37089	-42.00	-0.11	-0.10	ADAPT(1,1)-α1

Significant correlations were achieved in all cases with moderate correlations observed between rCBV and IVIM-f (s= 0.277-0.704, P<0.001) and rCBV and ADAPT(1,1)-α1 (s=0.336-0.672, P<0.001). Strong correlations were observed between the diffusion measurements IVIM-f and ADAPT(1,1)-α1 (s=0.731-0.968, P<0.001). As determined by Zou’s confidence interval, the correlation between rCBV and ADAPT(1,1)-α1 was statistically stronger than the correlation between rCBV and IVIM-f in 11 of the 15 cases considered.

The Spearman's rank correlations for each of the cases are shown for all of the tissue types considered in Figure 4.3. In the GM ROIs, ADAPT(1,1)-α1 had the strongest correlation to rCBV in 12 of the 15 cases, IVIM-f had a stronger correlation to rCBV in one case, and for two cases the correlations were determined to be of statistically comparable strength. For the WM ROIs, in relation to rCBV, ADAPT(1,1)-α1 had the statistically stronger correlation in 9 cases, IVIM-f in 5 cases and for one case the correlations were determined to be of statistically comparable strength. For the Tumour ROIs, in relation to rCBV, ADAPT(1,1)-α1 had the statistically stronger correlation in 7 cases, IVIM-f in 2 cases and for 6 cases, the correlations were determined to be of statistically comparable strength.

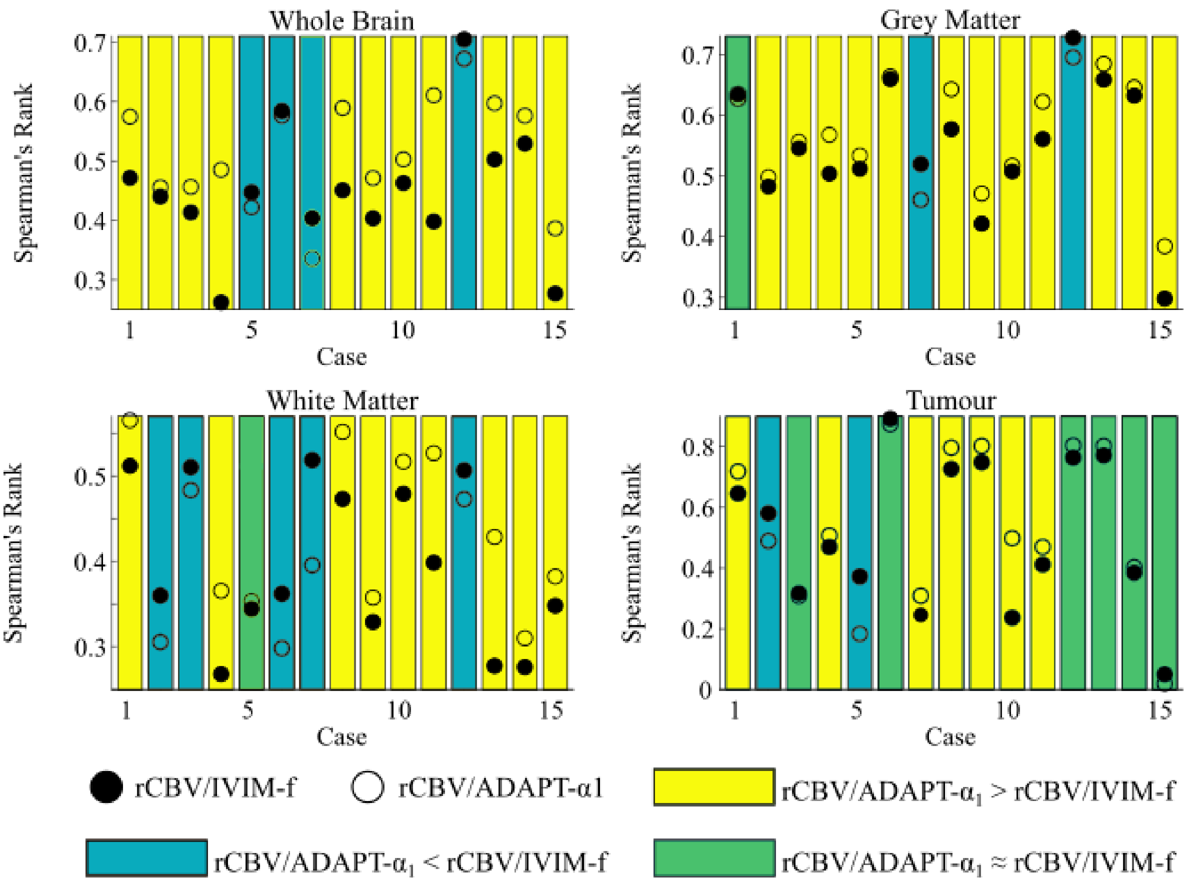

Figure 4.3: Spearman's Rank correlations between DWI measurements and rCBV for each case in the cohort considering the whole brain and regions of Grey Matter, White Matter and Tumour. P <0.001 for all measurements.

Considering the average correlation across the whole cohort (Table 4.3), the correlation between rCBV and ADAPT(1,1)-α1(s=0.520, P<0.001) was determined to be statistically stronger than the correlation between rCBV and IVIM-f (s=0.433, P<0.001). For the average Spearman’s rank correlation, the correlation between rCBV and ADAPT(1,1)-α1 was statistically stronger across GM, WM and Tumour ROIs for the whole cohort.

Table 4.3: Spearman’s Rank DWI measurements and CBV for the different tissue types. The Average and total correlations across the cases are reported, P < 0.001 for all measurements.

	Spearman's (s)					Zou's 95% CI		
ROI	rCBV IVIM-f	rCBV ADAPT(1,1)-α1	IVIM-f ADAPT(1,1)-α1	n	Fisher Z	Lower Bound	Upper Bound	Strongest Correlation
Average								
Whole Brain	0.433	0.520	0.897	35238	-40.72	-0.09	-0.08	ADAPT(1,1)-α1
Grey Matter	0.557	0.578	0.929	4999	-4.82	-0.03	-0.04	ADAPT(1,1)-α1
White Matter	0.401	0.425	0.898	5719	-4.43	-0.03	-0.01	ADAPT(1,1)-α1
Tumour	0.520	0.568	0.892	460	-2.66	-0.08	-0.01	ADAPT(1,1)-α1
Total								
Whole Brain	0.397	0.471	0.712	491735	-77.42	-0.08	-0.07	ADAPT(1,1)-α1
Grey Matter	0.506	0.521	0.768	60134	-6.71	-0.02	-0.01	ADAPT(1,1)-α1
White Matter	0.395	0.419	0.697	74384	-9.22	-0.03	-0.02	ADAPT(1,1)-α1
Tumour	0.480	0.649	0.807	4254	-21.28	-0.19	-0.15	ADAPT(1,1)-α1

The average correlations for each region of interest considered were statistically stronger between rCBV and ADAPT(1,1)- α1 than between rCBV and IVIM-f across the cohort. Between rCBV and ADAPT(1,1)- α1, Spearman’s rank, s=0.520, 0.578, 0.425, 0.568 and between rCBV and IVIM-f, s=0.433, 0.557, 0.401, 0.520 (P<0.001) across the whole brain and regions of grey matter, white matter and tumour respectively.

Spearman's rank correlations were also considered on a voxel-wise basis across every case (Total Correlation, Table 4.4). Considering the Spearman's rank, rCBV had a statistically stronger correlation with ADAPT(1,1)-a1 than with IVIM-f for all ROIs considered. Between rCBV and ADAPT(1,1)- α1, Spearman's rank, s=0.471, 0.521, 0.419 and 0.649 and between rCBV and IVIM-f, s=0.397, 0.506, 0.395, 0.480 (P<0.001) across the whole brain and regions of grey matter, white matter and tumour respectively.

The voxel-wise parameter values were correlated for an axial slice from one of the cases and plotted in Figure 4.4. The strongest correlations were observed in GM; the correlations in the Tumour appeared to have the greatest variability. For the rCBV and IVIM-f correlations, the relationship is linear. For the rCBV and ADAPT(1,1)-α1 correlation, a non-linear relationship is observed.

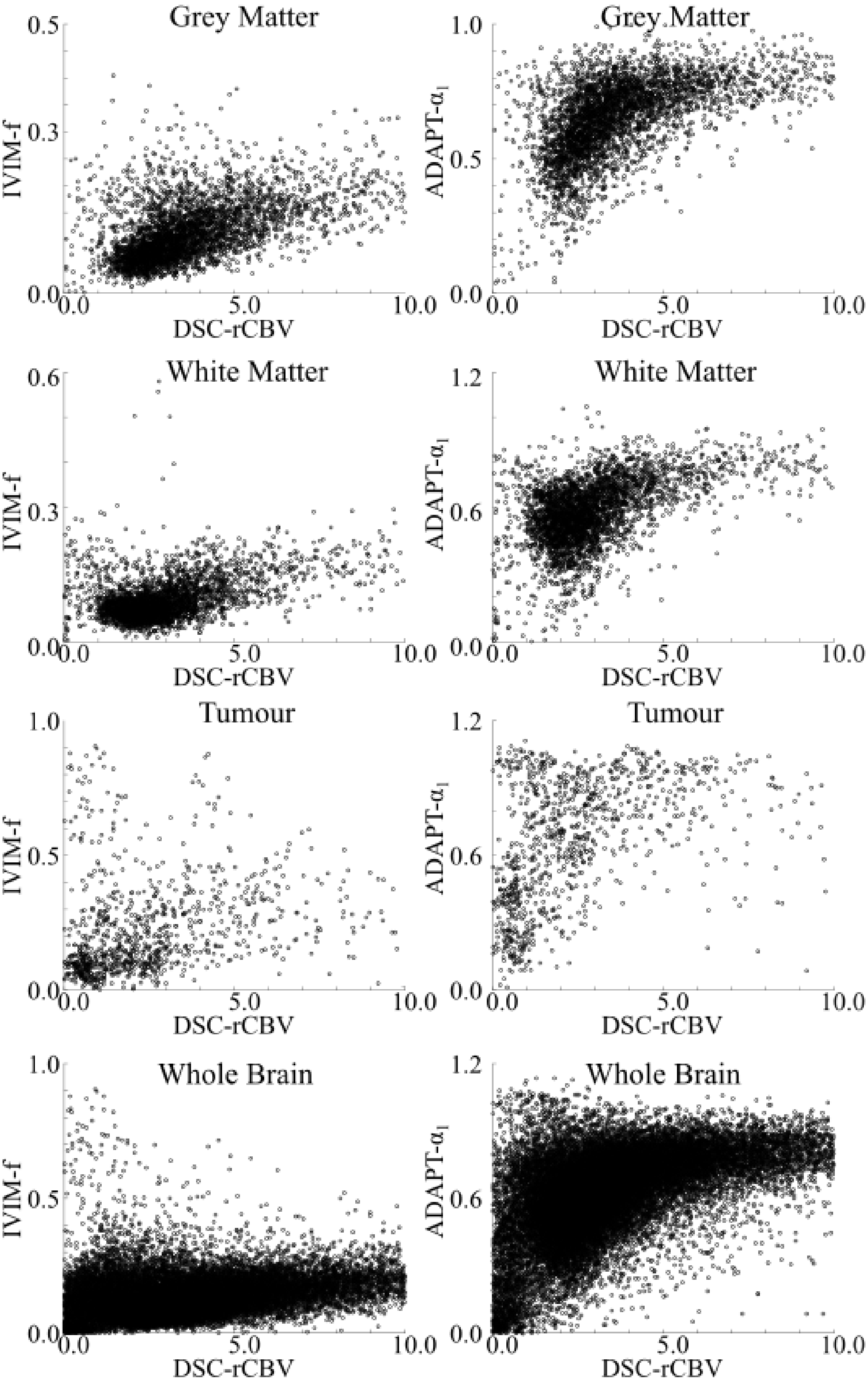

Figure 4.4: Parameter values for each voxel of an axial slice from a patient in the cohort. Correlations between (left) rCBV and IVIM-f and (right) rCBV and ADAPT(1,1)-α1. Correlations in regions of (top-bottom) Grey Matter, White Matter, Tumour and across the Whole Brain.

The parameter mean, median, and standard deviation for each tissue type, calculated across all voxels in the cohort, are presented in Table 4.4.

Table 4.4: Mean, Median and Standard Deviation of rCBV, IVIM-f, ADAPT(1,1)-α1 parameters for the cohort across different tissue regions on a voxel-wise basis.

	Grey Matter			White Matter			Tumour			Whole Brain		
	rCBV	IVIM-f	ADAPT-α_1	rCBV	IVIM-f	ADAPT-α_1	rCBV	IVIM-f	ADAPT-α_1	rCBV	IVIM-f	ADAPT-α_1
Mean	4.73	0.12	0.66	2.89	0.10	0.62	2.80	0.21	0.7	3.24	0.12	0.68
Median	3.76	0.10	0.68	2.61	0.08	0.63	2.44	0.14	0.71	3.03	0.1	0.69
Std Dev.	3.60	0.07	0.16	1.63	0.06	0.14	2.79	0.21	0.23	1.63	0.1	0.18

The rCBV parameter exhibits the greatest variability. rCBV measurements were respectively highest in GM. IVIM-f and ADAPT(1,1)-α1 measurements were higher in GM than WM but respectively highest in Tumour ROIs. For all parameters, variability was greatest in the Tumour ROIs.

4.3.2 Number of DWI Components and the Impact on Perfusion Measurements

The optimum ADAPT order was selected for each voxel, and thus the number of components in the diffusion signal determined (Figure 4.5). Most of the brain was determined to exhibit two-component behaviour; areas of one component behaviour were exhibited within the ventricles (Figure 4.5.b). Three-component behaviour was detected near the boundary of the ventricles (Figure 4.5.b and 4.5.d), indicating potential partial volume effects. Three-component behaviour was also exhibited within some tumour ROIs (Figure 4.5.f); this could also be due to partial volumes or potentially due to high perfusion in larger vessels.

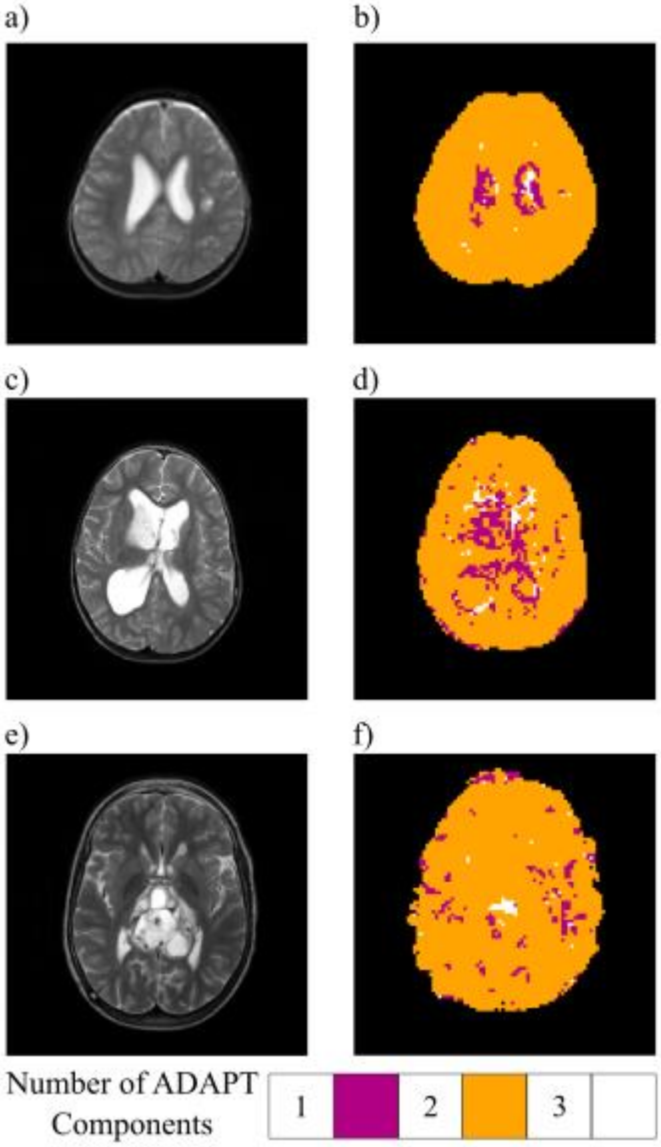

Figure 4.5: Example case of the ADAPT method applied to In-Vivo DWI axial slices. a) Axial b0 image, enlarged ventricles, b) ADAPT component map. c) Axial b0 image, enlarged ventricles and low perfused tumour, d) ADAPT component map, e) Axial b0 image, high perfused tumour, f) ADAPT component map.

The correlations were then performed voxel-wise within the regions identifying as one-, two- and three-component behaviour respectively. Spearman’s rank was then calculated for the average correlation across the whole cohort (Table 4.5).

Table 4.5: Average Spearman's Rank correlations between DWI measurements and rCBV for each case in the cohort considering the whole brain. One, Two and Three-component diffusion signals considered (determined with the ADAPT method) P < 0.001 for all measurements.

Spearman's Rank (s)				Zou's 95% CI				
Number of Components	rCBV IVIM-f	rCBV ADAPT-α1	IVIM-f ADAPT-α1	n	Fisher Z	Lower Bound	Upper Bound	Strongest Correlation
Whole Brain- Average								
1	0.133	0.239	0.840	1969	-8.49	-0.13	-0.08	ADAPT(1,1)-α1
2	0.457	0.505	0.890	30378	-20.87	-0.05	-0.04	ADAPT(1,1)-α1
3	0.380	0.511	0.860	467	-5.94	-0.18	-0.09	ADAPT(1,1)-α1

Regardless of the number of components detected, the correlation between rCBV and ADAPT(1,1)-α1 was statistically stronger than the correlation between rCBV and IVIM-f. Both correlations were moderate in regions that exhibited two components within the diffusion signal (rCBV and IVIM-f: s=0.457, rCBV and ADAPT(1,1)-α1: s=0.505, P<0.001). In regions of three-component behaviour, the correlation between rCBV and ADAPT(1,1)-α1 was comparable to the respective correlation in two components (rCBV and ADAPT(1,1)-α1: s=0.511, P<0.001) and the correlation between rCBV and IVIM-f was weaker (rCBV and IVIM-f: s=0.380, P<0.001). Both correlations were weakest in regions that exhibited one component behaviour (rCBV and IVIM-f: s=0.133, rCBV and ADAPT(1,1)-α1: s=0.239, P<0.001). The ratio of one-, two- and three-component voxels was 3:96:1 in GM, 4:94:1 in WM and 14:84:2 in tumours.

4.3.3 High Order ADAPT behaviour

For the voxels identified as exhibiting three-component behaviour, a higher-order ADAPT model, ADAPT(3,1), was fitted to the diffusion signal. The parameter ADAPT(3,1)-α1 was correlated against rCBV (s=0.641, P<0.001) demonstrating a stronger correlation than IVIM-f or ADAPT(1,1)-α1 against rCBV respectively (Table 4.5).

4.4 Discussion

Average correlations were statistically stronger between rCBV and ADAPT(1,1)-α1 than between rCBV and IVIM across the cohort. Both of these diffusion models are two component models. The ADAPT model makes no prior assumption about the diffusion signal and does not require multi-step fitting, a key factor that may contribute to the stronger correlation with rCBV.

A significant correlation was reported between rCBV and IVIM-f in the Tumour and GM ROI across the paediatric cohort. These results are in agreement with respective correlation studies in the adult population (18–21,23,25). A significant correlation was also found for the WM ROIs, not previously reported (25).

The Spearman's rank correlations between rCBV and ADAPT(1,1)-α1 were significantly stronger than the correlations between rCBV and IVIM-f for all tissue types considered across the cohort. It is evident that the correlation between rCBV and ADAPT(1,1)-α1 is non-linear (Figure 4.4). This is due to the ADAPT method fitting the logarithm of the diffusion signal, as this provides greater parameter stability (37). Pearson's r correlation coefficient would be unsuitable for investigating this non-linear correlation (38). A transformation could be applied to the ADAPT(1,1)-α1 data to ensure a linear correlation. However, given the properties of logarithms, if a linear summation of parameters is fitted to a logarithm of linear components, the relationship between the fitted parameters and original components cannot be recovered. Hence the transformation to ensure a linear correlation would be empirical. As the Spearman's rank correlation remains unchanged by any monotonic transformation (39), it is the recommended correlation coefficient to assess the correlations considered here.

The correlation of the diffusion parameters to rCBV was affected by the number of components detected in the diffusion signal. The correlation with voxels identifying one component behaviour was weakest. Theoretically, these voxels have no perfusion component, or a perfusion fraction too small to be currently detected. Hence, voxels with one component behaviour should be excluded from perfusion studies. The ADAPT method could be used to potentially identify voxels with such behaviour (29).

The correlations with voxels identifying two or three components were comparable for the ADAPT method. In voxels with three component behaviour, the parameter ADAPT(3,1)-$\alpha 1$ demonstrated an even stronger correlation with rCBV than ADAPT(1,1)-$\alpha 1$ or IVIM-f. The correlation between rCBV and IVIM-f in voxels with three components was comparatively weaker, highlighting another breakdown of the IVIM model's two-component assumption. This suggests that with more complex diffusion models, a better understanding of the perfusion behaviour could be attained. Three-component behaviour could, however, be caused by a multitude of reasons, such as partial volume effects (27)(40). Different ADAPT coefficients could potentially represent different flow regimes. Other ADAPT coefficients related to three-component behaviour should also be investigated. The correlations in tumour ROIs were moderate despite the heterogeneity. For the tumour correlations considered in each of the 15 cases, 6 cases were unable to determine which correlation was statistically stronger. This is likely due to the small size of the tumours and consequently small ROIs unable to provide the statistical power. With a larger cohort, the difference in correlations between low- and high-grade tumours could be investigated.

The mean IVIM-f parameter measurements were higher in GM (0.12 ± 0.07) than they were in WM (0.10 ± 0.06), in agreement with previous studies (25)(41). However, the parameter values were slightly higher than some of those previously reported in adult correlation studies, particularly for white matter (Wu et al. IVIM-$f_{GM}=0.14 \pm 0.02$, IVIM-$f_{WM}=0.07 \pm 0.01$(25), Grech-Sollars et al. IVIM-$f_{GM}=0.10 \pm 0.002$, IVIM-$f_{WM}=0.08 \pm 0.002$). This could be explained by the increase in perfusion reported in children compared to adults (42). The standard deviation of our results was higher, but this is likely due to considerably larger ROIs than other studies. In Tumour ROIs, the median IVIM-f was considerably higher than in healthy tissue (0.21±0.21). The high variance was likely due to tumour heterogeneity and the different tumour types included within the cohort. Within the tumour voxels, 14% were identified as exhibiting one component behaviour. As the IVIM equation is a bi-exponential model, the IVIM-f parameter could be wrongly estimated in these instances, further contributing to the high parameter variance. Although there are relatively twice as many three-component voxels in tumour ROIs compared to ROIs in healthy tissue, the overall number of three-component voxels is still comparatively small. This suggests that overestimation of IVIM-f is more likely caused by the one-component voxels instead of partial volume effects.

The mean rCBV parameter measurements were higher in GM (4.73±3.36 mL/100 mL) than WM (2.89±1.63 mL/100 mL). The grey matter values were comparable to those previously reported, but the measurements in white matter were considerably higher (Wu et al. IVIM-$rCBV_{GM}$=4.4±0.5 mL/100 mL, $rCBV_{WM}$=0.07±0.01 mL/100 mL (25)). The discrepancies and greater variation are most likely attributed to the age of the cohort and number of voxels considered, but also the different fitting methods implemented for DSC data (43). The rCBV tumour measurements had the greatest variation (2.30 ± 2.79 mL/100 mL) and is attributed to the heterogeneity of tumours and the different types considered within the cohort. There is a great range in the reported rCBV measurements for different tumour types (44).

4.5 Study Limitations

There are some limitations to the work presented in this chapter. The distribution of b-values in the DWI sequence could change the performance of the two diffusion models considered. For the GM and WM, the ROIs were not manually drawn. In previous studies, considerably smaller ROIs were manually drawn, resulting in a lower variance. The correlations were also enhanced by deliberately selecting voxels that exhibited high IVIM-f values (21). The application of such methods to this work could have further increased the correlations observed. Although DSC and DWI were acquired with the same image resolution, the sequential acquisition could result in patient movement between scans contributing to voxel mismatches. Fluctuations in noise could further affect the correlations.

As with any correlation analysis, a fundamental relationship cannot be proven by the results of a correlation study. Furthermore, the biophysical relationship between rCBV and the ADAPT parameters is unknown. ADAPT is based on the Auto-Regressive Moving Average model, which is considered atheoretical (45). However, the α1 parameter has been shown to relate to the decay rate of an exponentially decaying signal (46). For a DWI signal, increased perfusion will result in a fast signal decay rate. Although the relationship between the ADAPT parameters and the rCBV measurement is complex and non-linear in nature, ADAPT presents the opportunity for complex perfusion biomarkers to be obtained by making no prior assumptions about the DWI data.

4.6 Conclusion

The ADAPT coefficients have a greater correlation than the IVIM-f parameter with rCBV measured by DSC-MRI. The moderate correlations observed demonstrate that perfusion information can be obtained non-invasively through diffusion measurements. The ADAPT method makes no prior assumptions about the number of exponential components contributing to the data, which gives it an advantage over the IVIM fitting method, which inherently assumes two-component behaviour. Complex multi-component diffusion and perfusion information exists within the DWI signal. To probe and understand this rich information, a highly sensitive technique, such as ADAPT, should be implemented.

Chapter 5

The ADAPT Method for Parameter Selection

5. The ADAPT Method for Parameter Selection

In this chapter, the ADAPT method is reformulated, and the IVIM parameters are fully derived from the ADAPT coefficients. The ADAPT fitting method is compared to the multi-step, non-linear, least-square fitting algorithm commonly used to estimate the IVIM parameters, with a particular focus on the IVIM-D* parameter. Both fitting methods investigate simulated white matter and grey matter brain models, considering the accuracy, precision and bias for a range of Signal to Noise Ratio (SNR) levels. Once optimised, the performance of the fitting methods is investigated in In-Vivo data.

5.1 Introduction

The Intravoxel Incoherent Motion (IVIM) method requires multiple b-values to measure diffusion and perfusion-related properties of biological tissue. The IVIM equation is given as (Equation 5.1):

$$\frac{S_{(b)}}{S_{(0)}} = f \cdot exp^{-bD^*} + (1 - f) \cdot exp^{-bD} \qquad (5.1)$$

Where S(b)/S(0) is the signal intensity of the normalised signal for a particular b-value (a parameter that is changed by varying the diffusion sensitization of the MR sequence); IVIM- D is the diffusion coefficient; IVIM-D* is the pseudo-diffusion coefficient (related to the perfusion of blood in the capillary network); and IVIM-f is the volume fraction of incoherently flowing blood in the tissue describing the fraction of the signal arising from the vascular network (36).The IVIM method assumes the detected signal is comprised of two exponentially decaying compartments; with decay constants equal to IVIM- D and IVIM-D*. The effects of IVIM-D* are most evident in the acquired signal at the very low b-values ($b < 100$ s/mm^2) (102), as values of IVIM-D* are typically several orders of magnitude higher than IVIM-D

(37). The perfusion-related parameters IVIM-f and IVIM-D* have demonstrated clinical value in diagnosing diseased tissue, such as liver fibrosis (114) and deteriorating renal function in the kidneys (107), and in the grading of tumours (218). Correlations between IVIM-D* and the microvascular density in histology samples have also been reported (219).

Despite the additional perfusion-related information available with IVIM-D*, this parameter is not yet routinely calculated. Compared to the other IVIM parameters, IVIM-D* has the largest measurement error (111,120), high heterogeneity (111,220,221), poor reproducibility (45,191) and is difficult to evaluate (102). Consequently, several IVIM reproducibility studies have only considered IVIM-D and IVIM-f (191,222,223), or even questioned the clinical applicability of IVIM-D*, particularly in low perfused tissues such as the brain (191,220).

The estimation of IVIM-D* is dependent upon the diffusion-weighted MR sequence, the number of b-values and the fitting method implemented. Parameter estimation can be confounded by the inherent assumption of two tissue compartments in the IVIM model. For example, in regions that are cystic or ischemic with no perfusion compartment, IVIM-D* is not defined. In such a case, IVIM-D* can be incorrectly assigned the same value as IVIM-D (120). IVIM-f will then be estimated by any value between 0 and 1, evidently increasing parameter variability. If more than two-compartments are present, such as partial volume effects between brain tissue and cerebral spinal fluid (CSF), the high diffusion coefficient of CSF can be misinterpreted and be incorrectly measured in the IVIM-D* parameter. Other bulk flow phenomena, such as tubular flow or glandular secretion (128), may also contribute to the signal (102). Furthermore, the range of physiologically possible IVIM-D* values is much greater than for the other IVIM parameters, increasing the parameter variance (224).

For IVIM-D*, low perfused tissues have a higher measurement error due to the weakly bi-exponential signal (45). An increase in the number of b-values, sampling more of the low b-value regime, has been shown to increase parameter robustness (116). However, the b-value sequence implemented can influence parameter estimation, causing bias (117,225). To increase stability in the parameter estimations, IVIM is typically fitted using a constrained, Multi-Step approach. IVIM-D* is estimated via a nonlinear, least-squares fitting method, once IVIM-D and IVIM-f have been estimated (121,226). IVIM-D and IVIM-f are fitted using b-values above a selected threshold (typically b-values > 200 s/mm^2) at which the perfusion effects are considered negligible. However, this threshold is postulated to be tissue-dependent and will influence the estimation of IVIM-D* (37). Any errors in the fitting of IVIM-D and IVIM-f will propagate and increase the error in IVIM-D*. Compared to unconstrained fitting, the Multi-Step method reduces variability but consequently has a higher parameter bias. A range of different fitting methods for the IVIM parameters have been considered (45,125), but there is not yet a consensus on the best processing approach.

Hence there is a need to develop improved analysis methods for fitting DW-MRI data if the routine clinical use of IVIM-D* is to be attained. In this chapter, the Auto-Regressive Discrete Acquisition Points Transformation (ADAPT) method was implemented for the recovery of the IVIM parameters. The ADAPT method is based on a non-stationary, special case of the auto-regressive moving average model (227), a generalised multi-exponential model. ADAPT interprets the diffusion signals as a discrete function of acquisition points where the behaviour of the signal can be derived from the relationship between these acquisition points. ADAPT can represent a wide range of data sets and is not constrained to assume bi-exponential behaviour. ADAPT does not require any Multi-Step fitting processes, initial starting values, nor the oversampling of low b-values for robust parameter estimation (213).

The ability for ADAPT to correctly identify the number of components was established in a previous chapter (Chapter 3) and a strong correlation between the ADAPT coefficients and IVIM parameters confirmed. In previous chapters (Chapter 3 and Chapter 4), the ADAPT method was applied to a logged DWI signal. However, in this chapter the ADAPT method is applied to a normalised DWI signal with an offset of -1 (resulting in a signal value of 0 at b=0 s/mm^2), allowing the ADAPT coefficients to derive the IVIM parameters directly. The performance of the ADAPT fitting method is compared with the Multi-Step, non-linear, least-square fitting algorithm commonly used for IVIM parameter estimation.

5.2 Materials and Methods

5.2.1 The Auto-regressive Discrete Acquisition Points Transformation

The ADAPT method was modified to model the diffusion signal by the equation (Equation 5.2):

$$(S_n - 1) = \sum_{i=0}^{Q} \beta_i b_{n-i} + \sum_{j=1}^{P} \alpha_j \left(S_{n-j} - 1\right) \qquad (5.2)$$

Where S_n is the signal at acquisition point n, b_n is the b-value at acquisition point n, and α_j, β_i are the minimisation coefficients. Here the acquisition point of the b-values is used such that b value=0 s/mm^2 is at acquisition point 0. The subsequent b-value in the sequence would be acquisition point 1. At each acquisition point, the previously acquired b-values and signal values are used as previous input terms. Hence the signal at acquisition point n can be modelled by a linear summation of previous b-values and signal values. The parameters P and Q indicate the number of lag terms that the input signal depends upon. Upon selecting the order of the ADAPT(P,Q) model, the α and β minimisation coefficients are determined by minimising the normal equation. The ADAPT method uses the normalised diffusion signal, with an offset of -1 to ensure that that at acquisition point 0, the output, S_n-1, is 0. This is required so that for the first few data points, where the ADAPT order is greater than the acquisition points, a value of 0 can be substituted for cases where b_{n-i} or S_{n-j} don't exist. The α_j, β_i coefficients are established using the matrices in Equation 5.3:

$$S = \begin{bmatrix} b_{(0)} & 0 & \cdots & 0 & 0 & 0 & \cdots & 0 \\ b_{(1)} & b_{(0)} & \cdots & \vdots & \left(\frac{S_{(0)}}{S_{(0)}}\right) - 1 & 0 & \cdots & \vdots \\ \vdots & \vdots & \cdots & \vdots & \left(\frac{S_{(1)}}{S_{(0)}}\right) - 1 & \left(\frac{S_{(0)}}{S_{(0)}}\right) - 1 & \cdots & \vdots \\ \vdots & \vdots & \cdots & \vdots & \vdots & \vdots & \cdots & \vdots \\ b_{(N)} & b_{(N-1)} & \cdots & b_{(N-Q)} & \left(\frac{S_{(N-1)}}{S_{(0)}}\right) - 1 & \left(\frac{S_{(N-2)}}{S_{(0)}}\right) - 1 & \cdots & \left(\frac{S_{(N-P)}}{S_{(0)}}\right) - 1 \end{bmatrix};$$

$$A = \begin{bmatrix} \beta_0 \\ \vdots \\ \beta_Q \\ -\alpha_1 \\ \vdots \\ -\alpha_P \end{bmatrix}; \qquad S_{pred} = \begin{bmatrix} \left(\frac{S_{(0)}}{S_{(0)}}\right) - 1 \\ \left(\frac{S_{(1)}}{S_{(0)}}\right) - 1 \\ \vdots \\ \left(\frac{S_{(N)}}{S_{(0)}}\right) - 1 \end{bmatrix} \tag{5.3}$$

Where S is a matrix constructed from the b-values and the detected signal with acquisition point n=0, …, N. A is the matrix of ADAPT coefficients. S_{pred} is the final model of the normalised predicted signal. By finding the least-squares error of Equation 5.4, A is minimised, and the model S_{pred} is established:

$$S \cdot A = S_{pred} \tag{5.4}$$

5.2.1.1 Determining the Number of Components with ADAPT

Once the optimum ADAPT(P,Q) order has been selected, the number of components in the signal can be determined using the transfer function. The transfer function is given by dividing the signal output, (S_n-1), by the signal input, (b_n). Equation 5.2 can be rearranged as (Equation 5.5):

$$(S_n - 1) - \alpha_1(S_{n-1} - 1) - \cdots - \alpha_P(S_{n-P} - 1) = \beta_0 b_n + \beta_1 b_{n-1} + \cdots + \beta_Q b_{n-Q} \tag{5.5}$$

Using the Lag Operator, Equation 5.5 can be re-written as (Equation 5.6):

$$(S_n - 1)\left(1 - \alpha_1 \hat{L} - \cdots - \alpha_P \hat{L}^P\right) = b_n\left(\beta_0 + \beta_1 \hat{L} + \cdots + \beta_Q \hat{L}^Q\right) \tag{5.6}$$

Where $\hat{L}$ is the Lag Operator(181) such that $\hat{L}(S_n - 1) = (S_{n-1} - 1)$. Hence the transfer function, H(n), is written as (Equation 5.7):

$$H(n) = \frac{(S_n - 1)}{b_n} = \frac{\beta_0 + \beta_1 \hat{L} + \cdots + \beta_Q \hat{L}^Q}{1 - \alpha_1 \hat{L} - \cdots - \alpha_P \hat{L}^P} \tag{5.7}$$

By performing a Z-transform on the transfer function, converting the discrete signal to a ‘frequency’ domain representation, the number of components in the signal can be recovered (Equation 5.8):

$$H(z) = \frac{\beta_0 + \beta_1 z^{-1} + \cdots + \beta_Q z^{-Q}}{1 - \alpha_1 z^{-1} - \cdots - \alpha_P z^{-P}} \tag{5.8}$$

Providing P ≥ Q, finding the poles of the system, that is, the number of roots for the denominator of Equation 5.8 when equated to zero, yields the number of components. For example, ADAPT(2,2) gives (Equation 5.9):

$$(S_n - 1) = \alpha_1 (S_{n-1} - 1) + \alpha_2 (S_{n-2} - 1) + \beta_0 b_n + \beta_1 b_{n-1} + \beta_2 b_{n-2} \tag{5.9}$$

Taking the transfer function of ADAPT(2,2) and performing a Z-transform gives (Equation 5.10):

$$H(z) = \frac{\beta_0 + \beta_1 z^{-1} + \beta_2 z^{-2}}{1 - \alpha_1 z^{-1} - \alpha_2 z^{-2}} \tag{5.10}$$

Here the denominator is a quadratic expression with two roots. Consequently, ADAPT(2,2) is evaluated to be a two-component decay model. The number of components is determined by the Pth order of the optimum ADAPT(P,Q) model.

5.2.1.2 Deriving the IVIM parameters with ADAPT

The IVIM method models a bi-exponential diffusion signal (Equation 5.1). To derive the IVIM parameters from the ADAPT coefficients, the Z-transform for the sum of P exponentials is required. Equation 5.11, provides a generalised summation of P exponentials:

$$S[n] = \sum_{j=1}^{P} f_j \exp\left(-D_j b[n]\right) \tag{5.11}$$

Where S[n] is the measured signal at acquisition point n; P is the number of exponential terms; f_i indicates the amplitude of each exponential term; D_j is the decay constant, and b[n] gives the b-value at n. If the b-value sequence is linearly spaced with incremental gaps of Δb, then b[n] can be replaced with nΔb. This allows the summation in Equation 5.11 to be expressed as (Equation 5.12):

$$S[n] = \sum_{j=1}^{P} f_j r_j^n\,; \quad \text{where } r_j = \exp\left(-D_j \Delta b\right) \tag{5.12}$$

The Z-transform of Equation 5.12 is (Equation 5.13):

$$S[z] = \sum_{j=1}^{P} \frac{f_j}{1 - r_j z^{-j}} \tag{5.13}$$

By equating the denominators of the Z-transforms of the ADAPT equation (Equation 5.8) and the multi-exponential summation (Equation 5.13), such that (Equation 5.14):

$$1 - \sum_{j=1}^{P} \alpha_j z^{-j} = 1 - \sum_{j=1}^{P} r_j z^{-j} \tag{5.14}$$

It can be inferred that the poles, x_j, of Equation 5.8 will also be solutions to the denominator in Equation 5.14. That is (Equation 5.15)

$$x_j = \frac{1}{r_j} = \frac{1}{\exp\left(-D_j \Delta b\right)} \tag{5.15}$$

Hence the multi-exponential decay constants can be derived from the poles of the optimum ADAPT order (Equation 5.16):

$$D_j = \frac{\ln\left(x_j\right)}{\Delta b} \tag{5.16}$$

5.2.2 Data Simulations

All simulations and data analysis were conducted using MATLAB (MathWorks, Natick, MA, USA, v.2017b). Diffusion signals were simulated using the IVIM equation in Equation 5 .1. White Matter (WM) and Grey Matter (GM) models were simulated using IVIM parameters reported for volunteers in previous studies ($D_{WM}=0.77\times10^{-3}mm^2/s$; $D^*_{WM}=7.9\times10^{-3}mm^2/s$; $f_{WM}=0.07$; $D_{GM}=0.84\times10^{-3}mm^2/s$; $D^*_{GM}=8.2\times10^{-3}mm^2/s$; $f_{GM}=0.14$) (111). The ADAPT method requires linearly spaced b-values in order to derive the IVIM parameters. A series of clinically relevant, linearly spaced b-value sequences between 0 and 1000s/mm^2 were investigated with the number of b-values ranging between 7 and 16. Non-linearly spaced b-value sequences, optimised for IVIM, were also used for simulations, with a sequence of 11 exponentially spaced b-values [0, 20, 40, 80, 110, 140, 170, 200, 300, 500, 1000] and an optimised sequence of 16 b-values [0, 40, 50, 60, 150, 160, 170, 190, 200, 260, 440, 550, 600, 700, 980, 1000] considered. The 16 b-value sequence was proposed by Lemke et al. (45) for low perfused tissue and has been optimised using Monte Carlo simulations to minimise fit error.

5.2.3 Robustness Analysis

The robustness of the fitting methods was investigated with the addition of random white Gaussian noise to the simulations to mimic different levels of SNR. Although the noise in DWI is governed by a Rician distribution, it is well approximated by a Gaussian distribution for the SNR levels considered in this simulation (73). The lowest SNR level considered was 40, a typical value recorded for DWI measurements in previous studies (45)(121) and also in the In-Vivo case considered. SNR levels of 57, 69, 80, 89, 98, 106, 113 and 120 were also considered as these correspond to the SNR levels when the number of signal averages (NSAs) are linearly increased. When the NSA doubles, the SNR is increased by a factor of $\sqrt{2}$. The SNR level added to the diffusion signal was uniform across the b-values. The data simulations were performed using 1000 random data iterations for each model and SNR level.

5.2.4 In-Vivo Data Acquisition

To validate the performance of the fitting methods In-Vivo, a volunteer brain scan (age 26 years), was scanned on a Philips Achieva 3T TX (Philips Healthcare, Best, the Netherlands) MRI scanner at Birmingham Children’s Hospital using a 32-multichannel receiver head coil. Informed consent was obtained and the East Midlands – Derby Research Ethics Committee (REC 04/MRE04/41) approved the study operating under the rules of Declaration of Helsinki 1975 (and as revised in 1983). The diffusion-weighted MRI sequence used a sensitivity-encoded (SENSE) approach with single-shot, spin-echo (EPI) sequence and the following parameters: b-value data acquired in three orthogonal directions, FOV 230mm x 230mm, TR/TE 3214/84ms, matrix size 256x256, 5mm slice thickness and in-plane resolution 0.9mm x 0.9mm. A b-value sequence of 11 linearly spaced b-values between 0 and 1000 s/mm^2, [0, 100, 200, …, 1000] s/mm^2, was used. The scan duration of this protocol was 2.12 minutes.

The patient was scanned with the above protocol 8 successive times, with a dynamic scan, (duration 16.94 minutes) in order to assess the reproducibility of the IVIM parameters and to increase the signal to noise ratio (SNR) by averaging over the repeated measurements.

5.2.5 Data Analysis

A range of ADAPT orders from ADAPT(0,0) to ADAPT(3,3) were applied to the simulated diffusion signals with the optimum ADAPT order chosen by using the corrected Akaike Information Criterion (AICc) for model selection in finite data sets (173). The AICc, selects the optimum model by rewarding models for their goodness of fit and penalising for the number of parameters in the model. This penalty term discourages overfitting, and the model with the lowest AIC is deemed the optimum model (Equation 5.17):

$$AIC_c = n \cdot log\left(\frac{RSS}{n}\right) + \frac{2 \cdot k \cdot (k+1)}{n-k-1} \tag{5.17}$$

Where n is the number of b-values, RSS is the residual sum squared, and k is the number of model parameters. The diffusion signal, S_0 is included as a model parameter, and an additional parameter is counted due to the Gaussian noise hypothesis for signal residues. The optimum fit relative to the other considered models is justified by using Bayes Factors (193). The associated statistic, the log evidence ratio (LER) indicates the evidence for a competing model being the true optimum fit against that selected by the AICc. LER values greater than 0, 0.5, 1 and 2 indicate that a competing model has ‘minimal’, ‘substantial’, ‘strong’ or ‘decisive’ evidence that it is not the optimum fit.

The IVIM fitting method was assessed using non-linear least-square fitting, and a constrained one-parameter fitting method (121). This model assumes that the effects of perfusion are negligible in measurements at high b-values. For b-values > 200 s/mm^2, a monoexponential fitting method is implemented. By plotting the signal on a logarithmic scale and calculating the gradient and y-intercept, IVIM-D and IVIM-f can be calculated respectively. These parameters are given to Equation 5.1 and IVIM-D* is found using the with the Levenberg-Marquardt algorithm with the result bound between 0 and $5\times10^{-2}mm^2/s$ (219) This fitting method is henceforth referred to as the Multi-Step method.

The ADAPT method and Multi-Step method were fitted to the brain tissues models and also In-Vivo volunteer data. SNR levels for the In-Vivo measurements were calculated for the WM and GM using 5 4x4 pixel ROIs from each tissue type. The SNR of each ROI was calculated from the pixel-wise standard deviation across the multiple acquisitions (228). In-Vivo GM and WM masks were created using the Brain Extraction Tool (BET) (216) and the FMRIB's Automated Segmentation Tool (FAST) (217) from the FMRIB Software Library v6.0 (Analysis Group, Oxford, UK) using the T1-weighted images. A probability map was generated predicting whether a voxel was WM, GM or cerebrospinal fluid. WM and GM masks were created, using only voxels with a 100% probability of being that tissue type. To further mitigate the effects of partial volumes, an image erosion of 1 voxel was applied to each mask.

5.2.6 Statistical Analysis

To determine the optimal b-value sequence to implement with the ADAPT method, the simulated sequence that returned the lowest total relative error for the WM and GM models was selected. The relative error σ_x for parameter, x, is given by (Equation 5.18):

$$\sigma_x = \frac{\sqrt{\frac{1}{N}\sum_{i=1}^{N}(x_i - x)^2}}{x} \tag{5.18}$$

Where N is the number of iterations, x_i is the fitted parameter result for the ith iteration, and x is the true parameter value. The total relative error was found by summing the relative errors for each of the 3 IVIM parameters; $\sigma_{TOT}=\sigma_D+\sigma_{D*}+\sigma_f$.

For the model simulations, accuracy was assessed by comparing the mean parameter values measured by the fitting methods to their true values. The difference between the fitted parameter result and the true value was also measured using the relative bias, $\theta_{x.}$ for parameter x, the relative bias is given by (Equation 5.19):

$$\theta_x = \frac{\frac{1}{N}\sum_{i=1}^{N}(x_i - x)}{x} \tag{5.19}$$

Precision was assessed by calculating the coefficient of variation (CV) over the 1000 iterations measured. For all accuracy and bias measurements, significance tests were performed using Analysis of variance (ANOVA) and the Tukey post hoc analysis ($P < 0.05$).

For the In-Vivo data, the average IVIM-D* parameter and CV were calculated from the ROIs in the WM and GM and investigated for both fitting methods. To investigate the distribution of parameter values, histograms were computed from the WM (n=1327) and GM (n=2687) masks.

5.3 Results

5.3.1 ADAPT Method for Model Selection

A range of ADAPT orders were fitted to GM and WM models. The diffusion signals were simulated with a range of different SNR levels (Table 5.1).

Table 5.1: ADAPT Orders Fitted to White and Grey Matter Model Simulations

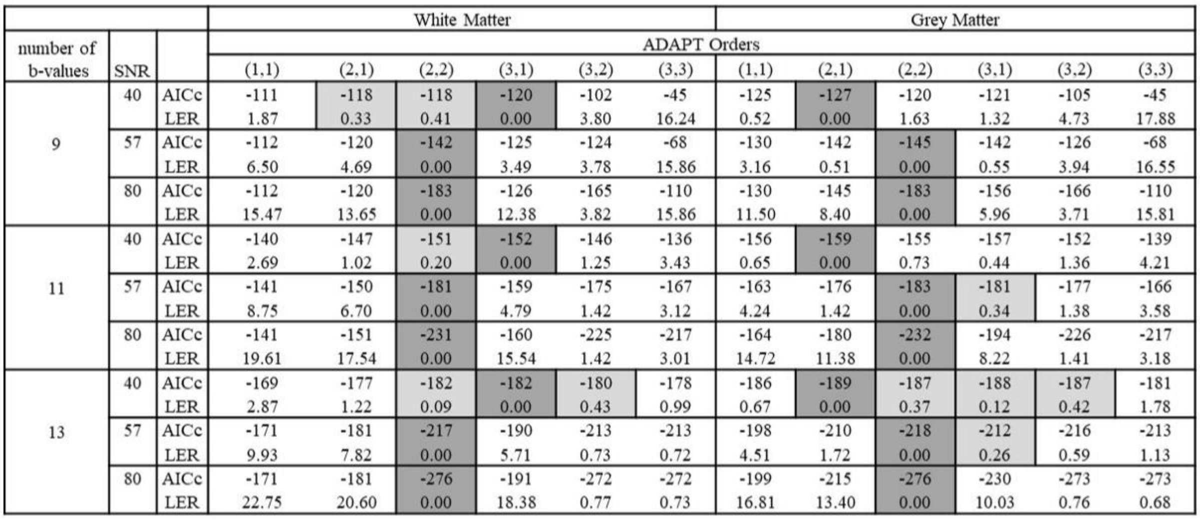

			White Matter						Grey Matter					
number of b-values	SNR		ADAPT Orders											
			(1,1)	(2,1)	(2,2)	(3,1)	(3,2)	(3,3)	(1,1)	(2,1)	(2,2)	(3,1)	(3,2)	(3,3)
9	40	AICc	-111	-118	-118	-120	-102	-45	-125	-127	-120	-121	-105	-45
		LER	1.87	0.33	0.41	0.00	3.80	16.24	0.52	0.00	1.63	1.32	4.73	17.88
	57	AICc	-112	-120	-142	-125	-124	-68	-130	-142	-145	-142	-126	-68
		LER	6.50	4.69	0.00	3.49	3.78	15.86	3.16	0.51	0.00	0.55	3.94	16.55
	80	AICc	-112	-120	-183	-126	-165	-110	-130	-145	-183	-156	-166	-110
		LER	15.47	13.65	0.00	12.38	3.82	15.86	11.50	8.40	0.00	5.96	3.71	15.81
11	40	AICc	-140	-147	-151	-152	-146	-136	-156	-159	-155	-157	-152	-139
		LER	2.69	1.02	0.20	0.00	1.25	3.43	0.65	0.00	0.73	0.44	1.36	4.21
	57	AICc	-141	-150	-181	-159	-175	-167	-163	-176	-183	-181	-177	-166
		LER	8.75	6.70	0.00	4.79	1.42	3.12	4.24	1.42	0.00	0.34	1.38	3.58
	80	AICc	-141	-151	-231	-160	-225	-217	-164	-180	-232	-194	-226	-217
		LER	19.61	17.54	0.00	15.54	1.42	3.01	14.72	11.38	0.00	8.22	1.41	3.18
13	40	AICc	-169	-177	-182	-182	-180	-178	-186	-189	-187	-188	-187	-181
		LER	2.87	1.22	0.09	0.00	0.43	0.99	0.67	0.00	0.37	0.12	0.42	1.78
	57	AICc	-171	-181	-217	-190	-213	-213	-198	-210	-218	-212	-216	-213
		LER	9.93	7.82	0.00	5.71	0.73	0.72	4.51	1.72	0.00	0.26	0.59	1.13
	80	AICc	-171	-181	-276	-191	-272	-272	-199	-215	-276	-230	-273	-273
		LER	22.75	20.60	0.00	18.38	0.77	0.73	16.81	13.40	0.00	10.03	0.76	0.68

Two component White Matter and Grey Matter diffusion models were investigated with a range of b-values and Signal to Noise Ratio (SNR) levels. The ADAPT method was applied to the bi-exponential signals and the optimum fit (highlighted in dark grey) was selected by choosing the method with the lowest AICc. Those ADAPT orders lightly shaded have an LER<0.5, indicating competing models.

The ADAPT method for model selection was found to be robust down to SNR≈57, with ADAPT(2,2), a two-component model determined to be the optimum fit. SNR≈40 was found to incorrectly determine the number of compartments in WM, which agrees with previous work(213). At SNR≈40, the GM simulations had ADAPT(2,1), also a two-component model, as their optimum fit. For WM simulations at SNR≈40, ADAPT(3,1), a three-component model, was found to be the optimum fit, indicating that noise was misinterpreted as an additional component. For SNR ≥ 80 no other orders competed with ADAPT(2,2) for either the WM or GM models with all LERs > 0.5. ADAPT orders (0,0), (1,0), (2,0), and (3,0) were also considered but had comparatively higher LER values. Sequences with 9, 11 and 13 b-values with SNR levels 40, 57, and 80 are shown in Table 5.1 and are indicative of the results found for other b-value sequences and SNR levels. Due to the model selection performance, simulations at SNR≈40 were not considered any further.

5.3.2 Optimum ADAPT sequence

The relative error for the IVIM-D* parameter and the total relative error was calculated for the WM and GM signals across the range of linearly spaced b-value sequences and SNR levels considered. The optimum number of b-values was found to be 11 for all SNR levels considered having the lowest total relative error and lowest relative error for the IVIM-D* parameter (Figure 5.1).

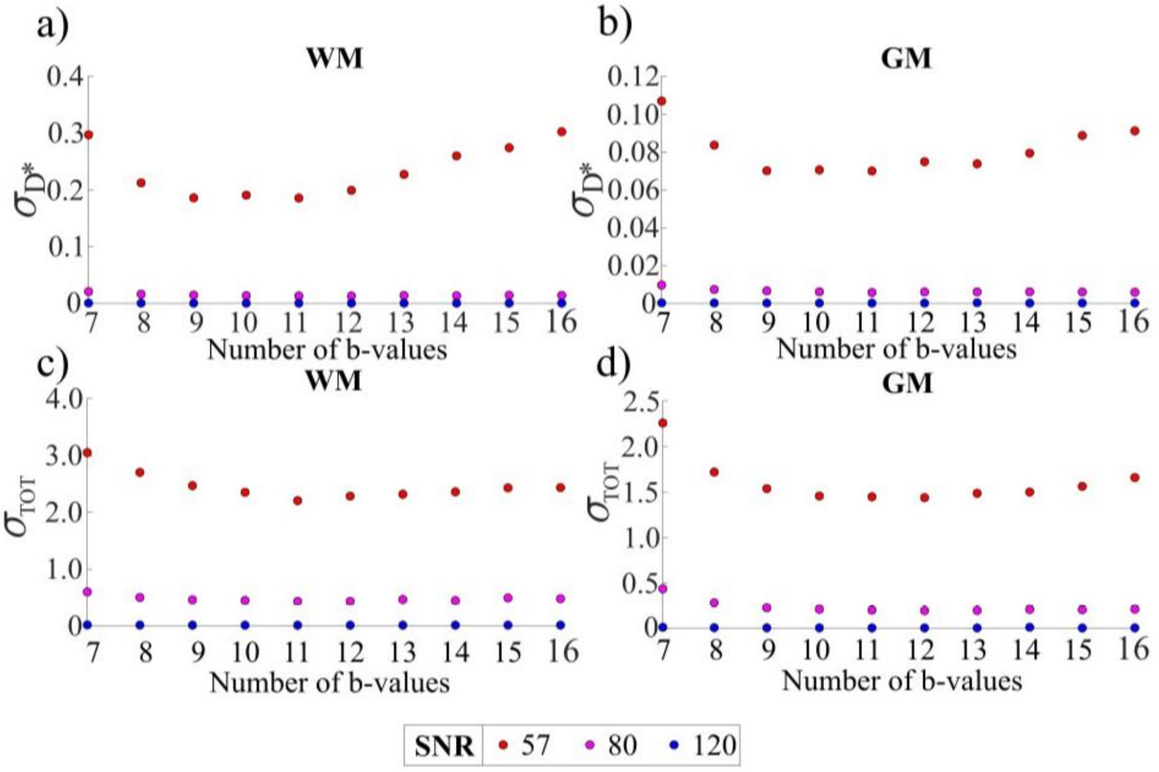

Figure 5.1: Relative error for the ADAPT method deriving the IVIM parameters as a function of the number of linearly spaced b-values in the signal. The relative error for the D* parameter in a) white matter, b) grey matter, Total relative error for all IVIM parameters in c) white matter, d) grey matter.

The optimum b-value sequence for ADAPT was [0, 100, 200, 300, 400, 500, 600, 700, 800, 900, 1000] s/mm^2. However, it can be noted that the ADAPT model is stable for the b-value sequences with 9 to 13 equally spaced b-values. In WM, at SNR≈57, σ_{TOT} was minimised with an 11 b-values sequence, σ_{TOT}=2.206. However, σ_{TOT} was comparable for 10 and 12 b-value sequences with σ_{TOT} = 2.351 and 2.285, respectively. At even higher SNR levels the minima found at 11 b-values was negligible; in WM, at SNR≈120, σ_{TOT} =0.013, 0.012 and 0.013 for 10, 11, and 12 b-value sequences respectively.

5.3.3 Model Data Simulations

5.3.3.1 Parameter Variability

The WM and GM simulation results for estimating IVIM-D, IVIM-D* and IVIM-f with the ADAPT method for an 11 b-value sequence linearly spaced are compared to the parameter results derived by the Multi-Step method with the 11 b-values linearly spaced, 11 b-values exponentially spaced, and 16 b-values optimised sequences (Figure 5.2.)

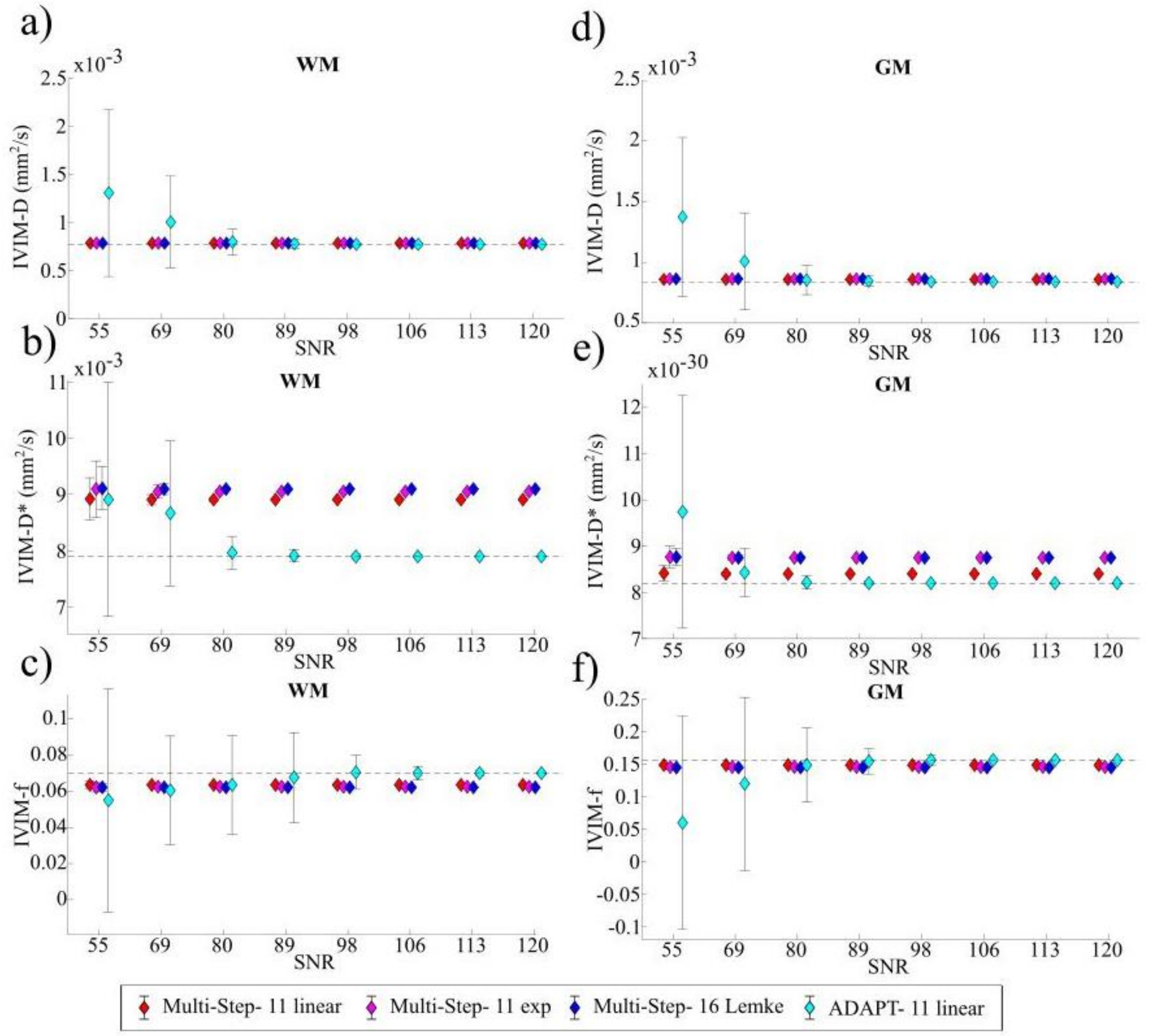

Figure 5.2: Accuracy results for the estimated IVIM parameters from the data simulations using the different fitting methods. WM models: a) IVIM-D, b) IVIM-D* c)IVIM-f. GM models: d) IVIM-D, e) IVIM-D* f)IVIM-f. The dashed lines represent the true IVIM parameter values, and the error bars the standard deviation for the 1000 iterations.

At high SNR levels, the ADAPT method provided more accurate IVIM parameters, in relation to the parameter averages of the 1000 iterations. This is most notable for IVIM-D* where ADAPT is the most accurate fitting method for WM with SNR ≥ 69, and GM with SNR ≥ 80. For IVIM-D, ADAPT becomes the most accurate fitting for WM with SNR ≥ 106 and GM with SNR ≥ 98, For IVIM-f, ADAPT becomes the most accurate at SNR ≥ 106 for

WM and SNR ≥ 98 for GM. The error bars for all IVIM parameters derived by the ADAPT method were, however larger in comparison to those obtained by the Multi-Step method.

For all IVIM parameters, the measurements obtained by the ADAPT method compared to all those obtained by the Multi-Step method (and various distributions of b-values considered) were significantly different (ANOVA $P<0.001$) with the ADAPT estimations closest to the ground truth values (Tukey $P<0.05$). This was across both the WM and GM models and all SNR levels considered with the only exception being IVIM-f in WM at SNR ≈ 69 and 80.

With the Multi-Step Method, comparing the IVIM parameter measurements obtained with the different distributions of b-values, there was no significant difference in IVIM-D or IVIM-f ($P > 0.05$) for SNR ≈ 57, 69 and 80 for either the WM or GM models. IVIM-D* had a significant difference across all SNR levels ($P < 0.05$) and all IVIM parameter measurements were significantly different ($P< 0.05$) for SNR ≥ 113.

The CV for all IVIM parameters fitted by the Multi-Step method for the three distributions of b-values considered were < 10% for the WM and GM models at SNR ≥ 57. As the Multi-Step method is typically fitted using an exponentially spaced sequence, the results for the CV, relative error and relative bias are shown using both the 11-linearly and 11-exponentially spaced b-value sequences in the figures below. However, the 11-linearly spaced method has a lower relative error and relative bias for both the WM and GM across all SNR levels considered. Consequently, only the results from the 11 linearly spaced b-value distribution are discussed any further.

The CV for all IVIM parameters was greater when fitted with the ADAPT method than with the Multi-Step method (Figure 5.3) but an acceptable CV of <10% can be achieved in most situations.

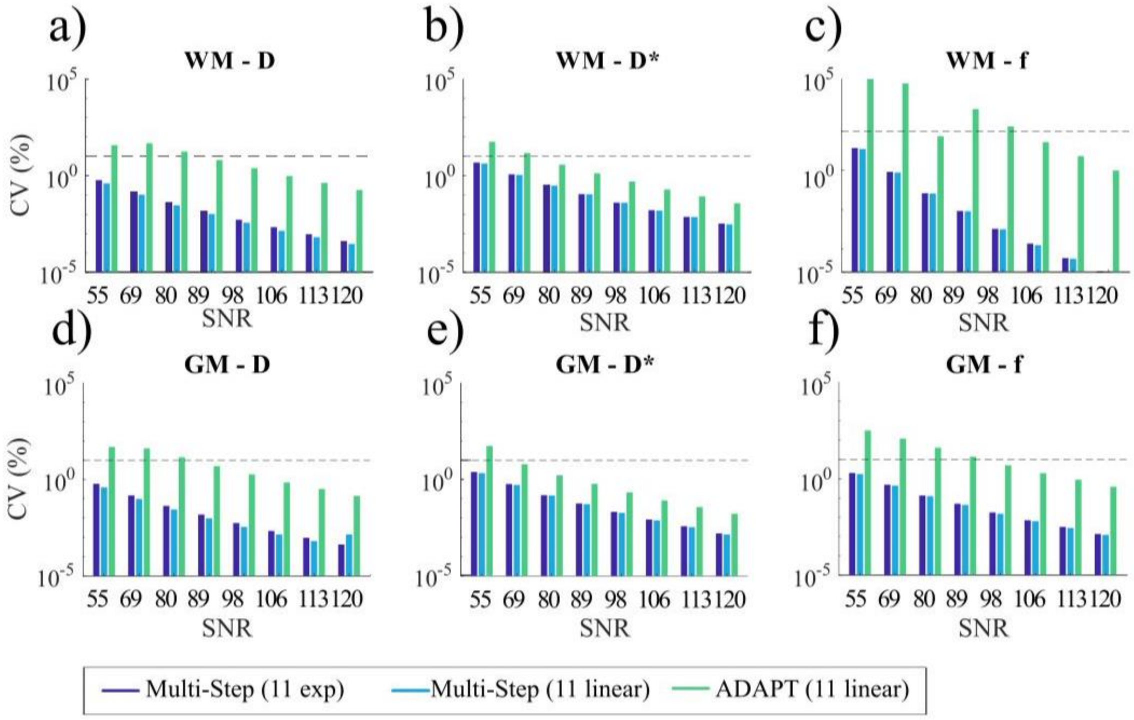

Figure 5.3: Coefficient of Variation (%) calculated for the fitting of the IVIM parameters with the ADAPT method and the multi-step fitting method for 11 equally spaced linear b-values. WM models: a) IVIM-D, b) IVIM-D*, c) IVIM-f. GM models: d) IVIM-D, e) IVIM-D*, f) IVIM-f. The dashed lines represent a CV=10%.

Although the parameter CVs are greater for the ADAPT fitting method, the CV is <10% for the WM in IVIM-D, IVIM-D* and IVIM-f at SNR ≥89, 80, 106, and in GM, SNR ≥ 89, 69, 98 respectively. The relative error was calculated for each of the IVIM parameters along with a summation for the total relative error (Figure. 5.4). (σ values in Table 5.2)

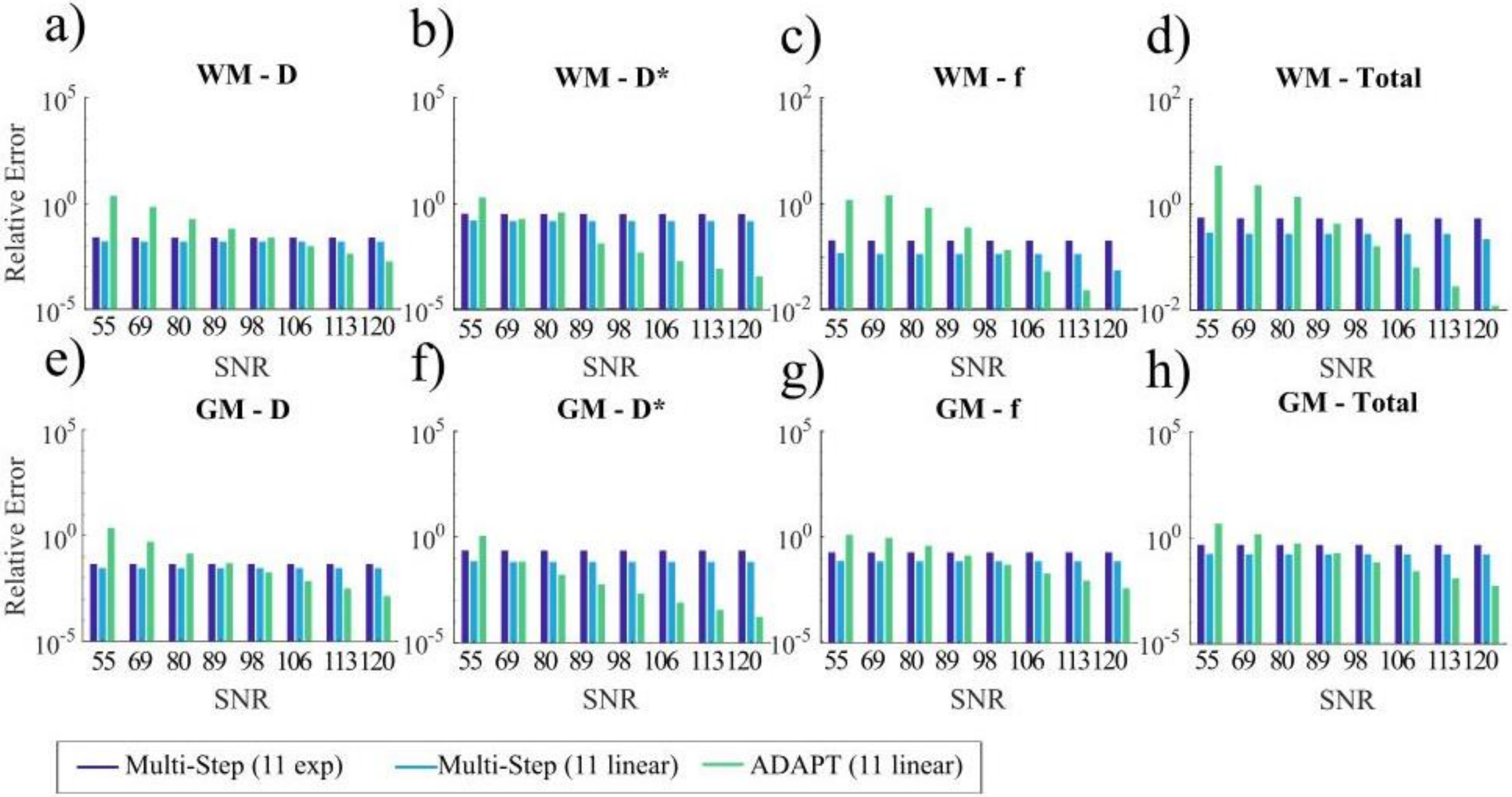

Figure 5.4: Relative Error calculated for the fitting of the IVIM parameters with the ADAPT method and the Multi-Step fitting method for 11 equally spaced linear b-values. WM models: a) IVIM-D, b) IVIM-D*, c)IVIM-f, d) Total.GM models: e) IVIM-D, f) IVIM-D*, g)IVIM-f, h) Total.

Table 5.2: Relative Error (± standard deviation) of IVIM parameters from White Matter and Grey Matter brain models fitted with the Multi-Step and ADAPT fitting method

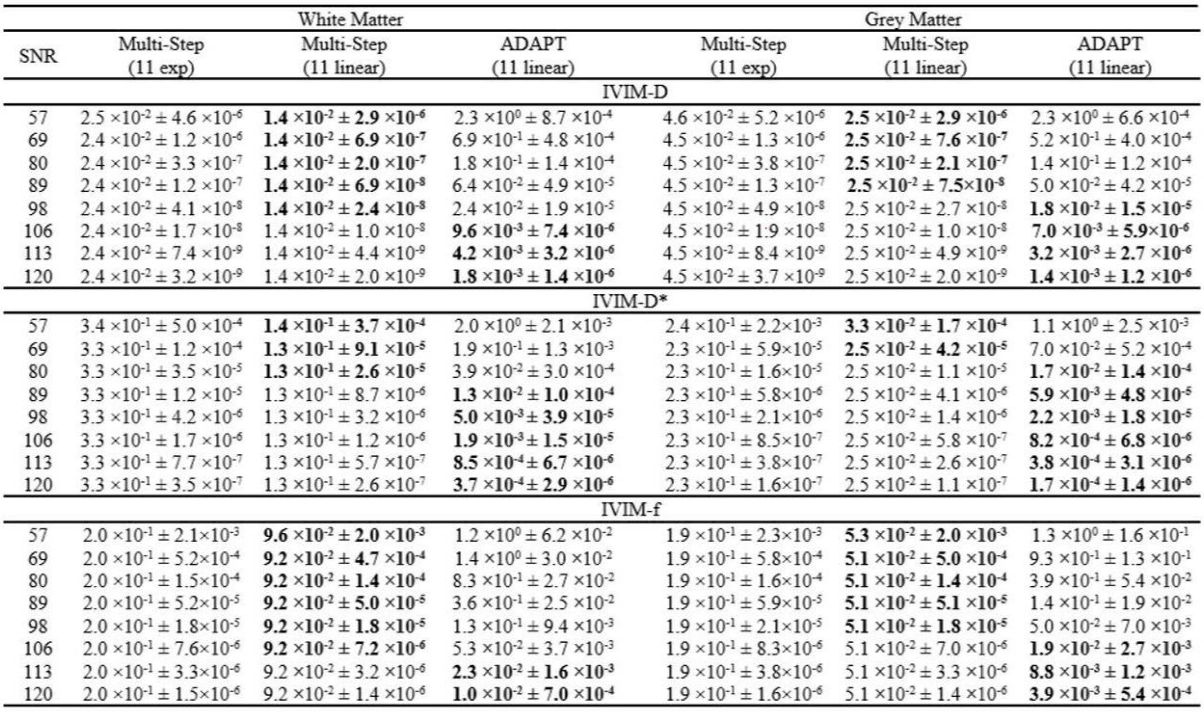

	White Matter			Grey Matter		
SNR	Multi-Step (11 exp)	Multi-Step (11 linear)	ADAPT (11 linear)	Multi-Step (11 exp)	Multi-Step (11 linear)	ADAPT (11 linear)
			IVIM-D			
57	$2.5 \times 10^{-2} \pm 4.6 \times 10^{-6}$	**$1.4 \times 10^{-2} \pm 2.9 \times 10^{-6}$**	$2.3 \times 10^{0} \pm 8.7 \times 10^{-4}$	$4.6 \times 10^{-2} \pm 5.2 \times 10^{-6}$	**$2.5 \times 10^{-2} \pm 2.9 \times 10^{-6}$**	$2.3 \times 10^{0} \pm 6.6 \times 10^{-4}$
69	$2.4 \times 10^{-2} \pm 1.2 \times 10^{-6}$	**$1.4 \times 10^{-2} \pm 6.9 \times 10^{-7}$**	$6.9 \times 10^{-1} \pm 4.8 \times 10^{-4}$	$4.5 \times 10^{-2} \pm 1.3 \times 10^{-6}$	**$2.5 \times 10^{-2} \pm 7.6 \times 10^{-7}$**	$5.2 \times 10^{-1} \pm 4.0 \times 10^{-4}$
80	$2.4 \times 10^{-2} \pm 3.3 \times 10^{-7}$	**$1.4 \times 10^{-2} \pm 2.0 \times 10^{-7}$**	$1.8 \times 10^{-1} \pm 1.4 \times 10^{-4}$	$4.5 \times 10^{-2} \pm 3.8 \times 10^{-7}$	**$2.5 \times 10^{-2} \pm 2.1 \times 10^{-7}$**	$1.4 \times 10^{-1} \pm 1.2 \times 10^{-4}$
89	$2.4 \times 10^{-2} \pm 1.2 \times 10^{-7}$	**$1.4 \times 10^{-2} \pm 6.9 \times 10^{-8}$**	$6.4 \times 10^{-2} \pm 4.9 \times 10^{-5}$	$4.5 \times 10^{-2} \pm 1.3 \times 10^{-7}$	**$2.5 \times 10^{-2} \pm 7.5 \times 10^{-8}$**	$5.0 \times 10^{-2} \pm 4.2 \times 10^{-5}$
98	$2.4 \times 10^{-2} \pm 4.1 \times 10^{-8}$	**$1.4 \times 10^{-2} \pm 2.4 \times 10^{-8}$**	$2.4 \times 10^{-2} \pm 1.9 \times 10^{-5}$	$4.5 \times 10^{-2} \pm 4.9 \times 10^{-8}$	$2.5 \times 10^{-2} \pm 2.7 \times 10^{-8}$	**$1.8 \times 10^{-2} \pm 1.5 \times 10^{-5}$**
106	$2.4 \times 10^{-2} \pm 1.7 \times 10^{-8}$	$1.4 \times 10^{-2} \pm 1.0 \times 10^{-8}$	**$9.6 \times 10^{-3} \pm 7.4 \times 10^{-6}$**	$4.5 \times 10^{-2} \pm 1.9 \times 10^{-8}$	$2.5 \times 10^{-2} \pm 1.0 \times 10^{-8}$	**$7.0 \times 10^{-3} \pm 5.9 \times 10^{-6}$**
113	$2.4 \times 10^{-2} \pm 7.4 \times 10^{-9}$	$1.4 \times 10^{-2} \pm 4.4 \times 10^{-9}$	**$4.2 \times 10^{-3} \pm 3.2 \times 10^{-6}$**	$4.5 \times 10^{-2} \pm 8.4 \times 10^{-9}$	$2.5 \times 10^{-2} \pm 4.9 \times 10^{-9}$	**$3.2 \times 10^{-3} \pm 2.7 \times 10^{-6}$**
120	$2.4 \times 10^{-2} \pm 3.2 \times 10^{-9}$	$1.4 \times 10^{-2} \pm 2.0 \times 10^{-9}$	**$1.8 \times 10^{-3} \pm 1.4 \times 10^{-6}$**	$4.5 \times 10^{-2} \pm 3.7 \times 10^{-9}$	$2.5 \times 10^{-2} \pm 2.0 \times 10^{-9}$	**$1.4 \times 10^{-3} \pm 1.2 \times 10^{-6}$**
			IVIM-D*			
57	$3.4 \times 10^{-1} \pm 5.0 \times 10^{-4}$	**$1.4 \times 10^{-1} \pm 3.7 \times 10^{-4}$**	$2.0 \times 10^{0} \pm 2.1 \times 10^{-3}$	$2.4 \times 10^{-1} \pm 2.2 \times 10^{-3}$	**$3.3 \times 10^{-2} \pm 1.7 \times 10^{-4}$**	$1.1 \times 10^{0} \pm 2.5 \times 10^{-3}$
69	$3.3 \times 10^{-1} \pm 1.2 \times 10^{-4}$	**$1.3 \times 10^{-1} \pm 9.1 \times 10^{-5}$**	$1.9 \times 10^{-1} \pm 1.3 \times 10^{-3}$	$2.3 \times 10^{-1} \pm 5.9 \times 10^{-5}$	**$2.5 \times 10^{-2} \pm 4.2 \times 10^{-5}$**	$7.0 \times 10^{-2} \pm 5.2 \times 10^{-4}$
80	$3.3 \times 10^{-1} \pm 3.5 \times 10^{-5}$	**$1.3 \times 10^{-1} \pm 2.6 \times 10^{-5}$**	$3.9 \times 10^{-2} \pm 3.0 \times 10^{-4}$	$2.3 \times 10^{-1} \pm 1.6 \times 10^{-5}$	$2.5 \times 10^{-2} \pm 1.1 \times 10^{-5}$	**$1.7 \times 10^{-2} \pm 1.4 \times 10^{-4}$**
89	$3.3 \times 10^{-1} \pm 1.2 \times 10^{-5}$	$1.3 \times 10^{-1} \pm 8.7 \times 10^{-6}$	**$1.3 \times 10^{-2} \pm 1.0 \times 10^{-4}$**	$2.3 \times 10^{-1} \pm 5.8 \times 10^{-6}$	$2.5 \times 10^{-2} \pm 4.1 \times 10^{-6}$	**$5.9 \times 10^{-3} \pm 4.8 \times 10^{-5}$**
98	$3.3 \times 10^{-1} \pm 4.2 \times 10^{-6}$	$1.3 \times 10^{-1} \pm 3.2 \times 10^{-6}$	**$5.0 \times 10^{-3} \pm 3.9 \times 10^{-5}$**	$2.3 \times 10^{-1} \pm 2.1 \times 10^{-6}$	$2.5 \times 10^{-2} \pm 1.4 \times 10^{-6}$	**$2.2 \times 10^{-3} \pm 1.8 \times 10^{-5}$**
106	$3.3 \times 10^{-1} \pm 1.7 \times 10^{-6}$	$1.3 \times 10^{-1} \pm 1.2 \times 10^{-6}$	**$1.9 \times 10^{-3} \pm 1.5 \times 10^{-5}$**	$2.3 \times 10^{-1} \pm 8.5 \times 10^{-7}$	$2.5 \times 10^{-2} \pm 5.8 \times 10^{-7}$	**$8.2 \times 10^{-4} \pm 6.8 \times 10^{-6}$**
113	$3.3 \times 10^{-1} \pm 7.7 \times 10^{-7}$	$1.3 \times 10^{-1} \pm 5.7 \times 10^{-7}$	**$8.5 \times 10^{-4} \pm 6.7 \times 10^{-6}$**	$2.3 \times 10^{-1} \pm 3.8 \times 10^{-7}$	$2.5 \times 10^{-2} \pm 2.6 \times 10^{-7}$	**$3.8 \times 10^{-4} \pm 3.1 \times 10^{-6}$**
120	$3.3 \times 10^{-1} \pm 3.5 \times 10^{-7}$	$1.3 \times 10^{-1} \pm 2.6 \times 10^{-7}$	**$3.7 \times 10^{-4} \pm 2.9 \times 10^{-6}$**	$2.3 \times 10^{-1} \pm 1.6 \times 10^{-7}$	$2.5 \times 10^{-2} \pm 1.1 \times 10^{-7}$	**$1.7 \times 10^{-4} \pm 1.4 \times 10^{-6}$**
			IVIM-f			
57	$2.0 \times 10^{-1} \pm 2.1 \times 10^{-3}$	**$9.6 \times 10^{-2} \pm 2.0 \times 10^{-3}$**	$1.2 \times 10^{0} \pm 6.2 \times 10^{-2}$	$1.9 \times 10^{-1} \pm 2.3 \times 10^{-3}$	**$5.3 \times 10^{-2} \pm 2.0 \times 10^{-3}$**	$1.3 \times 10^{0} \pm 1.6 \times 10^{-1}$
69	$2.0 \times 10^{-1} \pm 5.2 \times 10^{-4}$	**$9.2 \times 10^{-2} \pm 4.7 \times 10^{-4}$**	$1.4 \times 10^{0} \pm 3.0 \times 10^{-2}$	$1.9 \times 10^{-1} \pm 5.8 \times 10^{-4}$	**$5.1 \times 10^{-2} \pm 5.0 \times 10^{-4}$**	$9.3 \times 10^{-1} \pm 1.3 \times 10^{-1}$
80	$2.0 \times 10^{-1} \pm 1.5 \times 10^{-4}$	**$9.2 \times 10^{-2} \pm 1.4 \times 10^{-4}$**	$8.3 \times 10^{-1} \pm 2.7 \times 10^{-2}$	$1.9 \times 10^{-1} \pm 1.6 \times 10^{-4}$	**$5.1 \times 10^{-2} \pm 1.4 \times 10^{-4}$**	$3.9 \times 10^{-1} \pm 5.4 \times 10^{-2}$
89	$2.0 \times 10^{-1} \pm 5.2 \times 10^{-5}$	**$9.2 \times 10^{-2} \pm 5.0 \times 10^{-5}$**	$3.6 \times 10^{-1} \pm 2.5 \times 10^{-2}$	$1.9 \times 10^{-1} \pm 5.9 \times 10^{-5}$	**$5.1 \times 10^{-2} \pm 5.1 \times 10^{-5}$**	$1.4 \times 10^{-1} \pm 1.9 \times 10^{-2}$
98	$2.0 \times 10^{-1} \pm 1.8 \times 10^{-5}$	**$9.2 \times 10^{-2} \pm 1.8 \times 10^{-5}$**	$1.3 \times 10^{-1} \pm 9.4 \times 10^{-3}$	$1.9 \times 10^{-1} \pm 2.1 \times 10^{-5}$	**$5.1 \times 10^{-2} \pm 1.8 \times 10^{-5}$**	$5.0 \times 10^{-2} \pm 7.0 \times 10^{-3}$
106	$2.0 \times 10^{-1} \pm 7.6 \times 10^{-6}$	**$9.2 \times 10^{-2} \pm 7.2 \times 10^{-6}$**	$5.3 \times 10^{-2} \pm 3.7 \times 10^{-3}$	$1.9 \times 10^{-1} \pm 8.3 \times 10^{-6}$	$5.1 \times 10^{-2} \pm 7.0 \times 10^{-6}$	**$1.9 \times 10^{-2} \pm 2.7 \times 10^{-3}$**
113	$2.0 \times 10^{-1} \pm 3.3 \times 10^{-6}$	$9.2 \times 10^{-2} \pm 3.2 \times 10^{-6}$	**$2.3 \times 10^{-2} \pm 1.6 \times 10^{-3}$**	$1.9 \times 10^{-1} \pm 3.8 \times 10^{-6}$	$5.1 \times 10^{-2} \pm 3.3 \times 10^{-6}$	**$8.8 \times 10^{-3} \pm 1.2 \times 10^{-3}$**
120	$2.0 \times 10^{-1} \pm 1.5 \times 10^{-6}$	$9.2 \times 10^{-2} \pm 1.4 \times 10^{-6}$	**$1.0 \times 10^{-2} \pm 7.0 \times 10^{-4}$**	$1.9 \times 10^{-1} \pm 1.6 \times 10^{-6}$	$5.1 \times 10^{-2} \pm 1.4 \times 10^{-6}$	**$3.9 \times 10^{-3} \pm 5.4 \times 10^{-4}$**

For SNR≈57, the relative error in the IVIM-parameters for both the WM and GM models is at least an order of magnitude greater with the ADAPT model than with the Multi-Step method. However, as the SNR level increases, ADAPT begins to outperform the Multi-Step method. The performance is most notable for the IVIM-D* parameter. By SNR≈69, the relative error in the WM is comparable; σ_{D*}=0.128, 0.189 for the Multi-Step method and the ADAPT fitting method respectively.

For SNR≈89, σ_{D*} is considerably smaller for the ADAPT fitting method in the WM model; σ_{D*}=0.127, 0.013 for the Multi-Step method and the ADAPT fitting method respectively. As the SNR level increases, the relative error for the Multi-Step method plateaus while the relative error for the ADAPT fitting methods continues to decrease; i.e. at SNR≈120 in the WM model, σ_{D*}=0.1271, 0.0004 for the Multi-Step and ADAPT fitting method respectively. In the GM model, ADAPT has a smaller σ_{D*} from SNR≈80. The ADAPT method gives a smaller relative error for the other IVIM parameters at high SNR levels: from SNR≈106 and SNR≈98 for the IVIM-D parameter in the WM and GM respectively; from SNR≈113 and SNR≈106 for the IVIM-f parameter in the WM and GM. By SNR≈98, the total relative error in both the WM and GM is smallest when parameters are fitted using the ADAPT method instead of the Multi-Step method.

5.3.3.2 Parameter Bias

The relative bias results for the IVIM parameters in the WM and GM tissue models are presented in Figure 5.5. In general, the relative bias was positive for IVIM-D and IVIM-D* and negative for IVIM-f. For the IVIM parameters fitted by the Multi-Step method, the relative bias in each of the parameters appeared unchanged across the range of SNR levels considered. Higher biases were apparent in the perfusion related parameters, IVIM-D* and IVIM-f for the WM model, a lower perfused model compared to the GM. Conversely, the relative bias of the parameters derived by the ADAPT method were varied across the SNR levels considered, with the relative bias decreasing by orders of magnitude as the SNR increased.

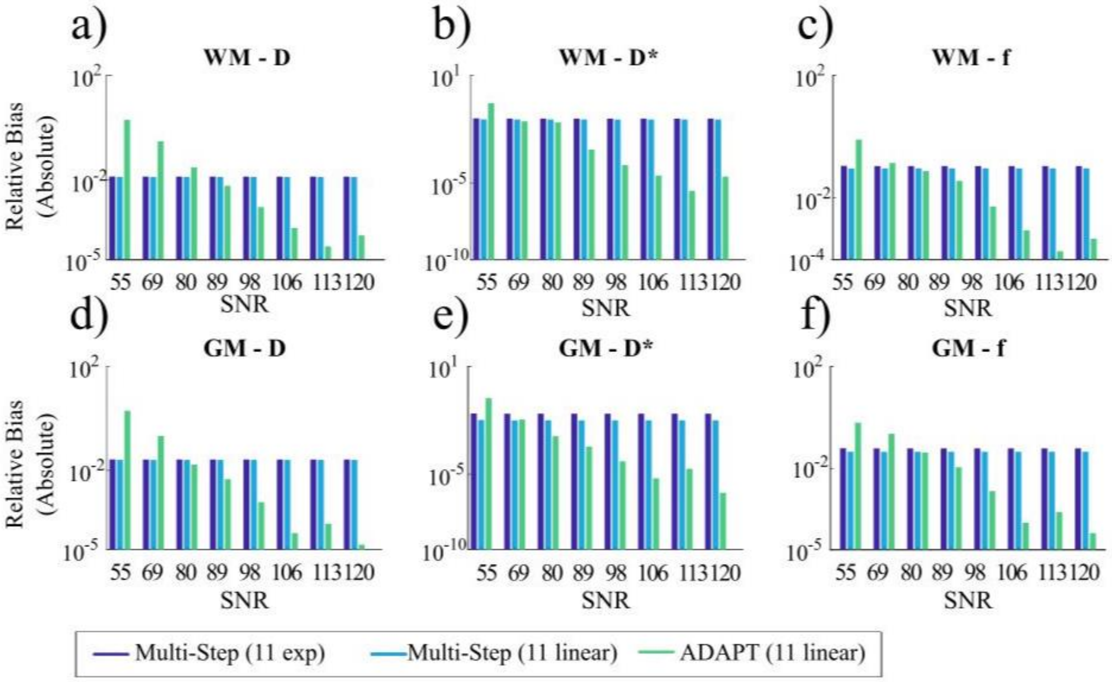

Figure 5.5: Relative Bias (absolute values) calculated for the fitting of the IVIM parameters with the ADAPT method and the Multi-Step fitting method for 11 equally spaced linear b-values. WM model: a) IVIM-D, b) IVIM-D*, c)IVIM-f. GM model: d) IVIM-D, e) IVIM-D*,f)IVIM-f.

For the WM model, θ_{D*} >10% (SNR≈120, θ_{D*}=12.71 ± 0.003%). From SNR≈80, the ADAPT method outperforms the Multi-Step method in the WM model, with θ_{D*}=0.80 ± 0.04% compared to θ_{D*}=12.73 ± 0.32%. The same trend was observed for θ_{D*} in the GM (Table 5.3).

In the WM, ADAPT has a lower relative bias from SNR≈89, 69, 89, for the IVIM-D, IVIM-D* and IVIM-f parameters, respectively. For the GM the threshold is at SNR≈80 for all three parameters. For the 11 exponentially spaced b-values, in WM, at SNR≈120, θ_{D*}=32.54 ± 0.004%). The relative bias for IVIM-D* in WM was also investigated using the unconstrained fitting method (where all IVIM parameters are simultaneously fitted); at SNR≈120, θ_{D*}=6.05 ± 0.00024% and θ_{D*}=7.15 ± 0.0028% with 11 exponentially and 11 linearly spaced b-values respectively.

Table 5.3: Relative Bias (%) of IVIM parameters

	IVIM-D			IVIM-D*			IVIM-f		
	Multi-Step (11 exp)	Multi-Step (11 linear)	ADAPT (11 linear)	Multi-Step (11 exp)	Multi-Step (11 linear)	ADAPT (11 linear)	Multi-Step (11 exp)	Multi-Step (11 linear)	ADAPT (11 linear)
White Matter									
57	2.44 ± 0.60	**1.38 ± 0.37**	199.80 ± 11.32	33.23 ± 6.33	12.93 ± 4.74	143.22 ± 13.70	-20.09 ± 2.99	**-9.13 ± 2.92**	-78.86 ± 8.81
69	2.43 ± 0.15	**1.37 ± 0.09**	30.54 ± 0.62	32.53 ± 1.54	12.72 ± 1.15	9.65 ± 1.63	-20.03 ± 0.74	**-9.19 ± 0.67**	-13.74 ± 0.88
80	2.43 ± 0.04	**1.37 ± 0.03**	3.18 ± 0.18	32.52 ± 0.44	12.73 ± 0.32	0.80 ± 0.04	-20.02 ± 0.21	**-9.21 ± 0.20**	-9.91 ± 0.83
89	2.43 ± 0.02	1.37 ± 0.01	**0.63 ± 0.06**	32.54 ± 0.15	12.72 ± 0.11	0.14 ± 0.01	-20.03 ± 0.07	-9.21 ± 0.07	**-3.61 ± 0.35**
98	2.43 ± 0.01	1.37 ± 0.003	**-0.10 ± 0.02**	32.54 ± 0.05	12.71 ± 0.04	-0.01 ± 0.005	-20.03 ± 0.03	-9.21 ± 0.03	**0.54 ± 0.13**
106	2.43 ± 0.002	1.37 ± 0.001	**0.02 ± 0.01**	32.54 ± 0.02	12.71 ± 0.02	0.003 ± 0.002	-20.03 ± 0.01	-9.21 ± 0.01	**-0.09 ± 0.05**
113	2.43 ± 0.001	1.37 ± 0.001	**-0.003 ± 0.004**	32.54 ± 0.01	12.71 ± 0.01	0.0003 ± 0.001	-20.03 ± 0.005	-9.21 ± 0.005	**0.02 ± 0.02**
120	2.43 ± 0.0004	1.37 ± 0.0003	**-0.01 ± 0.002**	32.54 ± 0.004	12.71 ± 0.003	-0.003 ± 0.0004	-20.03 ± 0.002	-9.21 ± 0.002	**0.05 ± 0.01**
Grey Matter									
57	4.53 ± 0.62	**2.52 ± 0.34**	182.64 ± 13.75	23.45 ± 3.02	**2.61 ± 2.03**	67.65 ± 91.68	-16.34 ± 1.66	**-5.11 ± 1.43**	-64.78 ± 11.08
69	4.53 ± 0.16	**2.50 ± 0.09**	20.02 ± 0.52	23.34 ± 0.71	2.49 ± 0.52	**2.80 ± 0.64**	-16.36 ± 0.41	**-5.07 ± 0.36**	-24.38 ± 0.90
80	4.53 ± 0.05	2.51 ± 0.02	**1.67 ± 0.14**	23.32 ± 0.19	2.50 ± 0.14	**0.23 ± 0.02**	-16.36 ± 0.11	-5.09 ± 0.10	**-4.79 ± 0.39**
89	4.53 ± 0.02	2.51 ± 0.01	**0.47 ± 0.05**	23.31 ± 0.07	2.50 ± 0.05	**0.05 ± 0.006**	-16.36 ± 0.04	-5.09 ± 0.04	**-1.32 ± 0.14**
98	4.53 ± 0.01	2.51 ± 0.003	**-0.06 ± 0.02**	23.31 ± 0.03	2.50 ± 0.02	**-0.01 ± 0.002**	-16.36 ± 0.01	-5.09 ± 0.01	**0.17 ± 0.05**
106	4.53 ± 0.002	2.51 ± 0.001	**-0.004 ± 0.01**	23.31 ± 0.01	2.50 ± 0.007	**0.0004 ± 0.001**	-16.36 ± 0.01	-5.09 ± 0.005	**0.01 ± 0.02**
113	4.53 ± 0.001	2.51 ± 0.001	**-0.01 ± 0.003**	23.31 ± 0.005	2.50 ± 0.003	**-0.002 ± 0.0004**	-16.36 ± 0.003	-5.09 ± 0.002	**0.03 ± 0.01**
120	4.53 ± 0.0004	2.51 ± 0.0003	**0.002 ± 0.001**	23.31 ± 0.002	2.50 ± 0.001	**0.00005 ± 0.0002**	-16.36 ± 0.001	-5.09 ± 0.001	**-0.004 ± 0.004**

5.3.4 In-Vivo Data Analysis

For the In-Vivo data, averaged over 8 acquisitions, the SNR at b-value=1000s/mm^2 was found to be 122.8±27.9 in the WM ROIs and 138.1±18.9 in the GM. The IVIM-D* parameter maps, calculated with the ADAPT and Multi-Step fitting methods for an axial slice, are presented in Figure 5.6.

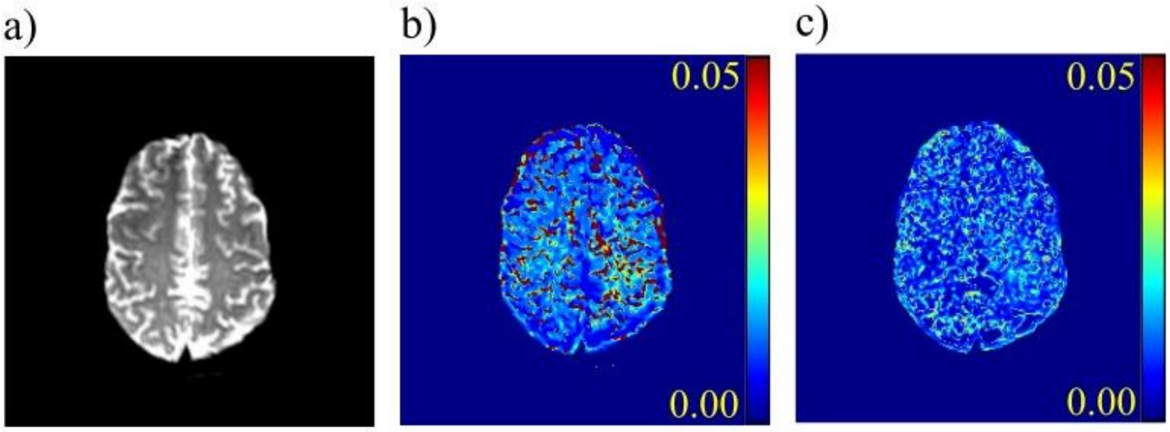

Figure 5.6: a)DWI axial volunteer slice where b=0 s/mm^2, averaged over 8 acquisitions. b)IVIM-D* parameter map calculated using the multi-step method. C) IVIM-D* parameter map calculated using the ADAPT method.

In the WM, the average IVIM-D* value was reported as $D^*_{WM}=7.7\times10^{-3} \pm 5.7\times10^{-4}$ mm^2/s, CV=7.33% and $D^*_{GM}=10.3\times10^{-3} \pm 5.6\times10^{-4}$ mm^2/s, CV=5.43% for the ADAPT and the Multi-Step methods respectively. In the GM, $D^*_{GM}=9.2\times10^{-3}\pm 5.2\times10^{-4}$ mm^2/s, CV=5.70%

and $D^*_{WM}=9.8\times10^{-3}\pm 5.4\times10^{-4}$ mm²/s, CV=5.55% for the ADAPT and the Multi-Step methods. The WM and GM histograms are presented in Figure 5.7.

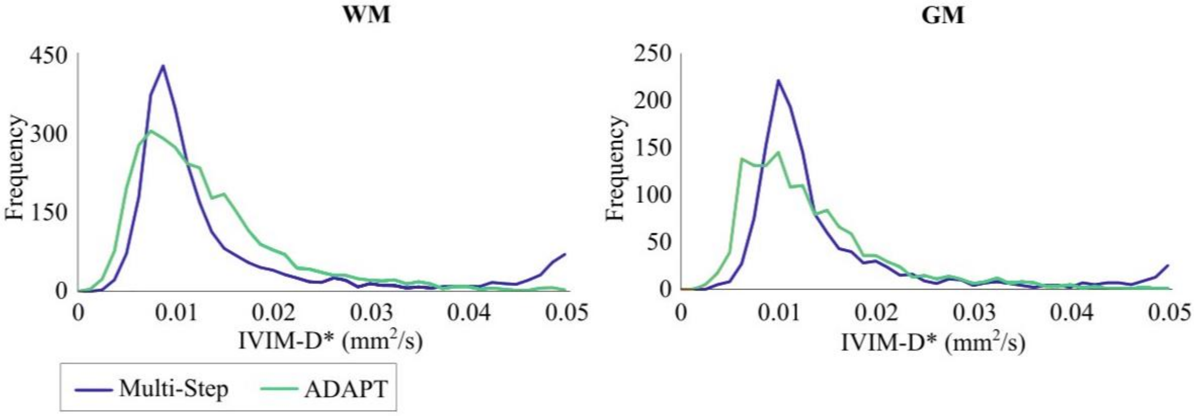

Figure 5.7: Histograms of IVIM-D* for In-Vivo data fitted with the multi-step and ADAPT fitting methods. White Matter region of interest (n=2687) and Grey Matter region of interest (n=1327).

The ADAPT method exhibited a broader histogram curve, implying greater variance in measuring IVIM-D*, in comparison to the Multi-Step method. The histogram peaks were at higher IVIM-D* values for the multi-step method in both the WM and GM.

5.4 Discussion

At high SNR levels, the ADAPT method is the superior fitting method, with a lower relative error and relative bias for each of the IVIM parameters considered. With the Multi-Step method, relative bias does not improve with increasing SNR levels and is incapable of yielding an accurate IVIM-D* in most situations. The bias in the estimated parameter values is strongly related to the b-value distribution (116). This is most evident in the IVIM-D* parameter. With the multi-step method, low perfused tissues require oversampling of the diffusion signal in the 'low b-value' regime ($b < 200s/mm^2$) (102)(104) in order to detect the subtle behaviour. Consequently, this oversampling means that any non-linear b-value sequence will bias the parameter fitting, as observed with the 11 exponentially spaced b-value sequence.

The Multi-Step method had a strong negative bias on all the IVIM-f values indicating that this method under fits the IVIM-f parameter and consequently overestimates the IVIM-D* parameter. The relative bias for IVIM-D* is greatest in the WM model, as this has a lower perfusion than the GM model. Even at SNR≈120, the bias of the Multi-Step method is >10% (12.71 ± 0.13%) in the WM model. The relative bias of the unconstrained fitting method was also greater than in the ADAPT method.

The ADAPT fitting method was successfully implemented for the In-Vivo case, with a small CV(<10%) observed in the WM and GM. Although the parameter bias couldn't be measured, as the ground truth is unknown, the trends are the same as those observed in the simulations. The average IVIM-D* value is greater with the Multi-Step method, and the histograms have peaks at higher IVIM-D* for the Multi-Step fitting method, supporting the observation that the Multi-Step method overestimates IVIM-D*.

It is recommended that providing the SNR level is sufficiently high (SNR ≥ 80) the ADAPT method should be used for recovery of the IVIM-D* parameter. However, an even higher SNR level is required for the stable recovery of the IVIM-D and IVIM-f parameters with the ADAPT method (SNR ≥ 98). As many IVIM studies don’t consider IVIM-D*, if IVIM-D and IVIM-f are the only two parameters of interest, then the Multi-Step method should be implemented. For IVIM-D and IVIM-f, the Multi-Step method is robust from SNR≈40 with the CV and relative bias <10%.

5.5 Study Limitations

Although the ADAPT method can attain a greater precision and accuracy, the time taken to achieve such a high SNR could be challenging in a clinical setting. If such a high SNR level is not feasible to attain, then a hybrid method for parameter recovery could be possible. At $SNR \geq 80$, using the equally spaced b-value sequence, the ADAPT method could be used to attain IVIM-D*. The same diffusion signal could then be fitted with the Multi-Step method to estimate IVIM-f and IVIM-D. As the ADAPT method makes no prior assumptions about the diffusion signal nor requires Multi-Step fitting procedures, it is a much faster fitting algorithm (213).

It may be seen as a limitation that the ADAPT method requires the b-values to be equally spaced. This is a b-value sequence unlikely to be used in current IVIM protocols. However, non-linearly spaced b-value sequences are currently required due to the poor fitting of IVIM-D*. The Multi-Step method requires the oversampling of the perfusion regime and is thus intrinsically biased. The ADAPT method requires a substantially higher SNR level than the Multi-Step method for parameter estimation, highlighting the general limitations of parameter estimation from noisy data. Regardless of the number of b-values or model used, no fitting method can truly give accurate and precise parameters with noisy data (229).

Other IVIM fitting methods should also be compared to the ADAPT method. i.e. Bayesian probability methods (125,230). Bayesian analysis doesn’t require initial parameter estimations. However, the implementation of such a method can be computationally intensive and parameter estimations greatly influenced by the prior information specified. Additionally, the low variability observed in parameter estimations may be at the expense of masking features in heterogeneous tissue (231).

The ADAPT method should be further developed to optimise fitting data with low SNR levels. The effects of denoising algorithms (232) should also be explored for the potential to avoid long acquisition times. The inclusion of an additional parameter or compartment to model the noise should also be considered.

5.6 Conclusion

At high SNR levels, the ADAPT method can successfully derive the IVIM parameters from the diffusion signal without making any prior assumptions about the nature of the data. The ADAPT method can estimate IVIM-D* with an acceptable relative bias and more accuracy than currently implemented fitting methods, which inherently provide biased values of this parameter.

Chapter 6

Conclusions and Future Work

6. Conclusions and Future Work

6.1 General Overview

The Auto-regressive Discrete Acquisition Points Transformation (ADAPT) method was developed for the estimation of multicomponent diffusion and perfusion behaviour within biological systems. The ADAPT method demonstrated that it could correctly identify the number of multiexponential components within the diffusion signal. This is something that cannot be achieved by applying multi-exponential fitting methods and selecting the optimum fit. This is an essential technique as the number of components within the diffusion signal greatly affects parameter estimations and consequently, the interpretation of the data. The coefficients of the ADAPT method also demonstrated a significant correlation with the Intravoxel Incoherent Motion (IVIM) parameters and the Dynamic Susceptibility Contrast (DSC) derived cerebral blood volume, highlighting a non-invasive method to obtain perfusion information. The ADAPT method and respective coefficients could be used to fully interpret the diffusion and perfusion measurements.

Alternatively, the diffusion signal could instead be interpreted though multiexponential decay constants via a reformulation of the ADAPT method. Providing the b-values in the diffusion sequence are equally spaced, the IVIM parameters can be mathematically derived from the ADAPT coefficients. The ADAPT method can estimate the IVIM parameters with lower bias and more accuracy than currently implemented fitting methods, which inherently provide biased values of the parameters. This is of particular significance for the perfusion IVIM-D* parameter which is not yet routinely calculated due to poor measurement errors with current fitting methods. The technical validation of the ADAPT method, both in component detection and parameter estimation, demonstrated that such techniques were robust and could be implemented with In-Vivo data, but highlighted the need for a sufficiently high signal to noise ratio and spatial resolution within the data. In this thesis, it has been demonstrated that multi b-value DWI data contains complex diffusion and perfusion information. With more advanced, sensitive techniques, such as the ADAPT method, this information can be probed further and establish a deeper understanding of tissue structure and behaviour.

Final conclusions and suggestions for the direction of future studies are presented below:

6.2 Final Conclusions

1. The ADAPT method demonstrated the ability to robustly fit a variable number of components and identify voxels exhibiting partial volume effects. IVIM parameter estimation is confounded in regions of partial volume effects, resulting in the thresholding of diffusion data in and around the ventricles. Hence the ADAPT method could be used to recover useful diffusion and perfusion related parameters from information that would otherwise be discarded. Technical validation demonstrated that the identification of the components was robust.
2. The ADAPT coefficients were shown to correlate with the perfusion measurement Dynamic Susceptibility Contrast- relative Cerebral Blood Volume (rCBV). The correlation was statistically stronger than the correlation between IVIM-f and rCBV. As DWI is a non-invasive method, this work highlighted a bolus free method for obtaining perfusion information. The performance of ADAPT also demonstrated that the fitting method used for interpreting the diffusion signal could greatly impact the correlation performance.
3. The ADAPT method was reformulated to enable the derivation of the IVIM model parameters from the ADAPT coefficients. The ADAPT fitting method was compared to the Multi-Step fitting method commonly used for IVIM parameter estimation. Considering the technical validations required for a quantitative imaging biomarker, the IVIM parameter accuracy and bias was lower with the ADAPT method. These results demonstrate that the ADAPT method was demonstrated to accurately measure IVIM-D* at high signal to noise ratio (SNR) levels. Unlike the Multi-Step method, the ADAPT method attained an acceptable relative bias for the IVIM-D* parameter. Providing the

SNR is sufficiently high (SNR ≥ 80); the ADAPT method should be used for the recovery of the IVIM-D* parameter.

6.3 Limitations and Future Works

1. The physical meaning of the ADAPT coefficients requires further investigations. Although the IVIM parameters can be mathematically derived from the ADAPT coefficients, error propagation will result in the IVIM parameters being less robust than the ADAPT coefficients. Hence the biophysical meaning of each of the ADAPT coefficient should be established in order to allow their direct interpretation. This should be explored through a range of studies, including establishing relationships with other perfusion biomarkers and further investigating computational models. A physical flow phantom should also be considered for validating perfusion measurements.
2. The ADAPT method should be further developed to optimise fitting data with lower SNR levels. In particular, the effects of denoising algorithms in combination with ADAPT should be explored for the potential to avoid long acquisition times. Selection of the optimum denoising algorithm is non-trivial and would require a considerable investigation. The inclusion of an additional component or parameter to account for noise should also be considered in future developments of the ADAPT method.
3. The ADAPT method for IVIM parameter extraction requires a linearly spaced b-value sequence for estimation of the IVIM parameters. This is a b-value sequence unlikely to be used in current IVIM protocols. However, current fitting methods require the oversampling of the low b-values in order to measure the effects of perfusion and are consequently intrinsically biased. ADAPT provides a method for robust component detection and parameter estimation, making no prior assumptions about the nature of the data.
4. With technical advancements, higher quality diffusion data can be attained, and the parameters from more complex multiexponential equations could be investigated. The

feasibility and robustness of parameters relating to a tri-exponential model should be explored. The ADAPT method should also be used to explore anisotropic effects with Diffusion Tensor Imaging (DTI). Such a study would require extensive considerations for the number of b-values and number of directions to include in the protocol. The ADAPT method would require reformulation and further interpretation of the resulting optimum ADAPT order. The trade-off between SNR and scan duration would also need to be considered. Although applications to DTI signals require extensive work, such work would enable anisotropic effects such as fanning or crossings of axon bundles to be explored. Further simulations and In-Vivo studies should be investigated.

The work in this thesis highlights the pitfalls of the assumptions and biases made by current multi b-value diffusion fitting methods. A new fitting method was investigated to address these pitfalls and evaluated. ADAPT could potentially obtain complex diffusion and perfusion biomarkers. Rich multicomponent information is present in the DWI signal. In order to extract this complex tissue behaviour, the ADAPT method is recommended for the fitting of multi b-value DWI data.

References

1. Kalaria RN, Akinyemi R, Ihara M. Stroke injury, cognitive impairment and vascular dementia. Biochim Biophys Acta - Mol Basis Dis. 2016;

2. Wilne SH, Ferris RC, Nathwani A, Kennedy CR. The presenting features of brain tumours: A review of 200 cases. Archives of Disease in Childhood. 2006.

3. Ssenyonga PK, Le Feuvre D, Taylor A. Head and neck neurovascular trauma: Clinical and angiographic correlation. Interv Neuroradiol. 2015;

4. Kalapurakal JA. Radiation therapy in the management of pediatric craniopharyngiomas - A review. Child's Nervous System. 2005.

5. Arai K, Lok J, Guo S, Hayakawa K, Xing C, Lo EH. Cellular mechanisms of neurovascular damage and repair after stroke. J Child Neurol. 2011;

6. Pak RW, Hadjiabadi DH, Senarathna J, Agarwal S, Thakor N V., Pillai JJ, et al. Implications of neurovascular uncoupling in functional magnetic resonance imaging (fMRI) of brain tumors. Journal of Cerebral Blood Flow and Metabolism. 2017.

7. Nelson AR, Sweeney MD, Sagare AP, Zlokovic B V. Neurovascular dysfunction and neurodegeneration in dementia and Alzheimer's disease. Biochim Biophys Acta - Mol Basis Dis. 2016;

8. Saver JL, Smith EE, Fonarow GC, Reeves MJ, Zhao X, Olson DM, et al. The "Golden Hour" and Acute Brain Ischemia. Stroke. 2010;

9. Zhou J, Li N, Yang G, Zhu Y. Vascular patterns of brain tumors. International Journal of Surgical Pathology. 2011.

10. Covarrubias DJ. Dynamic Magnetic Resonance Perfusion Imaging of Brain Tumors. Oncologist. 2004;

11. Wintermark M, Sesay M, Barbier E, Borbély K, Dillon WP, Eastwood JD, et al. Comparative overview of brain perfusion imaging techniques. Journal of neuroradiology. Journal de neuroradiologie. 2005.

12. Lui YW, Tang ER, Allmendinger AM, Spektor V. Evaluation of CT perfusion in the setting of cerebral ischemia: Patterns and pitfalls. American Journal of Neuroradiology. 2010.

13. Marchal G, Rioux P, Petit-Tabou MC, Derlon JM, Baron JC, Serrati C, et al. PET imaging of cerebral perfusion and oxygen consumption in acute ischaemic stroke: relation to outcome. Lancet. 1993;

14. Lima A, Bakker J. Noninvasive monitoring of peripheral perfusion. In: Applied Physiology in Intensive Care Medicine 2: Physiological Reviews and Editorials. 2012.

15. Strangman GE, Li Z, Zhang Q. Depth Sensitivity and Source-Detector Separations for Near Infrared Spectroscopy Based on the Colin27 Brain Template. PLoS One. 2013;

16. Kim MN, Durduran T, Frangos S, Edlow BL, Buckley EM, Moss HE, et al. Noninvasive measurement of cerebral blood flow and blood oxygenation using near-infrared and diffuse correlation spectroscopies in critically brain-injured adults. Neurocrit Care. 2010;

17. Chen JJ, Wieckowska M, Meyer E, Pike GB. Cerebral blood flow measurement using fMRI and PET: A cross-validation study. Int J Biomed Imaging. 2008;

18. Ssali T, Anazodo UC, Thiessen JD, Prato FS, St Lawrence K. A noninvasive method

for quantifying cerebral blood flow by hybrid PET/MRI. J Nucl Med. 2018;

19. Campbell BCV, Christensen S, Levi CR, Desmond PM, Donnan GA, Davis SM, et al. Comparison of computed tomography perfusion and magnetic resonance imaging perfusion-diffusion mismatch in ischemic stroke. Stroke. 2012;

20. Muir ER, Watts LT, Tiwari YV, Bresnen A, Shen Q, Duong TQ. Quantitative cerebral blood flow measurements using MRI. Methods Mol Biol. 2014;

21. Calamante F, Thomas DL, Pell GS, Wiersma J, Turner R. Measuring cerebral blood flow using magnetic resonance imaging techniques. Journal of Cerebral Blood Flow and Metabolism. 1999.

22. Essig M, Shiroishi MS, Nguyen TB, Saake M, Provenzale JM, Enterline D, et al. Perfusion MRI: The five most frequently asked technical questions. American Journal of Roentgenology. 2013.

23. Gaudino S, Martucci M, Botto A, Ruberto E, Leone E, Infante A, et al. Brain DSC MR perfusion in children: A clinical feasibility study using different technical standards of contrast administration. Am J Neuroradiol. 2019;

24. Himes NC, Young G. Background on Imaging Structural Imaging. In: Image-Guided Neurosurgery. 2015.

25. Provenzale JM, Wang GR, Brenner T, Petrella JR, Sorensen AG. Comparison of permeability in high-grade and low-grade brain tumors using dynamic susceptibility contrast MR imaging. Am J Roentgenol. 2002;

26. Maeda M, Itoh S, Kimura H, Iwasaki T, Hayashi N, Yamamoto K, et al. Tumor vascularity in the brain: evaluation with dynamic susceptibility-contrast MR imaging.

Radiology. 2014;

27. Schmainda KM, Prah MA, Rand SD, Liu Y, Logan B, Muzi M, et al. Multisite concordance of DSC-MRI analysis for brain tumors: Results of a National Cancer Institute Quantitative Imaging Network Collaborative Project. Am J Neuroradiol. 2018;

28. Lindgren E, Wirestam R, Markenroth Bloch K, Ahlgren A, van Osch MJP, van Westen D, et al. Absolute quantification of perfusion by dynamic susceptibility contrast MRI using Bookend and VASO steady-state CBV calibration: a comparison with pseudo-continuous ASL. Magn Reson Mater Physics, Biol Med. 2014;

29. Tan H, Maldjian JA, Pollock JM, Burdette JH, Yang LY, Deibler AR, et al. A Fast, Effective Filtering Method for Improving Clinical Pulsed Arterial Spin Labeling MRI. J Magn Reson Imaging. 2009;

30. Welker K, Boxerman J, Kalnin A, Kaufmann T, Shiroishi M, Wintermark M. ASFNR recommendations for clinical performance of MR dynamic susceptibility contrast perfusion imaging of the brain. Am J Neuroradiol. 2015;

31. Schmainda KM, Prah MA, Hu LS, Quarles CC, Semmineh N, Rand SD, et al. Moving toward a consensus DSC-MRI protocol: Validation of a low-flip angle single-dose option as a reference standard for brain tumors. Am J Neuroradiol. 2019;

32. Rogosnitzky M, Branch S. Gadolinium-based contrast agent toxicity: a review of known and proposed mechanisms. BioMetals. 2016.

33. Petcharunpaisan S. Arterial spin labeling in neuroimaging. World J Radiol. 2010;

34. Jahng GH, Weiner MW, Schuff N. Improved arterial spin labeling method: Applications for measurements of cerebral blood flow in human brain at high magnetic

field MRI. Med Phys. 2007;

35. Fournet G, Li JR, Cerjanic AM, Sutton BP, Ciobanu L, Le Bihan D. A two-pool model to describe the IVIM cerebral perfusion. J Cereb Blood Flow Metab. 2017;

36. Le Bihan D, Breton E, Lallemand D, Aubin ML, Vignaud J, Laval-Jeantet M. Separation of diffusion and perfusion in intravoxel incoherent motion MR imaging. Radiology. 2014;

37. Le Bihan D. What can we see with IVIM MRI? NeuroImage. 2018;

38. Federau C, Meuli R, O’Brien K, Maeder P, Hagmann P. Perfusion measurement in brain gliomas with intravoxel incoherent motion MRI. Am J Neuroradiol. 2014;

39. Federau C, Cerny M, Roux M, Mosimann PJ, Maeder P, Meuli R, et al. IVIM perfusion fraction is prognostic for survival in brain glioma. Clin Neuroradiol. 2017;

40. Shim WH, Kim HS, Choi CG, Kim SJ. Comparison of apparent diffusion coefficient and intravoxel incoherent motion for differentiating among glioblastoma, metastasis, and lymphoma focusing on diffusion-related parameter. PLoS One. 2015;

41. Hu YC, Yan LF, Wu L, Du P, Chen BY, Wang L, et al. Intravoxel incoherent motion diffusion-weighted MR imaging of gliomas: Efficacy in preoperative grading. Sci Rep. 2014;

42. Federau C. Intravoxel incoherent motion MRI as a means to measure in vivo perfusion: A review of the evidence. NMR in Biomedicine. 2017.

43. Jalnefjord O, Montelius M, Starck G, Ljungberg M. Optimization of b-value schemes for estimation of the diffusion coefficient and the perfusion fraction with segmented intravoxel incoherent motion model fitting. Magn Reson Med. 2019;

44. Jalnefjord O, Andersson M, Montelius M, Starck G, Elf AK, Johanson V, et al. Comparison of methods for estimation of the intravoxel incoherent motion (IVIM) diffusion coefficient (D) and perfusion fraction (f). Magn Reson Mater Physics, Biol Med. 2018;

45. Lemke A, Stieltjes B, Schad LR, Laun FB. Toward an optimal distribution of b values for intravoxel incoherent motion imaging. Magn Reson Imaging. 2011;

46. Pierpaoli C. Quantitative brain MRI. Topics in Magnetic Resonance Imaging. 2010;

47. Winfield JM, Payne GS, Weller A, DeSouza NM. DCE-MRI, DW-MRI, and MRS in cancer: Challenges and advantages of implementing qualitative and quantitative multi-parametric imaging in the clinic. Topics in Magnetic Resonance Imaging. 2016.

48. deSouza NM, Winfield JM, Waterton JC, Weller A, Papoutsaki M V., Doran SJ, et al. Implementing diffusion-weighted MRI for body imaging in prospective multicentre trials: current considerations and future perspectives. Eur Radiol. 2018;

49. Le Bihan D, Iima M, Federau C, Sigmund EE, Barbier EL, Grand S, et al. Other MRI Approaches to Perfusion Imaging (ASL, DSC, DCE). In: Intravoxel Incoherent Motion (IVIM) MRI. 2019.

50. O’Connor JPB, Aboagye EO, Adams JE, Aerts HJWL, Barrington SF, Beer AJ, et al. Imaging biomarker roadmap for cancer studies. Nat Rev Clin Oncol. 2017;

51. Abramson RG, Burton KR, Yu JPJ, Scalzetti EM, Yankeelov TE, Rosenkrantz AB, et al. Methods and Challenges in Quantitative Imaging Biomarker Development. Academic Radiology. 2015.

52. Raunig DL, McShane LM, Pennello G, Gatsonis C, Carson PL, Voyvodic JT, et al.

Quantitative imaging biomarkers: A review of statistical methods for technical performance assessment. Statistical Methods in Medical Research. 2015.

53. Smith ETS. Clinical applications of imaging biomarkers. Part 1. the neuroradiologist's perspective. British Journal of Radiology. 2011.

54. Shukla-Dave A, Obuchowski NA, Chenevert TL, Jambawalikar S, Schwartz LH, Malyarenko D, et al. Quantitative imaging biomarkers alliance (QIBA) recommendations for improved precision of DWI and DCE-MRI derived biomarkers in multicenter oncology trials. Journal of Magnetic Resonance Imaging. 2019.

55. Sullivan DC, Obuchowski NA, Kessler LG, Raunig DL, Gatsonis C, Huang EP, et al. Metrology Standards for Quantitative Imaging Biomarkers. Radiology. 2015;

56. Moreau B, Iannessi A, Hoog C, Beaumont H. How reliable are ADC measurements? A phantom and clinical study of cervical lymph nodes. Eur Radiol. 2018;

57. Bossuyt PM, Reitsma JB, Bruns DE, Gatsonis CA, Glasziou PP, Irwig L, et al. STARD 2015: An updated list of essential items for reporting diagnostic accuracy studies. Clinical Chemistry. 2015.

58. Keenan KE, Biller JR, Delfino JG, Boss MA, Does MD, Evelhoch JL, et al. Recommendations towards standards for quantitative MRI (qMRI) and outstanding needs. J Magn Reson Imaging. 2019;

59. Mahesh M. The Essential Physics of Medical Imaging, Third Edition. Med Phys. 2013;

60. Stroman PW. Source of the MR Signal and Its Properties. In: Essentials of Functional MRI. 2011. p. 37–67.

61. Kale SC, Chen XJ, Henkelman RM. Trading off SNR and resolution in MR images.

NMR Biomed. 2009;

62. Maxwell JC. A Treatise on Electricity and Magnetism Part IV. In: A treatise on electricity and magnetism. 1873.

63. Willinek WA, Schild HH. Clinical advantages of 3.0 T MRI over 1.5 T. Eur J Radiol. 2008;

64. Wood R, Bassett K, Foerster, Spry C, Tong L. 1.5 tesla magnetic resonance imaging scanners compared with 3.0 tesla magnetic resonance imaging scanners: systematic review of clinical effectiveness. CADTH Technol Overv. 2012;

65. Ladd ME, Bachert P, Meyerspeer M, Moser E, Nagel AM, Norris DG, et al. Pros and cons of ultra-high-field MRI/MRS for human application. Progress in Nuclear Magnetic Resonance Spectroscopy. 2018.

66. Reiss-Zimmermann M, Gutberlet M, Köstler H, Fritzsch D, Hoffmann KT. Improvement of SNR and acquisition acceleration using a 32-channel head coil compared to a 12-channel head coil at 3T. Acta radiol. 2013;

67. Gruber B, Froeling M, Leiner T, Klomp DWJ. RF coils: A practical guide for nonphysicists. Journal of Magnetic Resonance Imaging. 2018.

68. Pruessmann KP, Weiger M, Scheidegger MB, Boesiger P. SENSE: Sensitivity encoding for fast MRI. Magn Reson Med. 1999;

69. Dietrich O, Reiser MF, Schoenberg SO. Artifacts in 3-T MRI: Physical background and reduction strategies. Eur J Radiol. 2008;

70. Kneeland JB, Shimakawa A, Wehrli FW. Effect of intersection spacing on MR image contrast and study time. Radiology. 2014;

71. Dietrich O, Raya JG, Reiser MF. Magnetic resonance noise measurements and signal-quantization effects at very low noise levels. Magn Reson Med. 2008;

72. Pal C, Das P, Chakrabarti A, Ghosh R. Rician noise removal in magnitude MRI images using efficient anisotropic diffusion filtering. Int J Imaging Syst Technol. 2017;

73. Gudbjartsson H, Patz S. The rician distribution of noisy mri data. Magn Reson Med. 1995;

74. Coupé P, Manjón J V., Gedamu E, Arnold D, Robles M, Collins DL. Robust Rician noise estimation for MR images. Med Image Anal. 2010;

75. Aja-Fernández S, Vegas-Sánchez-Ferrero G, Tristán-Vega A. Noise estimation in parallel MRI: GRAPPA and SENSE. Magn Reson Imaging. 2014;

76. Robson PM, Grant AK, Madhuranthakam AJ, Lattanzi R, Sodickson DK, McKenzie CA. Comprehensive quantification of signal-to-noise ratio and g-factor for image-based and k-space-based parallel imaging reconstructions. Magn Reson Med. 2008;

77. NEMA. Determination of Signal-to-Noise Ratio (SNR) in Diagnostic Magnetic Resonance Imaging. Natl Electr Manuf Assoc [Internet]. 2001; Available from: https://www.nema.org/Standards/Pages/Determination-of-Signal-to-Noise-Ratio-in-Diagnostic-Magnetic-Resonance-Imaging.aspx

78. Brown R. A brief account of microscopical observations made on the particles contained in the pollen of plants. Philos Mag Ser 2. 1828;

79. Fick A. V. On liquid diffusion . London, Edinburgh, Dublin Philos Mag J Sci. 2018;

80. Le Bihan D, Iima M. Diffusion magnetic resonance imaging: What water tells us about biological tissues. PLoS Biol. 2015;

81. Bammer R. Basic principles of diffusion-weighted imaging. Eur J Radiol. 2003;

82. Kono K, Inoue Y, Nakayama K, Shakudo M, Morino M, Ohata K, et al. The role of diffusion-weighted imaging in patients with brain tumors. Am J Neuroradiol. 2001;

83. Hahn EL. Spin echoes. Phys Rev. 1950;

84. Tanner JE. Pulsed field gradients for NMR spin-echo diffusion measurements. Rev Sci Instrum. 1965;

85. Stejskal EO, Tanner JE. Spin diffusion measurements: Spin echoes in the presence of a time-dependent field gradient. J Chem Phys. 1965;

86. Pipe J. Pulse Sequences for Diffusion-Weighted MRI. In: Diffusion MRI: From Quantitative Measurement to In vivo Neuroanatomy: Second Edition. 2013.

87. Burdette JH, Elster AD, Ricci PE. Acute Cerebral Infarction: Quantification of Spin-Density and T2 Shine-through Phenomena on Diffusion-weighted MR Images. Radiology. 2013;

88. Yablonskiy DA, Sukstanskii AL. Theoretical models of the diffusion weighted MR signal. NMR in Biomedicine. 2010.

89. Kingsley PB, Monahan WG. Selection of the Optimum b Factor for Diffusion-Weighted Magnetic Resonance Imaging Assessment of Ischemic Stroke. Magn Reson Med. 2004;

90. Le Bihan D, Breton E, Lallemand D, Grenier P, Cabanis E, Laval-Jeantet M. MR imaging of intravoxel incoherent motions: application to diffusion and perfusion in neurologic disorders. Radiology. 1986;

91. Le Bihan D, Breton E. Imagerie de diffusion in-vivo par résonance magnetique nucléaire. Comptes-Rendus l’Académie des Sci. 1985;

92. Niendorf T, Dijkhuizen RM, Norris DG, Van Lookeren Campagne M, Nicolay K. Biexponential diffusion attenuation in various states of brain tissue: Implications for diffusion-weighted imaging. Magn Reson Med. 1996;

93. KÄRGER J, Pfeifer H, Heink W. Principles and Application of Self-Diffusion Measurements by Nuclear Magnetic Resonance. In: Advances in Magnetic and Optical Resonance. 1988.

94. Tu Van A, Granziera C, Bammer R. An Introduction to Model-Independent Diffusion MRI. Top Magn Reson imaging TMRI. 2010;

95. Ghosh A, Singh T, Singla V, Bagga R, Khandelwal N. Comparison of absolute Apparent Diffusion Coefficient (ADC) values in ADC maps generated across different postprocessing software: Reproducibility in endometrial carcinoma. Am J Roentgenol. 2017;

96. Herneth AM, Guccione S, Bednarski M. Apparent diffusion coefficient: a quantitative parameter for in vivo tumor characterization. Eur J Radiol. 2003;

97. Yamasaki F, Kurisu K, Satoh K, Arita K, Sugiyama K, Ohtaki M, et al. Apparent Diffusion Coefficient of Human Brain Tumors at MR Imaging. Radiology. 2005;

98. Koh DM, Collins DJ. Diffusion-weighted MRI in the body: Applications and challenges in oncology. Am J Roentgenol. 2007;

99. El Kady RM, Choudhary AK, Tappouni R. Accuracy of apparent diffusion coefficient value measurement on PACS workstation: A comparative analysis. Am J Roentgenol.

2011;

100. Hilario A, Ramos A, Perez-Nuñez A, Salvador E, Millan JM, Lagares A, et al. The added value of apparent diffusion coefficient to cerebral blood volume in the preoperative grading of diffuse gliomas. Am J Neuroradiol. 2012;

101. Helenius J, Soinne L, Perkiö J, Salonen O, Kangasmäki A, Kaste M, et al. Diffusion-weighted MR imaging in normal human brains in various age groups. Am J Neuroradiol. 2002;

102. Koh DM, Collins DJ, Orton MR. Intravoxel incoherent motion in body diffusion-weighted MRI: Reality and challenges. American Journal of Roentgenology. 2011.

103. Federau C, Sumer S, Becce F, Maeder P, O'Brien K, Meuli R, et al. Intravoxel incoherent motion perfusion imaging in acute stroke: Initial clinical experience. Neuroradiology. 2014;

104. Iima M, Le Bihan D. Clinical Intravoxel Incoherent Motion and Diffusion MR Imaging: Past, Present, and Future. Radiology. 2015;

105. Du J, Li K, Zhang W, Wang S, Song Q, Liu A, et al. Intravoxel incoherent motion MR imaging: Comparison of diffusion and perfusion characteristics for differential diagnosis of soft tissue tumors. Med (United States). 2015;

106. Ma W, Zhang G, Ren J, Pan Q, Wen D, Zhong J, et al. Quantitative parameters of intravoxel incoherent motion diffusion weighted imaging (IVIM-DWI): potential application in predicting pathological grades of pancreatic ductal adenocarcinoma. Quant Imaging Med Surg. 2018;

107. Ichikawa S, Motosugi U, Ichikawa T, Sano K, Morisaka H, Araki T. Intravoxel

incoherent motion imaging of the kidney: Alterations in diffusion and perfusion in patients with renal dysfunction. Magn Reson Imaging. 2013;

108. Mürtz P, Sprinkart AM, Reick M, Pieper CC, Schievelkamp AH, König R, et al. Accurate IVIM model-based liver lesion characterisation can be achieved with only three b-value DWI. Eur Radiol. 2018;

109. Luciani A, Vignaud A, Cavet M, Tran Van Nhieu J, Mallat A, Ruel L, et al. Liver Cirrhosis: Intravoxel Incoherent Motion MR Imaging—Pilot Study. Radiology. 2008;

110. Deng Y, Yang B, Peng Y, Liu Z, Luo J, Du G. Use of intravoxel incoherent motion diffusion-weighted imaging to detect early changes in diabetic kidneys. Abdom Radiol. 2018;

111. Wu WC, Chen YF, Tseng HM, Yang SC, My PC. Caveat of measuring perfusion indexes using intravoxel incoherent motion magnetic resonance imaging in the human brain. Eur Radiol. 2015;

112. Federau C, Maeder P, O'Brien K, Browaeys P, Meuli R, Hagmann P. Quantitative Measurement of Brain Perfusion with Intravoxel Incoherent Motion MR Imaging. Radiology. 2012;

113. Yamada I, Aung W, Himeno Y, Nakagawa T, Shibuya H. Diffusion coefficients in abdominal organs and hepatic lesions: Evaluation with intravoxel incoherent motion echo-planar MR imaging. Radiology. 1999;

114. Patel J, Sigmund EE, Rusinek H, Oei M, Babb JS, Taouli B. Diagnosis of cirrhosis with intravoxel incoherent motion diffusion MRI and dynamic contrast-enhanced MRI alone and in combination: Preliminary experience. J Magn Reson Imaging. 2010;

115. Leporq B, Saint-Jalmes H, Rabrait C, Pilleul F, Guillaud O, Dumortier J, et al. Optimization of intra-voxel incoherent motion imaging at 3.0 Tesla for fast liver examination. J Magn Reson Imaging. 2015;

116. Cohen AD, Schieke MC, Hohenwalter MD, Schmainda KM. The effect of low b-values on the intravoxel incoherent motion derived pseudodiffusion parameter in liver. Magn Reson Med. 2015;

117. Zhang JL, Sigmund EE, Rusinek H, Chandarana H, Storey P, Chen Q, et al. Optimization of b-value sampling for diffusion-weighted imaging of the kidney. Magn Reson Med. 2012;

118. Jambor I, Merisaari H, Aronen HJ, Järvinen J, Saunavaara J, Kauko T, et al. Optimization of b-value distribution for biexponential diffusion-weighted MR imaging of normal prostate. J Magn Reson Imaging. 2014;

119. Cho GY, Moy L, Zhang JL, Baete S, Lattanzi R, Moccaldi M, et al. Comparison of fitting methods and b-value sampling strategies for intravoxel incoherent motion in breast cancer. Magn Reson Med. 2015;

120. Federau C, O’Brien K, Meuli R, Hagmann P, Maeder P. Measuring brain perfusion with intravoxel incoherent motion (IVIM): Initial clinical experience. J Magn Reson Imaging. 2014;

121. Meeus EM, Novak J, Withey SB, Zarinabad N, Dehghani H, Peet AC. Evaluation of intravoxel incoherent motion fitting methods in low-perfused tissue. J Magn Reson Imaging. 2017;

122. Zhang SX, Jia QJ, Zhang ZP, Liang CH, Chen WB, Qiu QH, et al. Intravoxel

incoherent motion MRI: Emerging applications for nasopharyngeal carcinoma at the primary site. Eur Radiol. 2014;

123. Yao Y, Zhang S, Tang X, Zhang S, Shi J, Zhu W, et al. Intravoxel incoherent motion diffusion-weighted imaging in stroke patients: initial clinical experience. Clin Radiol. 2016;

124. Bisdas S, Klose U. IVIM analysis of brain tumors: an investigation of the relaxation effects of CSF, blood, and tumor tissue on the estimated perfusion fraction. Magn Reson Mater Physics, Biol Med. 2015;

125. Barbieri S, Donati OF, Froehlich JM, Thoeny HC. Impact of the calculation algorithm on biexponential fitting of diffusion-weighted MRI in upper abdominal organs. Magn Reson Med. 2016;

126. Chen W, Zhang J, Long D, Wang Z, Zhu JM. Optimization of intra-voxel incoherent motion measurement in diffusion-weighted imaging of breast cancer. J Appl Clin Med Phys. 2017;

127. Ertas G. Fitting Intravoxel Incoherent Motion Model to Diffusion MR Signals of the Human Breast Tissue using Particle Swarm Optimization. An Int J Optim Control Theor Appl. 2019;

128. Zhang Z, Hallac RR, Peschke P, Mason RP. A noninvasive tumor oxygenation imaging strategy using magnetic resonance imaging of endogenous blood and tissue water. Magn Reson Med. 2014;

129. Jahng GH, Li KL, Ostergaard L, Calamante F. Perfusion magnetic resonance imaging: A comprehensive update on principles and techniques. Korean Journal of Radiology.

2014.

130. Shiroishi MS, Castellazzi G, Boxerman JL, D’Amore F, Essig M, Nguyen TB, et al. Principles of T2∗-weighted dynamic susceptibility contrast MRI technique in brain tumor imaging. Journal of Magnetic Resonance Imaging. 2015.

131. Calamante F. Arterial input function in perfusion MRI: A comprehensive review. Progress in Nuclear Magnetic Resonance Spectroscopy. 2013.

132. Mouridsen K, Christensen S, Gyldensted L, Østergaard L. Automatic selection of arterial input function using cluster analysis. Magn Reson Med. 2006;

133. Hu LS, Baxter LC, Pinnaduwage DS, Paine TL, Karis JP, Feuerstein BG, et al. Optimized preload leakage-correction methods to improve the diagnostic accuracy of dynamic susceptibility-weighted contrast-enhanced perfusion MR imaging in posttreatment gliomas. Am J Neuroradiol. 2010;

134. Quarles CC, Gochberg DF, Gore JC, Yankeelov TE. A theoretical framework to model DSC-MRI data acquired in the presence of contrast agent extravasation. Phys Med Biol. 2009;

135. Kanal E, Maravilla K, Rowley HA. Gadolinium contrast agents for CNS imaging: Current concepts and clinical evidence. American Journal of Neuroradiology. 2014.

136. Kanda T, Ishii K, Kawaguchi H, Kitajima K, Takenaka D. High Signal Intensity in the Dentate Nucleus and Globus Pallidus on Unenhanced T1-weighted MR Images: Relationship with Increasing Cumulative Dose of a Gadolinium-based Contrast Material. Radiology. 2014;

137. Ferré JC, Bannier E, Raoult H, Mineur G, Carsin-Nicol B, Gauvrit JY. Arterial spin

labeling (ASL) perfusion: Techniques and clinical use. Diagnostic and Interventional Imaging. 2013.

138. Kim HS, Suh CH, Kim N, Choi CG, Kim SJ. Histogram analysis of intravoxel incoherent motion for differentiating recurrent tumor from treatment effect in patients with glioblastoma: Initial clinical experience. Am J Neuroradiol. 2014;

139. Bane O, Wagner M, Zhang JL, Dyvorne HA, Orton M, Rusinek H, et al. Assessment of renal function using intravoxel incoherent motion diffusion-weighted imaging and dynamic contrast-enhanced MRI. J Magn Reson Imaging. 2016;

140. Bisdas S, Braun C, Skardelly M, Schittenhelm J, Teo TH, Thng CH, et al. Correlative assessment of tumor microcirculation using contrast-enhanced perfusion MRI and intravoxel incoherent motion diffusion-weighted MRI: Is there a link between them? NMR Biomed. 2014;

141. Xu XQ, Choi YJ, Sung YS, Yoon RG, Jang SW, Park JE, et al. Intravoxel incoherent motion MR imaging in the head and neck: Correlation with dynamic contrast-enhanced MR imaging and diffusion-weighted imaging. Korean J Radiol. 2016;

142. Maier SE, Mulkern R V. Biexponential analysis of diffusion-related signal decay in normal human cortical and deep gray matter. Magn Reson Imaging. 2008;

143. Lätt J, Nilsson M, Wirestam R, Johansson E, Larsson EM, Stahlberg F, et al. In vivo visualization of displacement-distribution-derived parameters in q-space imaging. Magn Reson Imaging. 2008;

144. Hayashi T, Miyati T, Takahashi J, Fukuzawa K, Sakai H, Tano M, et al. Diffusion analysis with triexponential function in liver cirrhosis. J Magn Reson Imaging. 2013;

145. Ueda Y, Takahashi S, Ohno N, Kyotani K, Kawamitu H, Miyati T, et al. Triexponential function analysis of diffusion-weighted MRI for diagnosing prostate cancer. J Magn Reson Imaging. 2016;

146. Zeng Q, Shi F, Zhang J, Ling C, Dong F, Jiang B. A Modified Tri-Exponential Model for Multi-b-value Diffusion-Weighted Imaging: A Method to Detect the Strictly Diffusion-Limited Compartment in Brain. Front Neurosci. 2018;

147. Ohno N, Miyati T, Kobayashi S, Gabata T. Modified triexponential analysis of intravoxel incoherent motion for brain perfusion and diffusion. J Magn Reson Imaging. 2016;

148. Hu Y-C, Yan L-F, Sun Q, Liu Z-C, Wang S-M, Han Y, et al. Comparison between ultra-high and conventional mono b-value DWI for preoperative glioma grading. Oncotarget. 2017;

149. Ohno N, Miyati T, Kobayashi S, Gabata T. Reply to: On the perils of multiexponential fitting of diffusion MR data. J Magn Reson Imaging. 2017;

150. Jensen JH, Helpern JA. MRI quantification of non-Gaussian water diffusion by kurtosis analysis. NMR in Biomedicine. 2010.

151. Grant SC, Buckley DL, Gibbs S, Webb AG, Blackband SJ. MR microscopy of multicomponent diffusion in single neurons. Magn Reson Med. 2001;

152. Schwarcz A, Bogner P, Meric P, Correze JL, Berente Z, Pál J, et al. The Existence of Biexponential Signal Decay in Magnetic Resonance Diffusion-Weighted Imaging Appears to Be Independent of Compartmentalization. Magn Reson Med. 2004;

153. Van Baalen S, Froeling M, Asselman M, Klazen C, Jeltes C, Van Dijk L, et al. Mono,

bi- and tri-exponential diffusion MRI modelling for renal solid masses and comparison with histopathological findings. Cancer Imaging. 2018;

154. van der Bel R, Gurney-Champion OJ, Froeling M, Nederveen AJ, Krediet CTp. Tri-exponential approach for intravoxel incoherent motion analysis of multi b-value diffusion weighted MRI data follows GFR changes in healthy humans. Nephrol Dial Transplant. 2017;

155. Chevallier O, Zhou N, Cercueil J-P, He J, Loffroy R, Wang Y-X. Comparison of tri-exponential decay vs. bi-exponential decay and full fitting vs. segmented fitting for modeling liver intravoxel incoherent motion diffusion MRI. bioRxiv. 2018;

156. Cercueil JP, Petit JM, Nougaret S, Soyer P, Fohlen A, Pierredon-Foulongne MA, et al. Intravoxel incoherent motion diffusion-weighted imaging in the liver: comparison of mono-, bi- and tri-exponential modelling at 3.0-T. Eur Radiol. 2015;

157. Yablonskiy DA, Bretthorst GL, Ackerman JJH. Statistical model for diffusion attenuated MR signal. Magn Reson Med. 2003;

158. Jensen JH, Helpern JA, Ramani A, Lu H, Kaczynski K. Diffusional kurtosis imaging: The quantification of non-Gaussian water diffusion by means of magnetic resonance imaging. Magn Reson Med. 2005;

159. Pavilla A, Gambarota G, Arrigo A, Mejdoubi M, Duvauferrier R, Saint-Jalmes H. Diffusional kurtosis imaging (DKI) incorporation into an intravoxel incoherent motion (IVIM) MR model to measure cerebral hypoperfusion induced by hyperventilation challenge in healthy subjects. Magn Reson Mater Physics, Biol Med. 2017;

160. Bertleff M, Domsch S, Weingärtner S, Zapp J, O'Brien K, Barth M, et al. Diffusion

parameter mapping with the combined intravoxel incoherent motion and kurtosis model using artificial neural networks at 3 T. NMR Biomed. 2017;

161. Glenn GR, Tabesh A, Jensen JH. A simple noise correction scheme for diffusional kurtosis imaging. Magn Reson Imaging. 2015;
162. Gardner DG, Gardner JC, Laush G, Wayne Meinke W. Method for the analysis of multicomponent exponential decay curves. J Chem Phys. 1959;
163. Landaw EM, DiStefano JJ. Multiexponential, multicompartmental, and noncompartmental modeling. II. Data analysis and statistical considerations. Am J Physiol Integr Comp Physiol. 2017;
164. Holmström K, Petersson J. A review of the parameter estimation problem of fitting positive exponential sums to empirical data. Appl Math Comput. 2002;
165. Wiscombe WJ, Evans JW. Exponential-sum fitting of radiative transmission functions. J Comput Phys. 1977;
166. Ponce Hornos J, Villamil MF. A simple method for fitting multi-exponential curves of the decay type in a hand calculator. Acta Physiol Lat Am. 1980;
167. Hunt GE, Grant IP. Discrete Space Theory of Radiative Transfer and its Application to Problems in Planetary Atmospheres. J Atmos Sci. 2002;
168. Demeure CJ, Scharf LL. Initial results in prony analysis of power system response signals. IEEE Trans Power Syst. 1990;
169. Potts D, Tasche M. Parameter estimation for exponential sums by approximate Prony method. Signal Processing. 2010;

170. Osborne MR, Smyth GK. A Modified Prony Algorithm for Exponential Function Fitting. SIAM J Sci Comput. 2005;

171. Kumaresan R, Tufts DW, Scharf LL. A Prony Method for Noisy Data: Choosing the Signal Components and Selecting the Order in Exponential Signal Models. Proc IEEE. 1984;

172. Jibia AU, Salami M-JE. An Appraisal of Gardner Transform-Based Methods of Transient Multiexponential Signal Analysis. Int J Comput Theory Eng. 2013;

173. Akaike H. A New Look at the Statistical Model Identification. IEEE Trans Automat Contr. 1974;

174. Whittle P. Hypothesis testing in time series analysis. Uppsala: Almqvist & Wiksells boktr.; 1951.

175. Neyran B, Carme S, Wiart M, Robini M, Soulas EPC. Mapping myocardial perfusion with an intravascular MR contrast agent, A robust estimation by a spatially constrained approach. In: Computers in Cardiology. 2005.

176. Liu H, Shi J. Applying ARMA-GARCH approaches to forecasting short-term electricity prices. Energy Econ. 2013;

177. Gustavsson P, Nordströrm J. The impact of seasonal unit roots and vector ARMA modelling on forecasting monthly tourism flows. Tour Econ. 2001;

178. Bechtel MM, Leuffen D. Forecasting european union politics: Real-time forecasts in political time series analysis. Eur Union Polit. 2010;

179. Pukkila T, Koreisha S, Kallinen A. The identification of ARMA models. Biometrika. 1990;

180. Predictive Modeling Applications in Actuarial Science. Predictive Modeling Applications in Actuarial Science. 2016.

181. Box GEP, Jenkins GM, Reinsel GC, Ljung GM. Time Series Analysis: Forecasting and Control, 5th Edition, by. Journal of Time Series Analysis. 2015.

182. Simpson SL, Edwards LJ, Muller KE, Sen PK, Styner MA. A linear exponent AR(1) family of correlation structures. Stat Med. 2010;

183. Seymour L, Brockwell PJ, Davis RA. Introduction to Time Series and Forecasting. J Am Stat Assoc. 2006;

184. Smith MR, Nichols ST, Henkelman RM, Wood ML. Application of Autoregressive Moving Average Parametric Modeling in Magnetic Resonance Image Reconstruction. IEEE Trans Med Imaging. 1986;

185. Wood JC, Enriquez C, Ghugre N, Tyzka JM, Carson S, Nelson MD, et al. MRI R2 and R2* mapping accurately estimates hepatic iron concentration in transfusion-dependent thalassemia and sickle cell disease patients. Blood. 2005;

186. Taylor BA, Hwang KP, Elliott AM, Shetty A, Hazle JD, Stafford RJ. Dynamic chemical shift imaging for image-guided thermal therapy: Analysis of feasibility and potential. Med Phys. 2008;

187. Batchelor P, Chiribiri A, Nooralipour NZ, Cvetković Z. ARMA regularization of cardiac perfusion modeling. In: ICASSP, IEEE International Conference on Acoustics, Speech and Signal Processing - Proceedings. 2010.

188. Khalighi MM, Soltanian-Zadeh H, Ewing JR. ARMA modeling for estimation of permeability from perfusion MRI. In: Proceedings - International Symposium on

Biomedical Imaging. 2002.

189. Neyran B, Janier MF, Casali C, Revel D, Canet Soulas EP. Mapping myocardial perfusion with an intravascular MR contrast agent: Robustness of deconvolution methods at various blood flows. Magn Reson Med. 2002;

190. Chilla GS. Diffusion weighted magnetic resonance imaging and its recent trend—a survey. Klin Monatsbl Augenheilkd. 2015;

191. Meeus EM, Novak J, Dehghani H, Peet AC. Rapid measurement of intravoxel incoherent motion (IVIM) derived perfusion fraction for clinical magnetic resonance imaging. Magn Reson Mater Physics, Biol Med. 2018;

192. Kim M, Kim HS. Emerging techniques in brain tumor imaging: What radiologists need to know. Korean Journal of Radiology. 2016.

193. Cavanaugh JE. Unifying the derivations for the Akaike and corrected Akaike information criteria. Stat Probab Lett. 2003;

194. Panagiotaki E, Schneider T, Siow B, Hall MG, Lythgoe MF, Alexander DC. Compartment models of the diffusion MR signal in brain white matter: A taxonomy and comparison. Neuroimage. 2012;

195. Schwarz G. Estimating the Dimension of a Model. Ann Stat. 1978;

196. McQuarrie AD. A small-sample correction for the Schwarz SIC model selection criterion. Stat Probab Lett. 1999;

197. Akaike H. Prediction and Entropy. In: A Celebration of Statistics. 2011.

198. Kass RE, Raftery AE. Bayes factors. J Am Stat Assoc. 1995;

199. Taouli B, Beer AJ, Chenevert T, Collins D, Lehman C, Matos C, et al. Diffusion-weighted imaging outside the brain: Consensus statement from an ISMRM-sponsored workshop. Journal of Magnetic Resonance Imaging. 2016.

200. Salminen LE, Conturo TE, Bolzenius JD, Cabeen RP, Akbudak E, Paul RH. Reducing CSF Partial Volume Effects to Enhance Diffusion Tensor Imaging Metrics of Brain Microstructure. Technol Innov. 2016;

201. Chavez CE, Alonzo-Atienza F, Alvarez D. Avoiding the inverse crime in the Inverse Problem of electrocardiography: Estimating the shape and location of cardiac ischemia. In: 2013 40th Computing in Cardiology Conference, CinC 2013. 2013.

202. Calamante F. Perfusion MRI using dynamic-susceptibility contrast MRI: Quantification issues in patient studies. Top Magn Reson Imaging. 2010;

203. Delgado AF, Delgado AF. Discrimination between glioma grades II and III using dynamic susceptibility perfusion MRI: A meta-analysis. Am J Neuroradiol. 2017;

204. Spampinato MV, Schiarelli C, Cianfoni A, Giglio P, Welsh CT, Bisdas S, et al. Correlation between cerebral blood volume measurements by perfusion-weighted magnetic resonance imaging and two-year progression-free survival in gliomas. Neuroradiol J. 2013;

205. Singh R, Kesavabhotla K, Kishore SA, Zhou Z, Tsiouris AJ, Filippi CG, et al. Dynamic susceptibility contrast-enhanced mr perfusion imaging in assessing recurrent glioblastoma response to superselective intra-arterial bevacizumab therapy. Am J Neuroradiol. 2016;

206. Gale EM, Caravan P, Rao AG, McDonald RJ, Winfeld M, Fleck RJ, et al. Gadolinium-

based contrast agents in pediatric magnetic resonance imaging. Pediatric Radiology. 2017.

207. Duyn JH, Van Gelderen P, Talagala L, Koretsky A, De Zwart JA. Technological advances in MRI measurement of brain perfusion. In: Journal of Magnetic Resonance Imaging. 2005.

208. Bihan D Le, Turner R. The capillary network: a link between ivim and classical perfusion. Magn Reson Med. 1992;

209. Conklin J, Heyn C, Roux M, Cerny M, Wintermark M, Federau C. A simplified model for intravoxel incoherent motion perfusion imaging of the brain. In: American Journal of Neuroradiology. 2016.

210. Puig J, Sánchez-González J, Blasco G, Daunis-I-Estadella P, Federau C, Alberich-Bayarri Á, et al. Intravoxel incoherent motion metrics as potential biomarkers for survival in glioblastoma. PLoS One. 2016;

211. Suh CH, Kim HS, Lee SS, Kim N, Yoon HM, Choi C-G, et al. Atypical Imaging Features of Primary Central Nervous System Lymphoma That Mimics Glioblastoma: Utility of Intravoxel Incoherent Motion MR Imaging. Radiology. 2014;

212. Wirestam R, Borg M, Brockstedt S, Lindgren A, Holtås S, Ståhlberg F. Perfusion-related parameters in intravoxel incoherent motion MR imaging compared with CBV and CBF measured by dynamic susceptibility-contrast MR technique. Acta radiol. 2001;

213. Metcalfe-Smith E, Meeus E, Novak J, Dehghani H, Peet A, Zarinabad N. Auto-regressive Discrete Acquisition Points Transformation for Diffusion Weighted MRI

Data. IEEE Trans Biomed Eng. 2019;

214. Boxerman JL, Schmainda KM, Weisskoff RM. Relative cerebral blood volume maps corrected for contrast agent extravasation significantly correlate with glioma tumor grade, whereas uncorrected maps do not. Am J Neuroradiol. 2006;

215. Novak J, Withey SB, Lateef S, Macpherson L, Pinkey B, Peet AC. a comparison of pseudo-continuous arterial spin labelling and dynamic susceptibility contrast MrI with and without contrast agent leakage correction in paediatric brain tumours. Br J Radiol. 2019;

216. Smith SM. Fast robust automated brain extraction. Hum Brain Mapp. 2002;

217. Zhang Y, Brady M, Smith S. Segmentation of brain MR images through a hidden Markov random field model and the expectation-maximization algorithm. IEEE Trans Med Imaging. 2001;

218. Lai V, Li X, Lee VHF, Lam KO, Fong DYT, Huang B, et al. Nasopharyngeal carcinoma: Comparison of diffusion and perfusion characteristics between different tumour stages using intravoxel incoherent motion MR imaging. Eur Radiol. 2014;

219. Eberhardt C, Wurnig MC, Wirsching A, Rossi C, Rottmar M, Özbay PS, et al. Intravoxel incoherent motion analysis of abdominal organs: computation of reference parameters in a large cohort of C57Bl/6 mice and correlation to microvessel density. Magn Reson Mater Physics, Biol Med. 2016;

220. Park HJ, Sung YS, Lee SS, Lee Y, Cheong H, Kim YJ, et al. Intravoxel incoherent motion diffusion-weighted MRI of the abdomen: The effect of fitting algorithms on the accuracy and reliability of the parameters. J Magn Reson Imaging. 2017;

221. Andreou A, Koh DM, Collins DJ, Blackledge M, Wallace T, Leach MO, et al. Measurement reproducibility of perfusion fraction and pseudodiffusion coefficient derived by intravoxel incoherent motion diffusion-weighted MR imaging in normal liver and metastases. Eur Radiol. 2013;

222. Grech-Sollars M, Hales PW, Miyazaki K, Raschke F, Rodriguez D, Wilson M, et al. Multi-centre reproducibility of diffusion MRI parameters for clinical sequences in the brain. NMR Biomed. 2015;

223. Mannelli L, Nougaret S, Vargas HA, Do RKG. Advances in Diffusion-Weighted Imaging. Radiologic Clinics of North America. 2015.

224. Dyvorne H, Jajamovich G, Kakite S, Kuehn B, Taouli B. Intravoxel incoherent motion diffusion imaging of the liver: Optimal b-value subsampling and impact on parameter precision and reproducibility. Eur J Radiol. 2014;

225. Granata V, Fusco R, Catalano O, Guarino B, Granata F, Tatangelo F, et al. Intravoxel incoherent motion (IVIM) in diffusion-weighted imaging (DWI) for Hepatocellular carcinoma: correlation with histologic grade. Oncotarget. 2016;

226. Lee JH, Cheong H, Lee SS, Lee CK, Sung YS, Huh JW, et al. Perfusion Assessment Using Intravoxel Incoherent Motion-Based Analysis of Diffusion-Weighted Magnetic Resonance Imaging: Validation Through Phantom Experiments. Invest Radiol. 2016;

227. Moran PA, Whittle P. Hypothesis Testing in Time Series Analysis. J R Stat Soc Ser A. 2006;

228. Dietrich O, Raya JG, Reeder SB, Reiser MF, Schoenberg SO. Measurement of signal-to-noise ratios in MR images: Influence of multichannel coils, parallel imaging, and

reconstruction filters. J Magn Reson Imaging. 2007;

229. Pekar J, Moonen CTW, van Zijl PCM. On the precision of diffusion/perfusion imaging by gradient sensitization. Magn Reson Med. 1992;

230. Orton MR, Collins DJ, Koh DM, Leach MO. Improved intravoxel incoherent motion analysis of diffusion weighted imaging by data driven Bayesian modeling. Magn Reson Med. 2014;

231. While PT. A comparative simulation study of bayesian fitting approaches to intravoxel incoherent motion modeling in diffusion-weighted MRI. Magn Reson Med. 2017;

232. Reischauer C, Gutzeit A. Image denoising substantially improves accuracy and precision of intravoxel incoherent motion parameter estimates. PLoS One. 2017;